THE ROLE OF ACTIN CYTOSKELETON IN ENDOCYTOSIS IN THE SALIVARY GLANDS OF LIVE RODENTS

Andrius Masedunskas

A dissertation submitted to the faculty of the University of North Carolina at Chapel Hill in partial fulfillment of the requirements for the degree of Doctor of Philosophy in the Department of Biology in the College of Arts and Sciences.

Chapel Hill
2014

Approved by:

Steve Rogers

Mara Duncan

Kerry S. Bloom

Julie Donaldson

Paul Randazzo

Roberto Weigert

ABSTRACT

Andrius Masedunskas: The Role of Actin Cytoskeleton in Endocytosis
and Exocytosis in the Salivary Glands of Live Rodents
(Under the direction of Roberto Weigert)

In the last two decades, mammalian cell biology has greatly benefited from major technological advances in light microscopy that have enabled imaging virtually any cellular process at different levels of resolution. However, mammalian cell biology has been studied primarily by using *in vitro* models. Cell culture models have been used the most, since it offers several advantages such as, being amenable to both pharmacological and genetic manipulations, reproducibility, and relatively low costs. However, their major limitation is that the architecture and physiology of cells *in vitro* differ considerably from the *in vivo* environment. This issue can be overcome by the use of intravital microscopy, which encompasses various optical microscopy techniques aimed at visualizing biological processes in live animals. Recent developments in non-linear optical microscopy resulted in an enormous increase of *in vivo* studies, which have addressed key biological questions in fields such as neurobiology, immunology and tumor biology. However, the motion artifacts derived from heartbeat and respiration have prevented the imaging of intracellular structures and limited the use of intravital microscopy to the analysis of tissue architecture or single cell behavior.

In this respect, the goals of my thesis have been: 1) the development of an experimental system that enables visualizing subcellular organelles in live rodents for

extended periods of time, and 2) the investigation of the role of the actin cytoskeleton in endocytosis and exocytosis in live rodents. Here, I describe the establishment of a model for studying endocytosis end exocytosis in the salivary glands of live rats and mice. Moreover, I show that both processes can be imaged in live animals and that their behavior and kinetics differ from what has been reported in *in vitro* systems. Next, I show that the salivary glands can be genetically and pharmacologically manipulated *in situ,* thus opening the door for the investigation of the molecular machinery regulating membrane trafficking in live animals. Finally, in the last part of my dissertation, I focus on specific approaches developed to study the kinetics of exocytosis of single secretory granules and discuss how the actin cytoskeleton plays a fundamental role in controlling this process.

ACKNOWLEDGMENTS

Here I would like to thank several people, who have played a major part in the completion of my PhD. Without their support I would not be where I am today and probably would have fallen “trough the cracks”.

First, I would like to thank my Committee: Drs. Mara Duncan, Julie Donaldson, Kerry Bloom, Paul Randazzo, and Steve Rogers. Thank you all for your support, you all have been really great! I felt that I really need the guidance and the support, especially in the beginning when my project was really “out there”. Thank you for requesting more clarity and structure, it really helped to organize my project. In the end I came to realize, there may be something to a hypothesis-driven research ☺. I am also very grateful to you for all the advice I received on the experimental design, presentation of the results, and most importantly, all the career-related advice.

Next, I would like to thank my thesis advisor and mentor, Dr. Roberto Weigert. I was generally lucky in choosing good mentors but you have really stood out. I am forever indebted to you for sharing your insights, knowledge, and skills not only in science but also in life in general. Thank you for being extremely accommodating and supportive. It felt like you took my success as your own responsibility. I also appreciate you being open and transparent, always keeping me in the know and not only pointing out opportunities but also effectively creating them for me. It has been great to work with you and I hope there will be someone else around that can poke fun at you! It definitely makes for a better working environment ☺.

Thanks also to you, former and current members of the Weigert's lab, or IMTU as it is known. It has been a fun ride! First, I would like to acknowledge the starter of the lab, Myo-Pale' Aye, a very nice and all around super-great girl. I guess, by definition, without her there would be no IMTU. I am also grateful to Monika Sramkova for all her help with the experiments that I could not or would not do ☺. Laura Parente, you will always be remembered as a cheerful and lively girl that got stuff done around here: it was definitely a pleasure! I thank Tim Wigand for all his support and silly jokes around the lab. Also to Walt whose last name is too long and complicated to be covered in this thesis. Thanks for very interesting science conversations and for your insights and the skepticisms. And for Thai cooking tips too! The last shout-out goes out to Natalie Porat Shliom. Thanks for being real and blunt, your remarks about our exciting artifacts are always well taken. Thanks for the hangouts and for talking always, regardless of what, where or when.

Additionally, I would like to thank all the people that I was fortunate to interact with at our institute and branch. I would like to mention select few that particularly contributed to my growth as a scientist: Silvio Gutkind for sharing his amazing insights in everything science-related; Thomas Bugge for spreading his rigorous approach to science and all mice-related advice; and Alfredo Molinolo regarding his expertise in histopathology. I would like to add all of my collaborators from the institute and NIH-wide to this list. Many of the collaborations have resulted in publications, but even the ones that did not were part of my learning experience, so thank you all (yes, Dan, that includes you too).

Lastly, I would like to thank my family and friends. Without their constant presence and moral support I would have packed my bags already. So thank you Dad, Mom and Asta

(ok, and your now fiancé Joe). An especially huge thanks goes to Katiuchia Uzzun, who has been my best friend and family here at NIH over the years. A special thanks also goes to “one of a kind” cousin Vyga and another great friend Danielle. Big thanks goes to all my friends for all the fun times and for just being there, including Aline, Higor, Sidney, Nathalia, Ntinos, Lorena, Anna, Adam… too many to mention ☺.

TABLE OF CONTENTS

LIST OF FIGURES

LIST OF ABBREVIATIONS

2D	Two-dimensional
3D	Three-dimensional
488-D	Alexa-488 dextran
APM	Apical plasma membrane
Bleb	Blebbistatin
BSA	Bovine serum albumin
Carb	Carbachol
CDE	Clathrin-dependent endocytosis
CIE	Clathrin-independent endocytosis
Cyt D	Cytochalasin D
EGF	Epidermal growth factor
FVB	Friend virus type-B
GFP	Green fluorescent protein
GPCR	G-protein coupled receptor
IR	Infra-red
Iso	Isoproteranol
IVM	Intravital microscopy
Jasp	Jasplakinolide
LatA	Latrunculin A
MPM	Multiphoton microscopy
NIR	Near-infrared
PM	Plasma membrane

PMT	Photo multiplier tube
SC	Sub-cutaneous injection
SCG	Secretory granule
SG	Salivary gland
SHG	Second harmonic generation
THG	Third harmonic generation
TIRF	Total internal reflection microscopy
TMRM	Tetra-methyl rhodamine methyl ester
TXR-D	Texas-red dextran

INTRODUCTION

This introduction will provide a general and brief overview of endocytosis, regulated exocytosis, and the role of the actin cytoskeleton in these processes. The main goal is to convey the message that some of the conflicting data in the literature may be due to the use of *in vitro* and *ex vivo* experimental models. Next, the advantages and the limitations of these systems will be discussed in more details, emphasizing the need for the use of a combination of *in vivo* models and light microscopy-based approaches. Finally, a more detailed overview of intravital microscopy (IVM), its applications, and the potential for studying subcellular structures will be presented.

1. Endocytosis and regulated exocytosis

1.1 Endocytosis

Endocytosis is a fundamental process in a variety of cellular events, such as nutrient uptake, cell signaling, establishment and maintenance of cell polarity and remodeling of the plasma membrane (PM); it is also exploited by various pathogens as portal of entry into the target cells [1]. During the past decade, live-cell fluorescence microscopy, genetic manipulations and fluorescent protein technology enabled detailed characterization of the endocytic pathways with a focus on their dynamics and the elucidation of the molecular machineries. Based on historical reasons endocytosis has been divided into two main groups: clathrin-dependent (CDE) and clathrin-independent endocytosis (CIE). CDE includes all of the endocytic processes in which the coat protein clathrin is recruited to the nascent

endocytic vesicle (coated pit). Although for many years it was believed that there was a single type of clathrin-coated vesicle, recently it has emerged that they differ regarding many other components such as adaptors, cargo proteins and the scission machinery [2]. CIE encompasses a broader set of endocytic processes such as caveolae-mediated endocytosis, raft-associated pathways, non-raft CIE pathways, macropinocytosis, phagocytosis and many others that, at the moment, are not fully characterized in terms of molecular machinery [3-5].

1.2 Role of the actin cytoskeleton in endocytosis

Actin dynamics plays a central role in processes that reshape the plasma membrane. Actin polymerization drives membrane protrusions in phagocytosis and macropinocytosis as well as in extending lamellipodia and filopodia [6]. It is also important in various modes of endocytosis where it is thought to provide the force necessary for membrane invagination, fission and vesicle transport away from the plasma membrane [7]. The dynamic association of the actin cytoskeleton at the sites of clathrin-dependent endocytosis was first shown in cultured mammalian cells [8]. Using total internal reflection microscopy (TIRF), the authors captured bursts of actin polymerization at the vesicle budding sites, which coincided with the recruitment of dynamin, a GTP-ase implicated in the scission of the endocytic vesicles from the plasma membrane. The same group later showed that Arp2/3, an actin nucleating factor that facilitates actin polymerization and branching, and N-WASP, a regulator of Arp2/3, transiently associate with both clathrin-coated pits and vesicles [9]. Rottner's group has recently demonstrated that the Arp2/3 complex is required for actin polymerization at the vesicle budding sites and that genetic ablation of N-WASP impaired EGF internalization [10]. Cortactin is another Arp2/3 activator that was shown to transiently localize at the sites of endocytosis [11]. Notably, dominant-negative and Arp2/3-binding cortactin mutant as well

as siRNA knockdown experiments revealed that it is required for both CDE and CIE [12, 13].

Experiments employing pharmacological agents that interfere with actin turnover provided some of the earliest evidence that actin cytoskeleton is important in endocytosis. In *S. Cerevisiae*, endocytosis was completely blocked by treatment with both Latrunculin A (LatA), which binds actin monomers and prevents actin polymerization, and Jasplakinolide (Jasp), which stabilizes actin filaments [14, 15]. However, in cultured mammalian cells such pharmacological treatments resulted in partial block of both, CDE and CIE in most cases [16, 17]. When examined in live cells via TIRF microscopy, both Jasp and LatA treatments interfered with multiple steps of CDE [11, 18]. Interestingly, in polarized MDCK cells, cytochalasin D (Cyt D), which caps the barbed ends of actin filaments and prevents their polymerization, inhibited all forms of endocytosis at the apical surface but not at the basolateral surface [19]. Furthermore, another study showed that the effects of LatA and Jasp on endocytosis varied depending on the cell type and whether the cells were grown in suspension or on rigid substrates [20]. This series of evidences suggest that the role of the actin cytoskeleton in endocytosis varies with the environment and the geometry of the cells calling into questions whether the experimental systems used thus far are appropriate to address these issues.

1.3 Regulated exocytosis

Secretory tissues are composed of specialized cells that use a variety of strategies to deliver molecules to the cell surface and the extracellular space. Molecules destined for secretion are synthesized in the endoplasmic reticulum, transported to the Golgi apparatus, processed, and sorted into membranous carriers that are constitutively released from the trans-Golgi network [21]. These carriers, that can be vesicular or tubular in shape, are transported in a cytoskeleton-assisted fashion to the cell periphery where they dock to the PM. This step is followed by the fusion of the two lipid bilayers and the formation of the fusion pore, which permits the release of soluble cargo molecules into the extracellular space [22]. This overall process, generally known as exocytosis, can be either constitutive or regulated. Constitutive exocytosis does not require any stimulus, whereas regulated exocytosis is triggered by specific extracellular signals that are transduced intracellularly by proteins at the PM, such as G protein-coupled receptors (GPCRs), tyrosine kinase receptors, and voltage-dependent calcium channels.

The modality and the kinetics of regulated exocytosis vary considerably among the numerous types of secretory cells, and interestingly, post-fusion events seem to be more diversified than pre-fusion steps. Indeed, after fusion with the PM, exocytic membranes can undergo three different processes: 1) full collapse, where they are completely absorbed into the PM [23], 2) kiss and run, where they detach from the PM after the initial opening of the fusion pore and the partial release of cargo molecules [24], and 3) compound exocytosis, where an exocytic membrane fuse with the PM (primary fusion event) serving as a docking site for other exocytic membranes (secondary fusion events) generating a string of interconnected vesicles (Fig. 1 A) [23, 25, 26]. This diversity in modality of regulated

exocytosis may reflect the fact that the organization of the PM, the morphology of the membranous carriers, and the nature of the cargo molecules, differ among the various secretory organs. For example, in neurons, neurotransmitters are released from the axon terminal into the synaptic cleft and reach the post-synaptic neuron; in endocrine glands, molecules destined to secretion are released at the PM into the extracellular space, diffuse through the stroma, and eventually reach the bloodstream; and in exocrine glands, molecules are released at specialized domains of the PM, typically the apical poles, which form ductal structures leading directly to the external environment (Fig. 1 B). Membranous carriers are also heterogeneous in shape, size and content. In neurons, the synaptic vesicles that transport small neuropeptides are 50 nm in diameter [27]; in chromaffin cells, secretory granules (SCGs) that contain catecholamines are 300 nm in diameter [28]; in salivary glands (SGs) and pancreas, the large SCGs transport polypeptides and reach a diameter of 1-1.5 µm. Finally, in endothelial cells, the Weibel-Palade bodies that transport large aggregates of the Von Willebrand factor have a peculiar cigar-like shape with a length of 1-5 µm and a diameter of 0.1-0.3 µm (Fig. 2) [29]. How this morphological heterogeneity affects the modality of regulated exocytosis is a fascinating question. It is clear that after the exocytic vesicles fuse with the PM, a physical continuity is established between two membranous environments with different biophysical features (e.g. lipid composition, membrane tension, or membrane mobility) [30]. Thus, it is reasonable to assume that each secretory system generates a specific exocytic vesicle/PM interface, whose unique properties may dictate not only the modality of exocytosis but also the kinetics and the machinery required to complete the process [31]. These differences in biophysical and geometrical constraints may determine

the deployment of different molecular machineries or a different use of the same molecule in order to optimize the exocytic process.

1.4 The role of actin cytoskeleton in regulated exocytosis

Actin cytoskeleton and its associated machinery has long been a subject of investigations in the field of regulated exocytosis. In endocrine and neuroendocrine cells actin seems to work as a barrier that prevents premature fusion of the exocytic vesicles. In exocrine cells, the role of actin has been more controversial. Indeed, in exocrine glands, apical canaliculi are marked by a dense meshwork of filamentous actin (F-actin) [32]. Orci and colleagues first postulated that the actin cytoskeleton could act as a barrier to membrane fusion and exocytosis of large SCGs [33]. Later studies confirmed that the meshwork of F-actin actin needs to be transiently depolymerized for the docking and fusion of the granules to occur [34]. In parotid acinar cells, treatment with Jasp drastically inhibited degranulation supporting the idea that F-actin turnover is required for exocytosis [35]. While depolymerization of actin by lower concentrations of LatA seems to induce granule instability and fusion, more extensive depolymerization leads to inhibition of stimulated secretion [34, 36]. This suggests that the presence of apical F-actin might be required for the transport of the granule to the site of fusion and to generate some mechanical force to facilitate this step. Indeed, actin filaments and the activity of non-muscle myosin II have been recently implicated in granule delivery and docking at the plasma membrane in lacrimal acinar cells [37]. Additionally, F-actin seems to be recruited on and stabilizes the docked granule, while non-muscle myosin II stabilizes the fusion pore in pancreatic acinar cells [36, 38]. However, the full understanding of the role the acto-myosin complex plays in regulated secretion is far from complete. Studies in pancreatic acinar cells suggest that the granules

release their cargo via “kiss-and-run” mechanism while actin provides stability to the fusion pore [39]. Conversely, secretory granules in the lacrimal gland and the parotid salivary glands are thought to fuse and collapse completely suggesting a different role for the acto-myosin complex.

It is important to emphasize that the different roles proposed for the actin cytoskeleton may reflect either differences in the organization of the various secretory cells or the possibility that actin plays multiple roles at the same time. However, in some instances contradictory findings have been reported using the same model, suggesting that the use of different assays, experimental conditions, or model systems may affect regulated exocytosis [34]

2. Experimental model systems to study endocytosis and exocytosis

So far both endocytosis and exocytosis have been studied primarily by using either cell cultures grown on two-dimensional (2D) surfaces (endocytosis and exocytosis) or a variety of *ex vivo* preparations (exocytosis). These systems offer several advantages, such as a tight control of the experimental conditions, which results in high reproducibility, the possibility of performing genetic and pharmacological manipulations, and finally the use of a wide range of assays based on biochemistry, electro-physiology, and electron and light microscopy. Specifically, *in vitro* and *ex vivo* model systems have been the only choice to perform time-lapse imaging and thus to acquire information on the dynamics of both endocytic and exocytic processes. However, there are some legitimate concerns regarding how well such simple systems represent cell behavior in complex multicellular organisms. 2D cell cultures lack essential components that are characteristics of cells in their native

tissue: three-dimensional (3D) architecture, interactions with other cells, extracellular matrix, and signaling molecules. Another issue is that when cells are isolated from a tissue they may loose their specialization, polarity, and membrane organization. Finally, it is known that metabolic state, protein expression and turnover in cultured cells may be altered from the native tissue [40].

Endocytosis has been primarily studied in 2D systems and limited data have been generated in *ex vivo* or *in vivo* systems. As a consequence, many fundamental questions about the machinery regulating endocytosis are still unanswered. For example, we do not know much about which cell types carry out which type of endocytosis for most cargoes *in vivo*. There have been several studies in live animals using electron microscopy that have identified clathrin coated pits or caveosomes at the cell surface. However, these studies did not provide any dynamic information on the internalization and the subsequent steps in endosomal trafficking and in many cases the cargoes were not identified.

As for exocytosis, cultured cells have been used extensively to study endocrine and neuroendocrine secretion. The use of spinning disc or TIRF has made it possible to follow small vesicles (50-100 nm) that exocytose very rapidly (in the order of milliseconds, Fig. 2), and to investigate various aspects of exocytosis, such as the release of cargo proteins and the dynamics of the fusion pore [41]. For example, extensive studies have been performed on: exocytosis of the glucose transporter 4 (GLUT4) in primary rat adipocytes [42, 43] , dense core vesicles in bovine chromaffin cells, PC12 cells, and primary cultured hippocampal neurons [41, 44, 45], lytic granules in cytotoxic T lymphocytes [46], insulin granules in pancreatic beta cells [47], and Weibel-Palade bodies in human endothelial cells [48]. The field of exocrine secretion has relied extensively on preparations derived from explanted

organs, such as intact isolated acini or ducts. Since these *ex vivo* preparations are thicker than a single layer of cultured cells, regulated exocytosis has been imaged using either confocal or two-photon microscopy [25, 49]. Successful models have been established for SGs, pancreas, adrenal medulla, and lacrimal glands, where purified acinar preparations have provided groundbreaking information on the kinetics of exocytosis and the identification of some of the molecular components regulating these processes. Most of the studies were carried out by bathing acinar preparations in small fluorescent dyes, such as low molecular weight dextrans or sulphorhodamine-B, which accumulate in the extracellular space and upon the opening of the fusion pore access the SCGs. This approach has revealed that in most exocrine glands, SCGs primarily undergo compound exocytosis [25, 26, 50-53]. It is important to note that these preparations are based on the use of mechanical and enzymatic procedures that may have adverse effects on the response to exocytic stimuli. Furthermore, although some aspects of the architecture of the intact organs are maintained, other structural components are missing, such as extracellular matrix, supporting cells surrounding the acini, and ductal structures. Some of these shortcomings have been solved with the use of lobule preparations and tissue slices, where the architecture of the intact organ is locally preserved. The former model, has been instrumental in elucidating the complex nature of secretory pathways in SGs, whereas the latter, originally developed and used in neuroscience, have been particularly helpful to study multiple aspects of regulated exocytosis both in pancreas and in SGs [54, 55]. However, although both systems are the closest to *in vivo* models, they still lack the contribution from signaling molecules provided by the vasculature and the nervous system. Particularly, the latter may have a profound influence on the response to excitatory

stimuli, since denervation in live animals results in alterations in both the morphology and the exocytic capacity of the secretory apparatus, as shown in several studies [56].

Regulated exocytosis has also been extensively investigated in live animals, such as small rodents, relying on two main approaches: 1) the quantitative measurements of the amount of a given secreted molecule through the use of either biochemical or radio-immuno assays, and 2) electron microscopy, which has revealed the ultrastructure of the secretory apparatus. Although, these powerful approaches have provided biochemical and structural information on regulated exocytosis, they did not offer any insight on the dynamics of single exocytic events.

3. Intravital microscopy

To overcome the limitations of the *in vitro* and *ex vivo* models, a large effort has been directed towards developing techniques and tools to image and study cellular events in living animals, with the goal of achieving the same depth of analysis that is currently available for *in vitro* models.

Although in live animals organs have been imaged since the early 1930s [57], the major breakthroughs in this field occurred in the last decade with the improvement of conventional microscopes. Further improvement was achieved by development of microscopes based on the "non-linear" excitation of the specimen, which has opened the door to deep tissue imaging [58-60].

3.1 Non-linear optical microscopy

Non-linear optical microscopy techniques generate contrast using higher-order interactions between light and biological matter. Processes whose dependence from the

incident light is non-linear typically involve the absorption or the scattering and recombination of two or more photons by the specimen [58-66].

3.1.1 Two- and three-photon microscopy

The theoretical formulation of multi-photon excitation was proposed for the first time by Maria Goppert-Mayer [67]. However, it took 30 years to be experimentally proven with the invention of the first laser, and almost 60 years for the first multi-photon microscope to be built [68]. Two- (three-)photon excitation is based on the fact that a molecule of a fluorophore can be excited by the almost simultaneous absorption (between atto- and femto-seconds, 10^{-18}–10^{-15} s) of two (three) photons that have half (a third) of the energy that would be required to fill the gap between two of its energetic levels (Fig. 3 a, b) [58, 60]. This implies that multi-photon excitation requires near infrared light (NIR) or infrared light (IR) that have the ability to penetrate biological tissues deeper than UV or visible light, making it the ideal choice for deep tissue imaging [69]. Indeed, whereas in single confocal microscopy biological specimen can be imaged up to a depth of 50–60 μm, in multi-photon microscopy (MPM) this range can be extended up to 1 mm either by using tissues that exhibit a lower light scattering such as the brain [70] or by utilizing longer excitation wavelengths [71]. The probability of multi-photon transitions to occur is extremely low and requires very high light intensities concentrated in space and time. This is achieved using lasers that emit NIR/IR light in very short pulses (typically in the order of 100 fs) at high repetition rates (80–100 MHz), and using high numerical aperture lenses that focus the light to the excitation spot. In ideal conditions the absorption and the emission occur in a very small volume (1 fl) [58, 60] reducing significantly both photo-toxicity and photo-bleaching. Furthermore, this avoids the issue of off-focus emission, which in confocal microscopy is eliminated through

the use of a pinhole (Fig. 3 e). Finally, another important feature of multi-photon excitation is that for all the fluorophores characterized so far, the absorption spectra are much broader than in single photon excitation. This enables the imaging of multiple fluorophores using a single excitation wavelength (Fig. 3 f) [72, 73].

3.1.2 Second and third harmonic generation microscopy

Second harmonic generation (SHG) and third harmonic generation (THG) are processes that do not involve any energy absorption since the incident photons are scattered, recombining into a single photon in a process without energy loss (Fig. 3 c). For this reason they are suitable for imaging biological specimen with even lower photo-toxicity than MPM [61]. Although the major harmonic signals are produced in the forward direction and thus more suited for imaging slices, the backward scattering signal is still sufficient for imaging thick tissue in live organisms. Several molecules are able to generate harmonic signals, especially when assembled in highly ordered structures. Among them are collagen, microtubules, and muscle myosin [61, 74, 75]. Recently, lipids forming lipid bodies have also been successfully imaged in various living organisms using THG [76]. Due to the different nature of the harmonic emission, SHG and THG are often combined with MPM, expanding the repertoire of information that can be acquired. Recently, using spectral un-mixing techniques, up to six intrinsic signals coming from both multi-photon and harmonic emissions were resolved, providing very detailed information about the architecture of the skin in live nude mice [77].

3.2 Imaging tissue architecture and function *in vivo*

3.2.1 Intrinsic or endogenous fluorescence

Several endogenous molecules are excited using either non-linear optical techniques or single photon microscopy, providing valuable information on the tissue architecture without the need for exogenous labeling [74]. Although several studies have been performed utilizing endogenous emissions in explanted tissues, only few have been carried out in live animals. One of the molecules that has been exploited for this purpose is NAD(P)H that emits in the visible range upon either single photon (360 nm) or two-photon excitation (710–760 nm). Although its two-photon cross-section is very low, its abundance within the cell makes it a suitable endogenous label for both metabolic and structural studies. Changes in the levels of NAD(P)H were measured in live mice during ischemia and reperfusion in the jejunum [78], microcirculatory failure in the liver [79] or in the kidney after LPS-induced sepsis [80], providing novel data on the metabolic state of the tissue under pathological conditions. Recently, levels of NAD(P)H were measured in the skin and in the liver using FLIM [81]. NAD(P)H is distributed both in the cytoplasm and in the mitochondria, and at a relatively low magnification, its signal highlights the details of the architecture of various tissues [82-84]. Another molecule whose intrinsic fluorescence has been exploited for *in vivo* imaging is collagen, which when arranged in fibers generates a strong SHG signal [61, 75, 82-84]. Due to its very low turnover and stability, several studies have been focusing on analyzing the architecture of collagen fibers in various explanted organs under both physiological and pathological conditions [85-89]. Moreover, imaging collagen fibers in live animals has proven to be a valuable reference point within the tissue, particularly in the context of tumor migration and invasion where an important issue is to correctly locate and orient tumors that are repeatedly imaged over a long period of time [90-92]. Furthermore,

imaging the organization of collagen fibers has been extremely valuable in studies related to skin diseases both in live rodents and in patients [93]. Finally, in order to highlight various structural features in live animals, other molecules have been imaged using different modalities, such as elastin in the skin (MPM), myosin fibers in the skeletal muscle (SHG), myelin fibers in the corpus callosum (CARS, Fig. 3 e) or lipid-enriched structures (CARS) [83, 93-95]. As shown in subsequent chapters, native signals from NAD(P)H and collagen have been instrumental in enabling us not only in understanding of overall structure of SGs but also to orient ourselves in the right 3D space of the live tissue for a given experiment. Some examples of the parenchyma highlighted by NAD(P)H signals in various tissues are given in figure 4 a-i.

3.2.2 Exogenous labeling of the tissues

Another approach to image tissue architecture and function is to either administer exogenous dyes or to genetically introduce fluorescent proteins selectively targeted to the tissue of interest. For example, systemic injections of fluorescently labeled bovine serum albumin (BSA) or dextrans of different sizes have enabled studying and measuring both glomerular filtration and tubular reabsorption in the kidney [96-98]. In the pancreas of live mice, by imaging with a millisecond temporal resolution, blood flow patterns were determined in the islet vasculature bed [99]. This approach has been used extensively in neuroscience where vasculature flow has been imaged and measured either in normal conditions or under acute ischemic damage in the brain cortex [45, 70, 100] or in the olfactory bulb [101-103]. Imaging the vasculature both acutely and chronically has been an extremely important tool in the context of cancer biology to address key questions such as the contribution of the local microenvironment to tumor-induced angiogenesis [104, 105],

tumor-induced vascular permeability [106], and to follow the bio-distribution of drugs or other molecules in the tumoral mass [107, 108]. Moreover, exogenous dyes can also be locally administered in different tissues to highlight various structural features. For example, sulforhodamine B has been injected into the muscles of mice to image elastin fibers, or to selectively stain the astrocytes in the brain [109, 110]; curcumin and metoxy-04 has been injected to label amyloid plaques in tg2576 mice, a model for Alzheimer's disease [111, 112]; and Ru(phen3)2+ has been used to image the level of oxygen in the liver [79]. Finally, significant information about the architecture of tissues *in vivo* has been generated through the use of transgenic models expressing fluorescent reporters under the control of specific tissue promoters. The field of neuroscience has pioneered this approach with the generation of mice with specific neuronal populations expressing GFP or YFP, and recently, using a combinatorial strategy, the so-called "brainbow" mice were generated in which neurons are labeled with different colors, providing an experimental tool to analyze the neuronal circuitry [66, 113]. The use of fluorescent transgenic models is now rapidly expanding to address biological questions in other fields. For example, mice have been generated to image the pancreatic beta cells [99], the endothelium in various organs such as the kidney and the spleen, or in the presence of implanted tumors [114-116], and many more are becoming available. In the coming chapters we will present how we applied such exogenous fluorescent labeling techniques and transgenic animals to label various components of the SG down to separate organelles that enabled us to follow membrane trafficking events *in vivo*.

3.3 Imaging single cells *in vivo*

The ability to follow the fate of single cells over time within a given organ in live animals has contributed to major breakthroughs in fields such as cancer biology, immunology, microbiology, and recently in stem cell research. In cancer biology, several experimental systems have been developed to track the motility of cancer cells within a tumor *in vivo*. For example, mammary tumors have been imaged *in situ* in mice models highlighting the role of the macrophages during the intravasation process [92, 117], and the migration of highly invasive melanomas have been tracked dynamically, leading to the determination of interesting correlations between the differentiation state of the cells and their migration ability [118, 119]. Imaging the cells of the immune system in a live animal has revealed novel aspects of the dynamics of cellular immunity. Most of the experimental systems are based on transferring of fluorescently labeled isolated cells into recipient animals. From the first pioneering studies looking at the movements of B lymphocytes and T cells in the intact lymph-nodes [120-124], a number of immunological questions have been addressed, spanning from T cell activation [122, 125], the formation of mycobacterium-induced granulomas in the liver [126], T cell infiltration and elimination of solid tumors [127, 128], migration of dendritic cells [129], and the extrafollicular activation of B cells [130]. Another field that has benefited from the development of IVM microscopy is the biology of pathogen infection. One of the first studies conducted to image the progression of bacterial infections in live tissue was performed in the kidney, where the proliferation of a GFP-expressing uro-pathogenic Escherichia coli was studied [131]. Several other studies were performed using different approaches and strategies to image either later stages of the infectious process or focusing on the site of the infection [132, 133]. Finally, IVM has been

recently utilized in stem cell research to track individual hematopoietic stem cells over time in the calvarium bone marrow of living mice, thus opening the field to new and exciting discoveries [134].

3.4 First breakthroughs in imaging subcellular structures in live mammals

In a live animal, one of the issues for subcellular resolution imaging is the decline of signal to noise ratio as the depth and the light scattering properties of the tissue increase. Clearly, this can be remedied by choosing a model organ with an easy access to the cells of interest close the surface of the organ or by choosing less optically dense tissues such as the brain. Another major challenge in performing imaging at a subcellular level is represented by the motion artifacts due to the respiration and the heartbeat. The use of stereotactic devices that completely immobilize the head of the animal has been instrumental in achieving this high level of resolution in the brain. Indeed, the first structures that were resolved *in vivo* at a submicron resolution were the dendritic spines that can be imaged for over a month in transgenic mice expressing YFP or GFP in a subset of layer V pyramidal neurons [66, 135, 136]. In the last few years, both surgical procedures and novel devices ensuring the stabilization of other organs have been developed. The first application of IVM for the imaging of fast moving intra-cellular organelles in organs other than the brain was pioneered by the Molitoris group who has studied the internalization of fluorescently labeled dextrans and folic acid in the externalized kidney, also establishing methodologies to extract quantitative information [137-139]. Exocytosis has also been imaged in the kidney, where the release of renin from the granular cells of the glomeruli was studied using quinacrine to label a population of secretory granules [140]. Other subcellular compartments, such as mitochondria, were imaged dynamically in live animals either in the liver during ischemia–

reperfusion using Rhodamine123 [141], or in the kidney using tetra-methyl rhodamine methyl ester (TMRM) [142]. However, these studies only achieved relatively short imaging times, while the motion artifacts and the lack of resolution have hindered the observation of fine details of subcellular events such as organelle fusion and fission.

MATERIALS AND METHODS

1. Multi-photon microscopy

An IX81 inverted confocal microscope (Olympus) was modified to perform MPM (Fig. 5). A tunable Ti:Sapphire femtosecond laser, Chameleon Ultra II (Coherent), was used as laser source, and the power was modulated using a combination of neutral density filters (Chroma Technologies). The size of the beam was modulated using a beam expander (LSM Technology Inc.) and directed into a Fluoview 1000 scanning head (Olympus). The emitted signal was directed into a custom-made array of three non-descanned detectors that were installed on the right port of the microscope (LSM Technology). A 680-nm barrier filter (Chroma Technologies) was used to prevent the scattered IR light to reach the detectors. The three cooled photo multipliers (PMTs) were purchased from Hamamatsu (R6060-12), and the two dichroic mirrors and the barrier filters were purchased from Chroma Technologies. Hoechst, the endogenous fluorescence and the second harmonic signal were detected on the first PMT (dichroic mirror 510 nm, barrier filter 400–480 nm). FITC and Alexa 488 were detected on the second PMT (dichroic mirror 570 nm, barrier filter 505–560 nm), and Texas-Red was detected on the third PMT (barrier filter 590–650 nm). To enhance the detection of the endogenous fluorescence, the barrier filter was removed. The excised glands were imaged in the inverted setting, while time-lapse imaging on the live animal was performed in both, the inverted and the upright configurations using an objective inverter (LSM Technology) for the latter (Fig 6 E-L). All the time lapse sequences in MPM mode were acquired using a

UPLSAPO ×60 numerical aperture (NA) 1.2 water immersion objective or XLUMPFL20XW ×20 NA 0.95 water immersion objective (Olympus America). More detailed description of the MPM setup was previously published elsewhere [143].

2. Confocal microscopy

Intravital microscopy was also performed in confocal mode using the same IX81 inverted confocal microscope equipped with a Fluoview 1000 scanning head (Olympus America). DAPI and Hoechst 33342 nuclear dyes were excited by 405 laser; GFP and Alexa-488 were excited with a 488 nm laser; m-Tomato, Texas Red-Dextran, Cy3, DiI, Mitotracker Red, Lysotracker and TRITC were excited with a 561 nm laser; and Alexa-567 dye was excited by 633 nm laser. For the time-lapse imaging, the acquisition speed ranged from 0.2 to 1 sec/frame and the thickness of the optical slices was optimized to reach either 0.8 to 1.2 μm (Fig. 17). The images and time-lapse series were acquired using a UPLSAPO x60 numerical aperture (NA) 1.2 water immersion objective or Plan-Apo 60x / 1.42 NA oil immersion objective (Olympus America). The optimal focal plane for imaging was chosen between 10 and 15 μm from the surface of the glands (Fig. 18). During the acquisition of the time-lapse sequences occasional drifts in the Z-axis and in XY axis were corrected manually.

3. Animal preparation and gene transfection

All the experiments were approved by the National Institute of Dental and Craniofacial Research (NIDCR, National Institute of Health, Bethesda, MD, USA) Animal Care and Use Committee. Sprague–Dawley male rats weighing from 150–250 g, mice of C57 Black 6 and Friend virus B-type (FVB) background weighing 20–40 g were fed ad libitum.

FVB transgenic mouse lines expressing EGFP (GFP-mice) or C57BL/6 expressing the membrane-targeted Tomato protein (m-Tomato mice) were purchased from the Jackson Laboratory and bred as homozygous. The expression of both transgenes was driven by the chicken β-actin promoter and cytomegalovirus enhancer. The two lines were crossed to generate mice expressing both transgenes (GFP/m-Tomato mice). Myosin IIb-GFP and Myosin IIa-GFP mice were a generous gift from Dr. Adelstein (NHLBI, NIH) and were previously described [144]. GFP-Lifeact and RFP-Lifeact transgenic mice were a generous gift from Dr. Roland Weldich-Soldner and were described previously [145]. Animals were brought into the lab from the vivarium at least two days before the experiment, fed chow and water *ad libitum,* and allowed to acclimate in the new environment to prevent stress-induced secretion that may affect the outcome of the experiments [146].

A general flowchart of experimental procedures can be seen in Figure 7. However, in some cases the fluorescent dyes were injected during imaging. Additionally, in some cases, and especially when imaging transgenic animals, no exogenous labeling was applied. The animals were anesthetized by an intraperitoneal injection of a mixture of ketamine and xylazine (100 and 20 mg/kg, respectively) with additional injections as needed. For delivery of fluorescent probes, pharmacological agents and DNA into the Wharton's duct, a fine polyethylene cannula (PE5 or PE8) was inserted in the orifice below the tongue using tweezers (Fig. 6. A-C). The procedure has been described previously [147]. The cannulae were inserted for 0.2–0.5 cm and sealed with glue. The volume injected did not exceed 50 μL per rat SG, and the injections were performed very slowly to prevent damaging the glands. LifeAct-GFP or RFP plasmids were a generous gift from Dr. Tamas Balla (NICHD, NIH). Farnesyl-GFP or RFP plasmids were a generous gift from Dr. Julie Donaldson, (NHLBI,

NIH). For the systemic injections of fluorescent probes, the tail artery was surgically exposed, and a small incision was performed to insert a fine catheter connected to a 1-mL syringe. The tail was sutured, and small amounts of saline (100–200 μL) were injected as needed (Fig 6 D). Unless otherwise specified, the rats were injected with the following amount of fluorescent probes: 200 μg 70 kDa Texas Red Dextran (TXR-D), 200 μg 70 kDa 488-D, 40 μg 500 kDa FITC-D and 10 μg of Hoechst 33342 (Invitrogen). All the fluorescent probes were purchased from Invitrogen and diluted in sterile saline at the appropriate concentrations in a volume not exceeding 200 μL.

Imaging was performed either in the inverted or upright configuration based on the resolution and fluorescence signal constrains for a given experiment (Fig. 6 E-L). For the upright configuration the animal is stabilized on a platform with a custom-made holder that accommodates a SG and a coverslip. After the platform is situated on the microscope stage the heated objective is brought on top of the gland. For the inverted setup, the externalized SGs were accommodated on a coverslip mounted on the stage above the objective. The SGs and the body of the animal were immobilized using custom-made holders. Particular care has to be taken in controlling that the blood flow is not significantly reduced as a consequence of possible excessive pressure applied on the tissue. This can be assessed by visually looking at the flow of the erythrocytes in the vessels close to the acinar structures. All secretogues were injected subcutaneously (SC) into the dorsal side of the animal. To couple the sample to the objective, a carbomer-940-based gel (Snowdrift Farm) was prepared and used as described previously [84]. The temperature of the externalized glands was maintained using the objective heater (Bioptechs), and the temperature of the body of the animal was maintained a chemical heating pads “Foot Warmers” (Heat Factory), which were

purchased from the Amazon.com website. It is important to note that controlling the appropriate temperature (around 37˚C) is needed to overcome this major source of variability for IVM based experiments.

4. Administration of drugs

Drug treatment or vital dye staining was carried out by externalizing the SGs and bathing them in custom made cups that held 0.5 ml and 1.5 ml of working solution for mice and rats, respectively. Selective SG drug treatment allowed avoiding possible systemic effects. When SGs were treated with pharmacological agents while imaging in the inverted configuration, a nylon mesh was placed between the glands and the coverslip to facilitate the access of the fluid to the exposed tissue and the drug volume of 1 ml was slowly infused with PHD Ultra Nanomite syringe pump (Harvard Apparatus). (+) and (-) Bleb (EMD Chemicals), Cytochalasin D (EMD Chemicals) or Latrunculin A (Sigma-Aldrich) were administered at the appropriate concentration in saline. 0.5 % DMSO was used as control.

5. Immunofluorescence

Immunolabeling was carried out using cryosections or whole mounts of the SGs as described previously [148] with the following modifications. To preserve the sub-cellular architecture of the acinar cells, the SGs where rapidly fixed by performing cardiac puncture and perfusing the animals a with normal saline immediately followed by 4% formaldehyde, 0.05% glutaraldehyde and 0.2 M HEPES buffer, pH 7.3. The fixed tissue was stained with TRITC-Phalloidin (Sigma) and Alexa 488-Phalloidin (Invitrogen). The primary antibodies used in this study were the following: rabbit anti-vimentin (Dako) and rabbit anti LAMP-1

(Abcam). As secondary antibody, we used Alexa 488-goat anti-rabbit Immunoglobulin G (Invitrogen). Staining with antibodies against nonmuscle myosin IIa or IIb (Covance) was performed on cryosections that were fixed with acetone at -20°C for 20 min.

6. Toluidine blue staining

Animals were anesthetized as described above. Secretagogues or saline were injected SC and the animals were euthanized at the appropriate time by cardiac puncture and perfusion of a fixative solution as described above. SGs were removed and placed in fixative for an additional 24 hours. The tissue was embedded in paraffin and 3 µm sections were cut. After rehydration, the sections were incubated in 2% Toluidine blue in water for 1 minute, washed in water for 2 min, dehydrated in acetone, cleared in xylene and mounted. Pictures were taken in brightfield mode using a 100x oil immersion objective.

7. Image processing and analysis

Quantification of degranulation, fluorescence intensity and granule diameter measurements were carried out using Metamorph (Molecular Devices). To quantify the number of the SCGs, time-lapse image stacks were processed with the H-basin morphology filter, which enhances granule-like objects and inverts the image contrast. The granules were manually counted at 0, 2.5, 5, 10, 15, 20, 25 and 30 minutes after the injection of either Iso or Carb (Sigma-Aldrich) and normalized for the number of the granules at time 0 (100 %). The co-localization between m-Tomato and actin in the SCGs was assessed using Imaris (Bitplane). Z stacks were acquired from phalloidin-stained whole-mounted SGs and analyzed both manually by using the ortho-slicer function. Each granule was scored for the

presence or absence of actin and m-Tomato. We have analyzed Three acini were analyzed per animal, for a total of 3 animals. Fluorescence intensity from time-lapse data sets were measured using the region measurement toolbox. The change in granule or canaliculi diameter over time was measured using the kymograph tool. For the supplementary movies, image registration was performed using the Stackreg plug-in from Image J (W. Rasband, National Institutes of Health). When needed, the background noise was reduced by applying to each image one or two rounds of a 2x2 pixel low-pass averaging filter in Metamorph. Brightness, contrast and gamma correction were applied as needed. Volume rendering was performed using Imaris (Bitplane). Data analysis and graphing was done in Microsoft Excel. The final preparation of the images was conducted with Photoshop CS (Adobe).

RESULTS AND DISCUSSION

1. Setting up the intravital imaging system

In order to study membrane trafficking in living mice and rats we had to overcome some of the challenges inherent to imaging the living tissue, such as motion artifacts and signal degradation due to the imaging depth. As a model organ, we used the SGs of live rats, which offer several advantages. First, they can be exposed by a relatively minor surgery and easily immobilized to minimize the motion artifacts that are detrimental to high-resolution imaging. Second, SGs are a quite homogeneous tissue form the depth perspective, whereby most of the specialized cell types of the organ can be reached at relatively shallow depths (10 to 30 µm). Third, SGs are amenable to both pharmacological and genetic manipulations making these organs ideal to study cellular processes at a molecular level. Indeed, various molecules can be delivered to SGs through multiple routes: 1) via systemic injection, 2) via intra-organ injection, 3) via bathing of the organ in a solution, and 4) via the salivary ducts that can be accessed from the oral cavity. Specifically, this last route has been utilized to deliver plasmid DNA, enabling us to transiently express fluorescently tagged proteins in the parenchyma of SGs.

To minimize the motion artifacts we designed holders to accommodate the SG in both the inverted and the upright configuration (Fig. 6 E-L). The upright configuration in the inverted microscope was achieved by using an objective inverter / extension arm from LSM Technologies. Although this setup allows for the easiest access to the SGs, the inverted configuration results in a more efficient imaging because of the lower number of components

in the optical path. Therefore, the inverted setup was preferred for experiments where the highest resolution was desirable. For the upright configuration the exposed SG was placed in the holder, immersed in the optical coupling gel and secured by a glass coverslip. The heated objective was brought onto the coverslip using the objective inverter (Fig 6 H, I). Similarly, the SG was secured onto a coverslip with a custom-made holder in the inverted configuration (Fig 6 L). The animal temperature was closely monitored by a thermometer and maintained by a chemical heating pad.

1.1 Imaging the structure and dynamics of the salivary glands via endogenous fluorescence and fluorescent probes

First, we determined whether we could use MPM to image the architecture of rodent SGs and other organs. To this aim, we imaged the SGs using excitation wavelengths between 980 and 1000 nm. In both rats and mice we found that the architecture of the SGs was revealed when the laser was tuned between 730 nm and 750 nm (Fig. 8). This emission most likely represent NAD(P)H molecules as shown by others [74]. Large elastic fibers were detected exciting the specimen between 800 nm and 960 nm and most likely representing a combination of 2P and SHG signals (Fig. 8). We performed 3D reconstructions of the gland by acquiring sequential images along the Z-axis from the surface up to 70-100 µm. The very same area was first imaged exciting at 750 nm (Fig. 9 grey) and then at 900 nm (Fig. 9 green). Due to their distinct morphology, the acini and the ducts were easily identified (Fig. 9 arrow and arrowheads, respectively). Furthermore, some structural features such as the acinar canaliculi or the mitochondrial-enriched basolateral pole of the granular convoluted tubules have also been imaged at a level of resolution comparable to that obtained by classical immunohistochemistry (Fig. 9 and fig. 4 i-j) [147, 148].

Next, we determined whether we could dynamically image the parenchyma of the SGs and visualize the vasculature in the live animal using endogenous fluorescence and exogenous fluorescent probes. To highlight the vasculature, 500 kDa FITC-dextran (FITC-D) was injected into the tail artery. Almost instantly, the dextran filled the vasculature where it was retained for the entire duration of the experiment (Fig. 10). The same experiment was performed highlighting the nuclei by injecting Hoechst 33342 prior to the injection of 500 kDa FITC-D (Fig. 10). Furthermore, we were able to image the vasculature in the rat liver and the brain, glomerular filtration in the kidney and kidney and SGs (Fig. 1.4 k-m). We also found that fluorescent dye can be retro-infused by gravity into the salivary ducts of rats to image dynamically the ductal system (Fig. 4 n). This method is capable of revealing an intricate network of ducts and canaliculi at the same time highlighting the apical pole of the epithelial cells [147-149].

Next, we attempted to image membrane trafficking for extended periods of time in the SGs. To this aim we used two strategies: 1) systemic injection of low molecular weight dextrans that diffuse out of the vasculature and are internalized by adjacent cells revealing the endosomal system, and 2) labeling of subcellular organelles, such as mitochondria, using specific vital dyes. First, we injected a combination of dextrans of different molecular weights (500 kDa FITC-D and 70 kDa Texas Red-dextran (TXR-D)) and imaged the exposed glands by two-photon microscopy. Both dextrans appeared almost immediately in the vasculature (Fig. 11a) with the 70 kDa TXR-D diffusing in the stroma and being internalized by cells (Fig, 11a). Notably, the process was imaged for 14 minutes at a scan speed of one frame per second. In a second experiment, we injected Alexa 488-dextran and bathed the exposed glands with Mitotracker to reveal mitochondria. A single stromal cell was imaged in

time lapse. Since this cell was located close to the surface of the glands we used confocal microscopy that exhibits a higher spatial resolution. Indeed, we could observe the dynamics of single mitochondria and catch fusion events between the endosomes (Fig 11 b). This experiment suggested that when the cells of interest are located in the first 10–30 μm from the surface of the organ, single photon confocal microscopy can also be used, enabling imaging at a higher resolution than MPM (compare Fig. 11 a and b).

1.2 Gene delivery salivary gland epithelial cells

A major breakthrough that has allowed extending IVM to many other areas of cell biology is the ability to rapidly transduce fluorescently tagged genes in specific cell populations of the organ of interest. One of the first studies in this direction was aimed at studying the actin cytoskeleton and was performed in the endothelial cells of the kidney that were transduced with either GFP-actin or GFP-cofilin using micro-puncture techniques and adenoviral vectors [150, 151]. Successful gene delivery to other organs such as skeletal muscle, liver and brain has been reported in live rodents [152]. Recently, using the SGs and plasmid DNA, we have shown that genes can be selectively targeted and robustly expressed in the different subpopulations of cells forming the parenchyma of the salivary glands [147] (Fig. 11 c–e). Using high-resolution two-photon microscopy, different subcellular organelles were imaged dynamically such as clathrin-coated vesicles, the trans-Golgi network (Fig. 11 c, e), and early endosomal compartments, with a resolution comparable to that achieved in cell culture by single photon confocal microscopy. Furthermore, the dynamics and the distribution of various molecules such as the GFP-Lifeact (Fig. 11 d, e) and Aquaporin 5 – GFP (Fig. 11 c) was also analyzed, showing that this technology can be applied to address and study different cellular processes.

2. Intravital imaging of endocytosis

We have shown that systemically injected molecules diffuse out of the vasculature and are rapidly internalized by a series of cells in the salivary glands. An important question was to determine the nature of these cells. To this aim, 70 kDa TXR-D was injected into the tail artery and after 1 hr the SGs were imaged by TPM. A Z-stack of images revealed that two distinct populations of cells internalized dextran: one that is embedded within the elastic fibers (Fig. 12 A1) and the other that is located in the stroma around both acinar and ductal structures (Fig. 12 A2). As shown in Figure 12 B, both populations of cells were positive for vimentin suggesting that they are fibroblastic in nature, although other cell types such as dendritic cells could not be completely ruled out. We also compared the uptake and trafficking of fluid-phase markers with those of molecules such as transferrin that are internalized via receptor-mediated endocytosis. Surprisingly, we observed the early endosomes containing labeled dextran as early as 2-5 minutes after injection whereas transferrin internalization and accumulation was markedly slower and appeared only 10-15 minutes after probe injection (Fig 12 D). Furthermore, a significant fraction of transferrin-positive endosomes overlapped with dextran labeled endosomes. In contrast, the isolated salivary gland fibroblasts exhibited very rapid kinetics of transferrin internalization and showed no significant overlap with dextran-labeled endosomal-lysosomal system, as previously reported (Fig 12 E). Moreover, dextran internalization was markedly slowed down and mostly relied on macropinocytosis in cultured fibroblasts. This experiment provides a compelling evidence that cultured cells do not always reflect the behavior of cell in their physiological environment. Although it would be tempting to investigate the reasons

of these discrepancies, we sought to continue our characterization of the endocytic pathways *in vivo*.

Next we determined the kinetics of the fluid phase cargo trafficking through the various endocytic compartments in more detail. To this aim, we first intravenously injected the rats with TXR-D to load the lysosomal compartment, and after 24 h, we injected 70 kDa Alexa 488 dextran (488-D) to image the early endosomal compartments. The glands were removed at different times after the injections of 488-D and imaged as described above. As expected, TXR-D accumulated in lysosomal structures labeled by the late endosomal/lysosomal marker lysosomal-associated membrane protein 1 (LAMP-1) [153] (Figure 13 A). After 20 min from the second injection, 488-D was present in early endosomes. This was determined by two lines of evidence: first, 488-D-containing endosomes did not overlap with the late endosomes/lysosomes containing TXR-D (Figure 13 B, top panel) and second, the 488-D-containing endosomes were not labeled by LAMP-1. After 30 min (Figure 13 B, lower panel, arrowheads), a significant overlap was observed, and after 60 min, most of the 488-D dextran reached the late endosomal/lysosomal compartment (data not shown). Notably, the progression of the cargoes from the early endosomes to the late endosomes/lysosomes is consistent with that reported for cultured cells [154]. To image the fusion events between the various endosomal compartments dynamically, we set up a time-lapse acquisition upon the second injection of 488-D. After 5 min from the injection, the 488-D appeared in small peripheral early endosomes (Figure 13 C, time 7:00), which did not reach the lysosomal compartment but increased in size in the first 20–25 min (Figure 13 C, time 15:00 and 25:00,). The size of the endosomes increased because of homotypic fusion events as shown in Figure 13 D where two small early endosomes came in contact and fused,

generating a larger endosome that did not contain any TXR (Figure 13 D, arrowheads,). These fusion events are not always obvious because they occur within 3 seconds, a time that is very close to the time interval between each frame of the time-lapse sequence. At later time-point, we detected fusion events between larger endosomes containing only 488-D. These structures most likely represent late endosomes because they overlapped with LAMP-1. Notably, we did not observe any direct fusion events between endosomes containing 488-D and lysosomes containing TXR-D. Instead, the 488-D-containing endosomes gradually acquired TXR-D (Figure 13 E, time 55:00 versus time 56:38, insets and arrowheads) and then fused with another endosome containing both 488-D and TXR-D (Figure 13 E, time 57:57 and 58:14, inset and arrow). Because of the limit in the resolution of TPM, we could not determine the mechanisms by which the 488-D acquired the TXR-D, which most likely implicates some transient connections as previously described by Luzio and colleagues [154].

We have shown that the trafficking of probes through early endosomes and late endosomes/lysosomes can be studied in live animals. However, an important prerequisite to study the molecular machinery regulating these processes is the ability to perturb this system. In this regard, the Wharton's duct provides a direct route to deliver drugs into the submandibular glands. This avoids systemic injections, which might lead to broader non-specific effects to the entire animal. To check how effectively molecules can be delivered throughout the SGs, a fine polyethylene cannula was inserted into the Wharton's duct (Figure 14 A). The 488-D was injected through the cannula. Almost immediately, it appeared in large circular structures that most likely represent the cross sections of the large ducts (Fig. 14 B,C, arrow). Immediately after injection, 488-D appeared in small ducts and in the acinar canaliculi (Fig. 14 B,C, arrowheads). To test whether drugs delivered through this route

would exert their effect throughout the entire gland, we injected LatA or CytD, two molecules known to disrupt the actin cytoskeleton. A rat was first systemically injected with TXR-D to label the endosomal and the lysosomal compartments. After 1 h, one gland was injected with LatA or CytD, while the other gland was injected with the vehicle, and 45 min later, 488-D was injected systemically. The glands were excised and imaged after 1 h. CytD (Fig. 14 D and E) was indeed effective in disrupting the F-actincytoskeleton in many areas of the glands as shown by cryosections, while other organs were not affected. Notably, both drugs reduced the internalization of 488-D when compared with control glands, while the levels of TXR-D injected prior to the drugs were not affected (Fig. 14 F, G). How these drugs affected the fluid-phase endocytosis in the gland remains to be investigated, but the results serve as a proof of principle that drugs can be selectively and effectively delivered to the SGs without affecting other organs. Our study has provided new insights into the dynamics of fluid phase and receptor mediated endocytosis in the live animal, which might enable us to better understand the mechanisms of endocytosis in cells in their native environments.

One of the most intriguing finding in our studies on endocytosis was that most of the probes introduced via the blood circulation or via stromal injections were not detected in the epithelium. For example, stromal injection of dextran or other hydrophilic fluorescent conjugates resulted in labeling of the stroma, while the parenchyma remained unlabeled (Fig.15 A). This was generally true for all of the organs tested in mice and rats. If the probe is left for longer period of time it is washed away from the stroma and only the cells that actively endocytosed the probe remain labeled. Presumably, some barrier between the stroma and the epithelium may be preventing the fluorescent probes from accessing the epithelium. A good candidate for such barrier is basement membrane that lines all of the epithelial tissues

in the body. This is supported by the fact that some lipophilic probes such as DiI are able to cross the barrier to be internalized by the epithelial cells (Fig. 15 A). The barrier function is likely to be highly important in organ physiology and some pathological conditions (such as the spread of infectious agents) and with the advent of IVM and physiological models such phenomena can now be studied.

In order to avoid this barrier and study endocytosis in the epithelium, we introduced fluorescent dextrans to the apical side by cannulating the major Wharton's duct and performing infusion by gravity (Fig. 15 B). We were able to label all of the ductal system but still did not see any significant fluid phase uptake under resting conditions (Fig. 15 B, panel 3). We then observed that upon stimulation of protein secretion with isoproterenol (see next sections), the clearing of the ductal system and the simultaneous endocytosis of the fluorescent dextran could be observed. (Fig. 15 B and C). This process is called compensatory endocytosis, and it is stimulated during regulated exocytosis to retrieve the large volumes of new membranes that are delivered to the PM. Compensatory endocytosis is extremely important for the physiology of the glands as the acinar cells have to retrieve the extra membranes contributed by secretion [155]. To our knowledge this is so far the first successful attempt to visualize the compensatory endocytosis dynamically in exocrine glands in live animal.

3. Intravital imaging of exocytosis

3.1 Establishing a model for studying secretory granule dynamics and exocytosis

In SGs, proteins are secreted at the APM primarily through the regulated exocytosis of large SCGs [156]. Due to the lack of appropriate markers for these vesicles there are no good models allowing to observe SCG dynamics in live exocrine tissues or in *ex vivo* preparations. To overcome this issue, we utilized transgenic mice ubiquitously expressing a soluble form of the green fluorescent protein [157]. By using intravital two-photon microscopy, we observed that in the acinar cells of the SGs and the other exocrine glands tested, cytoplasmic GFP was excluded from large vesicles (Fig. 16 and Fig. 17). Based on their size (1-1.5 µm in diameter), behavior (see below), and lack of overlap with markers for other large intracellular organelles such as lysosomes and mitochondria, these vesicles were identified as SCGs (Fig. 16). To better resolve these vesicles, we utilized confocal microscopy, which allows us to control the thickness of the optical slices, providing a higher resolution when compared to two-photon microscopy (Fig. 17) [158]. By performing a z-scan of the SGs, we determined the optimal imaging depth to be approximately between 10 and 15 µm below the surface of the glands (Fig. 17 and Fig. 18). At this depth, the first layers of acini were optically sectioned in the middle (Fig. 18) where both SCGs (Fig.19 a, arrowheads) and acinar canaliculi (Fig. 19 a, arrow) are clearly visible. Indeed, GFP highlighted the APM as identified by the enrichment in cortical F-actin (Fig. 19 b and inset). Although we have not established the reason for this enrichment, we speculated that GFP may bind to some of the components of the actin cytoskeleton in a non-specific fashion. By combining IVM imaging techniques and the use of transgenic animals we have established a powerful model to study regulated exocytosis in exocrine glands.

3.2. Regulation of fusion of secretory granules in the salivary glands of live animals

Since there are conflicting data generated in *in vitro* and *ex vivo* systems about the role of β-adrenergic and muscarinic receptors in SGs, we sought to determine which stimulus elicit exocytosis of the SCGs *in vivo*. Exocytosis was assayed by estimating the reduction in the number of large SCGs after agonist stimulation, as shown by others [55, 146]. To this aim, we injected isoproterenol (Iso, β-adrenergic agonist) and imaged the SCGs by time-lapse confocal microscopy (Fig. 19 c, left panel). Thirty minutes after the injection of Iso we observed an 80% reduction in the number of SCGs and a significant expansion of the acinar canaliculi (Fig. 19 c right panel and insets). The reduction in the number of SCGs was uniformly observed throughout the acini confirming that SCGs underwent exocytosis. Although our experimental set up did not allow imaging directly the fusion step (i.e. the mixing of the membrane bilayer), this assay provided an indirect estimate of the fusion events of the SCGs with the APM. The maximal rate of degranulation was elicited when Iso was injected between 0.1-0.5 mg/Kg (Fig. 19 d) and occurred after 2-5 min from the injection. Higher doses of Iso (>0.5 mg/Kg) induced the rapid formation of large vacuoles (Fig. 20), which most likely represent a non-physiological process [159]. The same response was also observed in the parotid glands and in the SGs of live rats, and neither the externalization of the glands nor the GFP expression had any effect on the regulation or the rate of degranulation (Fig. 20). Injections of Carb, even at doses comparable to those utilized in *ex vivo* explants, did not stimulate any degranulation in contrast to previously reported data (Fig. 19 d and Fig. 20) [52, 53, 55, 160, 161]. However, Carb showed a biological activity since it induced fluid secretion as expected (Fig. 21). Lastly, co-injection of Iso and Carb did not result in any significant increase in the rate of degranulation (Fig. 19 e, Fig. 21).

3.3. After fusion with the apical plasma membrane the secretory granules collapse in a single step.

Next, we imaged the dynamics of the SCGs at the apical plasma membrane (APM). The scanning speed was increased to 0.2-0.6 s per frame to visualize the large SCGs, which undergo exocytosis in a slow fashion (several seconds up to minutes) [23, 27]. Upon injection of Iso, most of the cytoplasmic SCGs increased their motility, whereas those closer to the APM did not. This subpopulation of SCGs exhibited a 2-3 fold increase in the GFP fluorescence surrounding them, which correlated with the recruitment of F-actin (Fig. 22 a). Notably, these SCGs decreased in size slowly (40-60 sec) and gradually collapsed into the APM (Fig. 22 b, arrow and 22 c), suggesting that exocytosis of SCGs was imaged. This idea is further supported by the fact that these events were observed only when degranulation was stimulated by Iso. Previous studies in acinar preparations of explanted exocrine glands showed that this process occurs through compound exocytosis rather than single fusion events [23, 55, 162]. Compound exocytosis has been defined as the process by which large SCGs fuse with SCGs that are already connected with the APM, generating strings of 3-4 interconnected granules [25]. These strings, which have been reported to be stable for more than 20 sec, should have been detectable under the imaging conditions used in this study [36, 51]. However, we cannot exclude that due to the thin optical slices utilized to image the SCGs in the GFP mice, some of the interconnections between the fusing SCGs might have been missed. To clarify this, we used two alternative approaches. First, we slowly infused a fluorescently-labeled dextran into the ductal system of a live rat (Fig. 22 d) [147]. This approach mimics the bathing of the explanted glands in small fluorescent probes that has been used to investigate exocytosis in *ex vivo* models [25, 36, 39, 55, 163, 164]. For this set of experiments, we used larger optical sections (1-1.2 µm, Fig. 17) closely matching those

achieved by two-photon microscopy experiments that have been successfully utilized to image compound exocytosis [38]. Upon injection of Iso, the dye rapidly filled large vesicular structures, which later gradually collapsed with the APM (Fig. 22 e and f). Based on their size (1-1.5 µm in diameter) we argued that these structures represent SCGs, which have fused with the APM and have been filled with fluorescent dextran upon the opening of the fusion pore. This was confirmed by performing the same experiment in the mouse expressing soluble GFP, where the SCGs are visible (data not shown). Under these conditions, we did not observe any evidence of compound exocytosis. Second, we used a transgenic mouse ubiquitously expressing a membrane-targeted peptide fused with the fluorescent protein tdTomato (m-Tomato mice) [165]. This reporter localized both at the apical and the basolateral PM but not in the SCGs (Fig. 22 g). The apical canaliculi were easily identified based on their characteristic F-actin coat and morphology (Fig. 22 g-i). In this model, we expected the m-Tomato to diffuse into the SCGs upon fusion with the APM thus enabling us to track their fate. Also in this case, the optical section was increased to 1-1.2 µm to optimize the detection of the SCGs and the APM (Fig. 17). After injection of Iso, m-Tomato localized onto large circular structures (1-1.5 µm in diameter) and the acinar canaliculi appeared enlarged as shown for the GFP mice (Fig 22 h). Time-lapse imaging showed that upon injection of Iso the m-Tomato circular profiles completely collapsed at a rate similar to that observed for the SCGs in the GFP mice (40-60 sec) (Fig. 22 j). Fusing SCGs clustered around the expanded canaliculi but compound exocytosis was not observed (Fig. 22 j). These vesicles represented the fused SCGs as shown by crossing the m-Tomato mice with the GFP mice (Fig. 23).

Overall, our data support the idea that large SCGs in the SGs *in vivo* fuse at the PM and release their contents in the extracellular space in a single event, which leads to the controlled collapse of the granules into the APM. Although we have not observed any compound exocytosis of large SCGs, due to the spatial and temporal limitations of our experimental system we cannot rule out that smaller vesicular structures (between 50 and 100 nm) fuse with the SCGs during the collapse.

Based on this data we conclude that the β-adrenergic and not the muscarinic receptors elicit the fusion of the SCGs with the APM and that this process occurs in SGs *in vivo* through single fusion events and not through compound exocytosis [23, 55]. The reason(s) for the discrepancy between the data derived from explanted organs or acinar preparations and the animal model are difficult to determine. One possible explanation is that the damages derived from the mechanical or enzymatic procedures used to prepare the tissues may activate or alter various signaling pathways, favoring the docking of the granules at the APM and their sensitivity to Ca++ signaling, as shown for lysosomal secretion during membrane repair [166]. Moreover, these procedures may disrupt the actin cytoskeleton resulting in the fusion between the granules at the APM, reminiscent of compound exocytosis [55].

4. Role of the actomyosin complex during the exocytosis of large secretory granules

4.1. F-Actin is recruited on the secretory granules after membrane fusion with the apical plasma membrane and is required to drive their collapse to completion

We observed that the size of the SCGs did not change for the first 5-10 sec after fusion with the APM (Fig. 22c, f and k, red circles). During this time the m-Tomato diffused into the SCGs with what appeared to be a slow rate. Interestingly, the fusion pore opened in parallel with the diffusion of the m-Tomato, as shown by infusing fluorescently-labeled dextran into the ductal system of the m-Tomato mouse and stimulating exocytosis with Iso (Fig. 24). After the intensity of the m-Tomato fluorescence reached a maximum the granules sharply decreased in size (Fig. 22 k, black circles). We hypothesized that this lag time was due to the recruitment of the machinery regulating the collapse of the granules. Since F-actin coated the granules close to the APM (Fig. 22 a), we investigated whether it could play a role in facilitating this step. To this aim, we labeled the SGs of the m-Tomato mice for F-actin after stimulation with Iso. We observed that 100% of the F-actin-coated granules (481 granules scored, N=3) were labeled with the m-Tomato, whereas 2.8 ± 1.8 % (average ± S.E.M, N=3) of the m-Tomato-labeled granules were not labeled with F-actin (Fig. 25 a, arrows). This finding suggested that F-actin was recruited onto the SCGs only after membrane fusion has occurred. Next, we analyzed the dynamics of F-actin recruitment onto the SCGs by transfecting the acini of live rats with GFP-lifeact, a probe that dynamically labels F-actin without compromising its function [167]. We have previously shown that the acini in the SGs can be selectively transfected with fluorescently-tagged proteins (Fig. 25) [147]. As expected, in acinar cells, GFP-lifeact showed a distribution comparable to that of F-actin. In control conditions GFP-lifeact was localized at the PM and enriched at the apical pole (Fig. 25 d, arrowhead). Upon stimulation with Iso, GFP-lifeact was recruited onto the

SCGs and then progressively released during their collapse (Fig. 25 d and e, arrows). To analyze the kinetics of F-actin recruitment with respect to the dynamics of the SCGs, we co-transfected Red Fluorescent Protein-lifeact (RFP-lifeact) with GFP-Farnesyl, a marker for the PM [168] that behaves similarly to the m-Tomato both in resting conditions (Fig. 25 f, arrow) and under stimulation (Fig. 25 f, arrowheads). F-actin was recruited onto the SCGs after a short lag time coinciding with the initial diffusion of membranes from the canaliculi, suggesting that some of the factors controlling the nucleation or the assembly of F-actin might come from the APM (Fig. 25 g, and h). This finding also suggests that F-actin assembly occurs after the opening of the fusion pore and most likely does not play any role in this process. Finally, we pharmacologically disrupted the actin cytoskeleton in live animals by using cytochalasin D (CytD, Fig. 27) or latrunculin A (LatA, Fig. 26). In resting conditions no exocytic events were observed, although some small vesicular structures of unknown origin were observed in close proximity to the PM. Upon injection of Iso, SCGs fused with the APM with the same rate described above, but failed to collapse (Fig. 27 a, arrows and b) and increased in size, forming large vacuoles 2-3 fold larger than the normal granules, as shown by measuring their diameter over time (Fig. 27 c, red circles). These vacuoles were generated by the SCGs fusing with the APM, and not as a result of interfering with endocytic events, as shown by disrupting the actin cytoskeleton in GFP-mice (Fig. 26). Furthermore, we observed that the remaining SCGs fused and rapidly collapsed with the vacuoles in a process reminiscent of compound exocytosis (Fig. 27 d). LatA treatment produced similar results (Fig. 26). These observations suggest that F-actin may play a role in controlling the collapse of the granules and in preventing their homotypic fusion that was not observed under control conditions. Moreover, F-actin may provide a scaffold preventing the

expansion of the SCGs that may be driven by the hydrostatic pressure generated by the fluid secretion that we observed during the exocytic process (Fig. 28).

Finally, we observed that 5-10 min after stimulation with Iso the total amount of secreted protein was inhibited by almost 50% (Fig. 26 d). Since we ruled out that the impairment of the actin cytoskeleton affected the opening of the fusion pore (Fig. 26 e), this inhibition may be explained by the fact that the failure of the first SCGs to collapse prevented the discharge of the cargo proteins into the canaliculi. However, after 30 min, all the SCGs completely fused with the large vacuoles (Fig. 26 c) and the level of the secreted protein was comparable to that measured in control conditions. This suggests that the cargo proteins retained in the vacuoles were released into the canaliculi, possibly facilitated by fluid secretion accompanying exocytosis.

Taken together, these data suggest that F-actin serves many functions during stimulated secretion in the SGs. First, we have shown that F-actin provides a scaffold counteracting hydrostatic imbalances that might interfere with the dynamics of the granules. This role is most likely restricted to the exocrine glands where regulated exocytosis at the APM is accompanied by fluid secretion. Notably, such a role for F-actin has not been described in *ex vivo* systems where the hydrostatic pressure does not build-up due to the lack of an intact ductal system. Second, we have shown that F-actin prevents the fusion between the SCGs accumulated in the apical area and those fused with the APM. In secretory systems in which the collapse of the SCGs is a slow process, the fused granules may have acquired components of the APM, which makes them more susceptible to fusion with other SCGs [169]. In order to prevent these fusion events, F-actin could be recruited onto the SCGs performing a “barrier” function similar to what has been proposed for the F-actin at the APM

[34, 170]. Finally, we have shown that F-actin is required to drive the collapse of the SCGs to the APM. Our data suggests that F-actin may serve as a platform to recruit molecules generating the force required for the collapse of the granule). The impairment of the assembly of F-actin around the fused SCGs leads to a substantial increase in their size and a complete block of their collapse.

4.2. Myosin IIa and IIb are recruited onto the granules and their motor activity facilitates the collapse of the secretory granules

We reasoned that the role of F-actin in facilitating the collapse of the SCGs may be linked to the assembly of an acto-myosin complex, as described for the contractile ring during cytokinesis [171, 172]. Indeed, nonmuscle myosin IIa has been previously implicated in the regulation of the opening and the closing of the fusion pore during regulated secretion [38, 39, 173]. We determined that in resting conditions, both myosin IIa and IIb localized in the cytoplasm and at the APM in the SGs (Fig. 29 a and c), whereas upon stimulation with Iso, both isoforms were recruited onto the surface of the fusing granules (Fig. 29 b and d, arrowheads). To determine whether these myosins were involved in SCGs exocytosis, we pharmacologically blocked their motor activity by using (-)blebbistatin (Bleb), a specific inhibitor of the myosin II ATPase [37]. In animals treated with (-)Bleb, we observed the appearance of few intracellular vesicles of unknown origin and the enlargement of the acinar canaliculi (Fig. 29 e, arrows). Upon stimulation with Iso, although the onset of the fusion events was not affected, the acinar canaliculi further expanded and granules of larger size appeared at the APM (Fig. 29 e, arrowheads). Time-lapse sequences showed that a significant proportion of SCGs fused with the APM and abruptly increased in size, as observed when the actin cytoskeleton was disrupted (Fig. 29 g and i). However, under these conditions, SCGs collapsed with the APM and only a small population collapsed at a slower

rate when compared with the inactive stereoisomer (+)Bleb (Fig. 29 h and i). These data suggest that myosin IIa and IIb are part of the machinery that regulates the collapse of the granules after fusion with the APM but whether myosin II is absolutely required for granule collapse is still unclear.

We have shown that the inhibition of the motor activity of myosin II results in a sharp increase in the size of all the fused SCGs and in the delay of the kinetics of the collapse but only in a small sub-population of the SCGs. The fact that (-)Bleb did not completely block the collapse of the granules might be due to a partial inhibition of the myosin activity and unfortunately, higher concentrations of (-)Bleb could not be used since they induce non-specific effects on the cell membranes. Two other possibilities are that either other molecules are involved in this process (e.g. another myosin), or that when myosin II activity is impaired the collapse of the SCGs is regulated by a different mechanism. Moreover, since (-)Bleb inhibits the activity of both myosin IIa and IIb we could not assess whether they perform different functions during SCGs exocytosis in SGs as described in other systems [38, 39, 174]. To address these issues, studies employing mice harboring conditional knockout alleles of myosin IIa and IIb are underway.

4.3. F-actin and Myosin II recruitment and their dynamics during regulated exocytosis.

An important question is how the fusing granule recruits the actomyosin complex to its surface. Is the adrenergic signaling cascade required for the acto-myosin recruitment and if so, which molecules are involved? Alternatively, is membrane fusion and the mixing of the two membranous compartments sufficient to initiate the recruitment? Another interesting question is whether actin and myosin are dependant on each other for their recruitment and function. In order to start to address these questions we used transgenic mice expressing

GFP-myosin IIa and IIb [144]. Using these mice we have been able to image the dynamics of myosin IIa and IIb, which in resting conditions are localized at the APM and in the cytoplasm whereas upon stimulation are both recruited onto the granules (Fig. 30 A and B). Both myosin II isoforms are recruited from the cytoplasm and not by diffusion from the APM, as shown by the kymographs in Fig. 30A and B. Moreover, we had crossed these mice with those expressing RFP-Lifeact enabling us to simultaneously visualize F-actin and myosin II (Fig. 30 C). Notably, we observed that during exocytosis myosin IIb is recruited on the granules 6-8 seconds after the initiation of actin polymerization at the granule membrane (Fig 30 D). By plotting the fluorescence profiles we also found that myosin IIb is retained on the granules after F-actin disassembly (Fig 30 E). Such observations suggested that the in actin may play a role in the initial phase of myosin II recruitment onto the membranes and that later some other molecule may be involved maintaining it at the PM. Similar results were obtained for myosin IIa. Ongoing studies are aimed at pharmacologically perturbing one or the other molecule of the complex and observing the changes in dynamics of the partner molecule.

5. Model of regulated secretion in salivary glands

To summarize, in our studies of regulated exocytosis in SGs we focused on the dynamics of the process and the machinery regulating the fate of the SCGs after their fusion with the APM. We used a combination of transgenic mice and gene transfection into the SGs of live rats, which enabled us to visualize the SCGs, their limiting membranes, their content, actin cytoskeleton and myosin motor proteins. Specifically, we showed that exocytosis of the SCGs in the SGs *in vivo* is elicited exclusively by the β-adrenergic receptor and not the

muscarinic receptor. Furthermore, we determined that after fusion with the APM, SCGs completely collapse without any evidence of compound exocytosis. Finally, upon fusion with the APM, F-actin and nonmuscle myosin II are recruited onto the surface of the SCGs, where they provide a scaffold that facilitates the collapse with the APM and prevents the homotypic fusion of the SCGs [175]. By taking advantage of IVM and a physiological model system were able to shed some light in these controversial topics in the field of regulated exocytosis. The discrepancy between our data and those acquired using *ex vivo* systems may warrant some further discussion on models of regulated exocytosis and possible factors that might have been overlooked.

First, it may be useful to review the basic structure of the acinus, which produces the complex morphology of the apical pole, where secretion takes place. Acini are formed by 9-10 polarized acinar cells, which are tightly packed into a sphere-like unit (Fig. 31). The apical domains of the PM of two adjacent cells form narrow canaliculi with a diameter of 0.2-0.3 µm and a length of 10-15 µm. Each cell shares 2-3 canaliculi with adjacent cells, and they are all interconnected, ultimately merging into a larger duct at the base of the acinus, called the intercalated duct. A single acinar cell contains 250-300 SCGs, which have a diameter of 1-1.5 µm. One of the most striking outcomes of this arrangement is the difference in membrane tension between the APM and SCGs, which is a function of their diameter. When two of such membranous compartments fuse there is a flow of membranes toward the area with the lowest membrane tension [30, 176]. Based on geometrical consideration, large SCGs should have a lower membrane tension than narrow canaliculi, and indeed we observed that after the opening of the fusion pore, membranes flow from the canaliculi into the SCGs (Fig 32). This suggests that the collapse of the SCGs into the PM

may not be an energetically favorable process. We propose that the actomyosin complex is recruited onto the surface of the SCGs to form a contractile scaffold, which provides the energy to complete this step (Fig. 32). Although we do not know whether the force generated by the scaffold acts by pushing the membranes or by enlarging the fusion pore, we suggest that the actomyosin complex is required to reduce the size of the SCGs, thus increasing their membrane tension to a point in which the collapse becomes more energetically favorable.

Two interesting observations further support this model. First, in the absence of a functional actin cytoskeleton the SCGs are able to collapse into the large vacuoles (Fig 27 D). Under this condition, SCGs (diameter 1-1.5 µm) have a higher membrane tension than the large vacuoles (4-5 µm) and their collapse may be more favorable (Fig. 33 C). Second, we noted that when the activity of the myosin II motor is impaired, the acinar canaliculi are significantly expanded (diameter 1.8-2.0 µm) (Fig. 29 E and G). Under this condition, SCGs may have a higher membrane tension than the expanded canaliculi and the process could possibly be brought to completion without the need for a contractile activity (Fig. 33 A). Multiple reports from *ex vivo* models have reported actin coat on the granules, however they did not find F-actin or myosin to be required for controlling the collapse. It is possible that some disturbances during acinar preparations may alter the delicate geometry of apical domains of the cells.

Another aspect that emerged for our *in vivo* study comes from the finding that when the dynamics of the actin cytoskeleton was disrupted by pharmacological agents such as cytochalasin D or latrunculin A, SCGs expanded in size and their gradual collapse was impaired. The analysis of the diameters of the SCGs showed that there is a linear increase in their size in the first 20-30 seconds after the opening of the fusion pore. Since during this

period we did not detect any large membranous vesicle fusing with the SCGs, we speculated that the expansion was driven by the flow of membranes from the APM into the granule via the fusion pore. In addition to the membrane tension factor, hydrostatic pressure may contribute to this process (Fig 28). After this initial step, the increase in size of the enlarged SCGs is due to membranes delivered by other SCGs that fuse with the enlarged SCGs that have acquired the characteristics of the APM (Fig. 27 D). Similarly, when the activity of myosin II was impaired with blebbistatin, SCGs initially expanded in size, and later resumed their gradual collapse. This suggests that the myosin II contractile activity is also required to counteract the hydrostatic pressure after the opening of the fusion pore. Under this condition, the expanded granules did not further increase in size since the fusion with the other SCGs was prevented by the actin coat that assembled around the expanded granules.

Overall our data suggests that another function of the actomyosin complex on the surface of the fusing granules is to counteract the effect of the hydrostatic pressure. This implies that fused SCGs represent a weak spot at the APM that needs to be “patched” to prevent disruptions in the cell architecture. This hypothesis was also supported by the fact that an artificial increase of the intraductal pressure during exocytosis induced the expansion of the SCGs even when the actin cytoskeleton was not perturbed.

CONCLUSIONS

In the past two decades the development of fluorescent protein technology and live cell microscopy resulted in an explosion of information on every cellular process imaginable. These developments have advanced our understanding of cell biology tremendously. Most of this knowledge was acquired by employing cell culture models which are extremely powerful when it comes to experimental manipulations, however, they may not provide a true representation of the actual biology of complex multicellular organisms. Over the years there has been tremendous progresses in developing experimental models that can produce dynamic and mechanistic information in multicellular organisms, most notably in *C. elegans*, *D. melongaster* and *D. rerio*. More recently, IVM techniques, and nonlinear microscopy in particular, have expanded *in vivo* studies into mammalian models. Although IVM has addressed key biological questions in fields such as neurobiology, immunology and tumor biology, most of the work has been focused at the tissue and single cell level [149]. The possibility to expand our knowledge of cell biology in mammalian models under true physiological conditions, is very exciting and justifies the efforts to advance the current IVM techniques towards achieving subcellular resolution. Moreover, approaches based on pharmacological and genetic manipulations have to be developed in order to start probing the function of various machineries in cell biology.

With this in mind, we set out to establish a model system for studying endocytosis end exocytosis in the salivary glands of live rats and mice. The SGs are readily accessible with a minor surgery and can be externalized and stabilized for intravital imaging in relatively easy fashion. Development of surgical and stabilization techniques such as

customized SG holders was crucial in our achievement of imaging sub cellular structures in live animals. Using this system we were able to image internalization and trafficking of various fluorescent molecules in the stromal and acinar cells of SGs *in vivo*. We found that fluid phase markers that diffuse from the blood vessels are rapidly internalized into early endosomes of fibroblasts within 2–3 min from the injection. The early endosomes undergo homotypic fusion in the periphery of the cells and after 30–40 min reach late endosomal/lysosomal structures in the perinuclear area [148]. The kinetics of transferrin internalization was markedly slower than that of fluid phase markers and they were all trafficked into the lysosomes. Notably, the same cells explanted and grown on glass employed the canonical pathways where transferrin undergoes rapid internalization and recycling while avoiding the lysosomal degradation. Next, we developed pharmacological and genetic manipulations that allowed us to ask questions about the machinery involved in the process of interest. For example, we showed that perturbing actin cytoskeleton partially inhibits the fluid phase endocytosis in stromal cells *in vivo* [148].

We then extended IVM to study both the regulation and modality of regulated exocytosis in SGs *in vivo* and began to dissect some of the molecular components involved in this process. We focused our initial efforts on unraveling the role of the actin cytoskeleton in exocytosis of SCGs, as no clear picture of its function in regulated secretion has emerged up to this point. To address these questions, we used a combination of different approaches such as: 1) transgenic mouse models, 2) the ability to transfect genes into the acinar cells, and 3) the ability to selectively deliver fluorescent probes and pharmacological agents into the SGs. The use of mice expressing cytoplasmic GFP and/or membrane-localized tomato fluorescent protein has enabled imaging the kinetics of SCGs exocytosis and to confirm that *in vivo* this

process is triggered exclusively by beta-adrenergic stimulation. Next, by using three independent experimental approaches we observed that *in vivo,* SCGs fuse with the PM and gradually collapse after the opening of the fusion pore without any evidence of compound exocytosis. Lastly, we found that actin and nonmuscle myosin II assemble on the granules after fusion and are important in driving the complete collapse of the SCGs. Our data suggests that a functional contractile actomyosin complex assembles onto the SCGs during exocytosis to perform at least three functions: 1) to counteract the effect of the hydrostatic pressure an energetically unfavorable membrane tension difference, 2) to prevent the homotypic fusion of the granules that are fused with the APM and 3) to facilitate the gradual collapse of the secretory granules [31, 175, 177].

Our approach to studying cell biology based on IVM in live rodents has highlighted that some biological processes occur with the coordination of several cellular events and are strongly influenced by the architecture of the experimental model. Reductionist approaches based on the use of simplified models offer the advantages of a better control of the experimental conditions and the opportunity to study processes at a molecular level. However, certain aspects of the physiology of an organ, that may have unanticipated effects on cellular functions cannot be recapitulated *in vitro* systems and require the use of *in vivo* models. The same approaches and tools developed for the SGs can be easily applied to other organs and target new problems in cell biology. Furthermore, novel tools are now available to address additional questions using IVM. Among them are mice expressing various fluorescently tagged markers and machinery, huge libraries of knockout and conditional knockout animals and relatively novel procedures to perform protein ablation *in vivo* via siRNA or shRNA. IVM has a huge potential to uncover several not yet understood cellular

processes during physiological and pathological conditions. In our view, this approach is going to be one of the main tools to study cell biology in the future and we were fortunate to have contributed in advancing this field a step further.

FIGURES

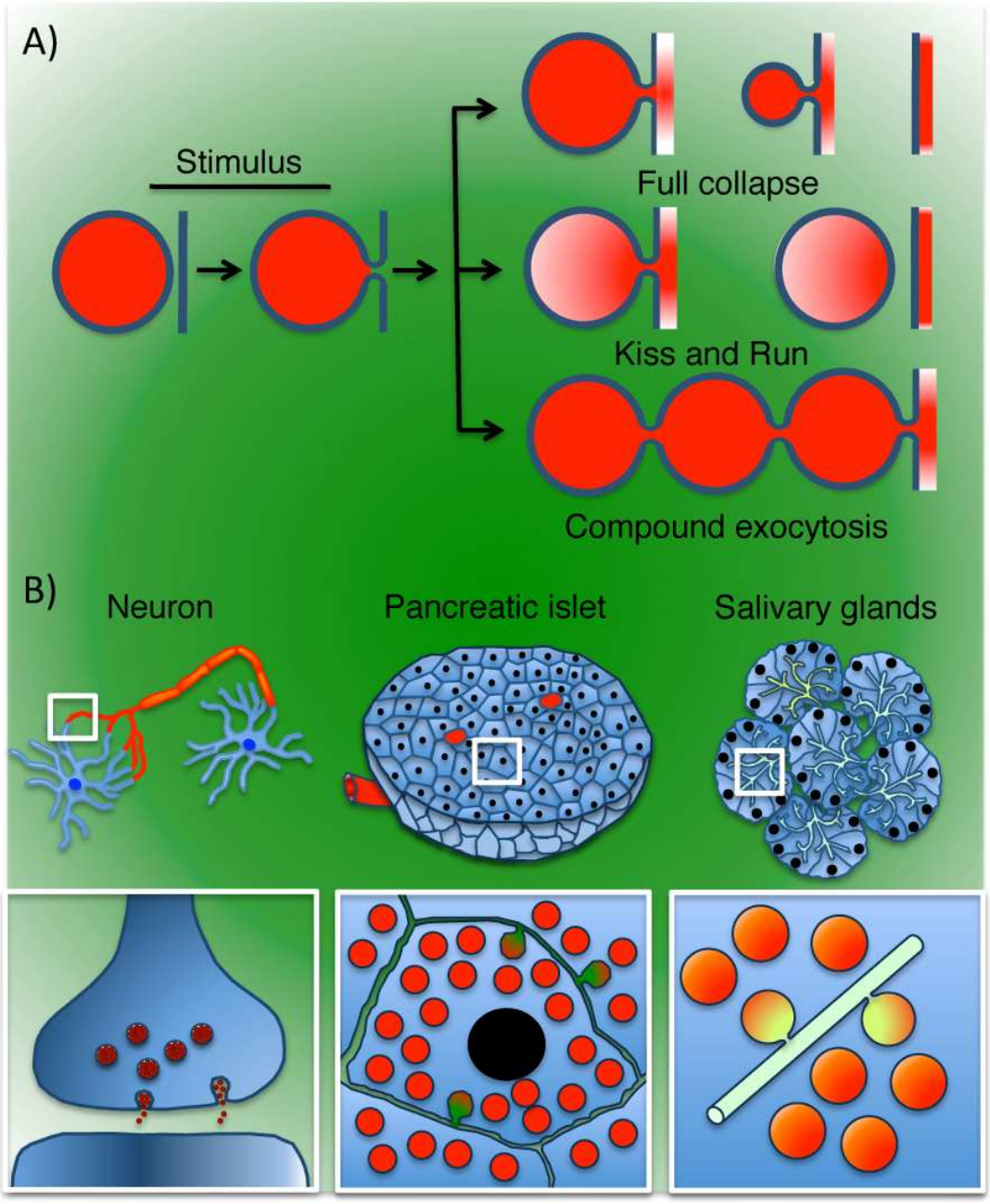

Figure 1. Regulated exocytosis. A – Modality of regulated exocytosis. Upon stimulation, exocytic vesicles fuse with the PM and the fusion pore opens. Exocytic vesicles can undergo: 1) full collapse, 2) kiss and run, or 3) compound exocytosis. B - Different architecture of the secretory organs. In neurons, small synaptic vesicles release their content at the pre-synaptic terminals into the synaptic cleft (left). In endocrine glands, such as the pancreatic islets, molecules are released in the extracellular space and reach the bloodstream (center). In exocrine glands, such as the salivary glands, cargo molecules are released into a series of canaliculi and ducts that are connected to the oral cavity (right)

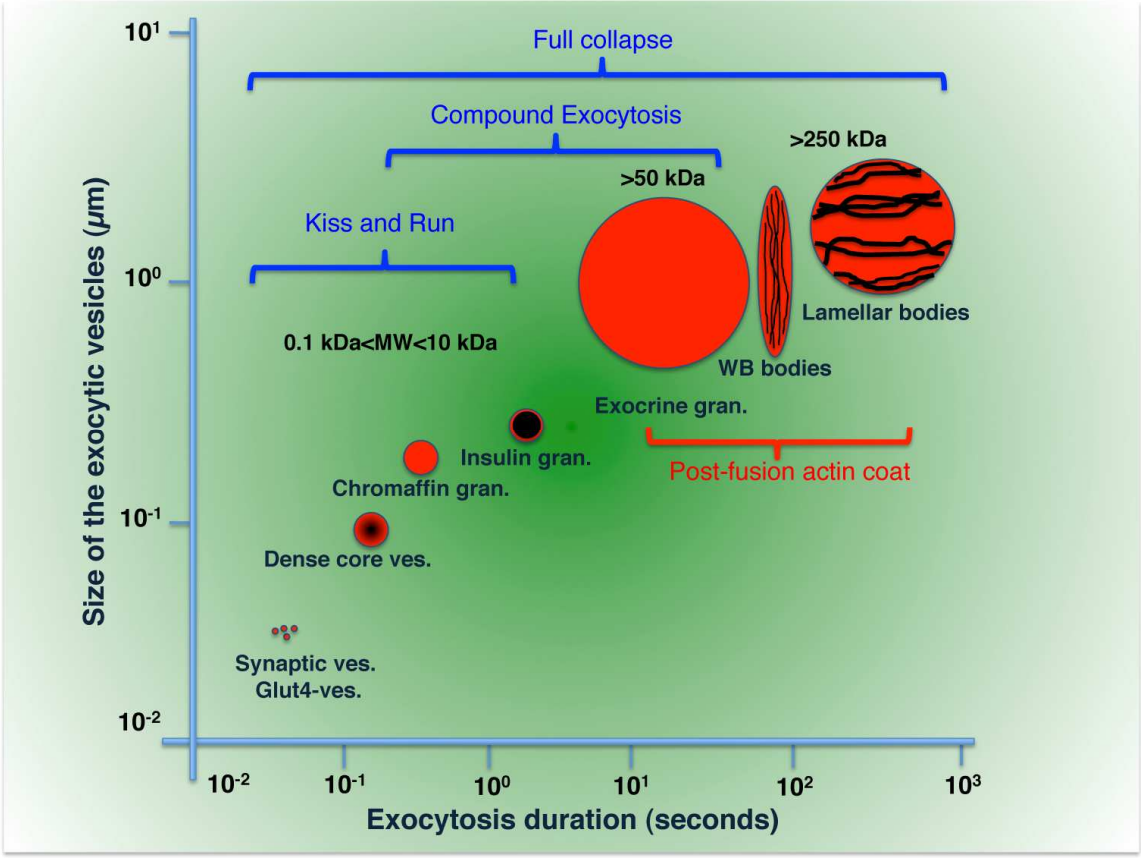

Figure 2. Morphology of the exocytic vesicles. Exocytic vesicles have different size ranging from 50 nm for the small synaptic vesicles up to 2-3 µm for the lamellar bodies. The nature of the cargo molecules varies from small neuropeptides to aggregates of different sizes, such as the VWF and insulin. The duration of the exocytic events ranges from few milliseconds, for the smaller vesicles, up to minutes, for granules containing large aggregates. The increase in diameter and size of the cargo molecules inversely correlates with the duration of exocytosis. Notably, kiss and run events seems to occur primarily in smaller vesicles transporting lower molecular weight cargoes, and actin primarily coats larger vesicles that have a slower kinetics of exocytosis and transport larger cargo molecules.

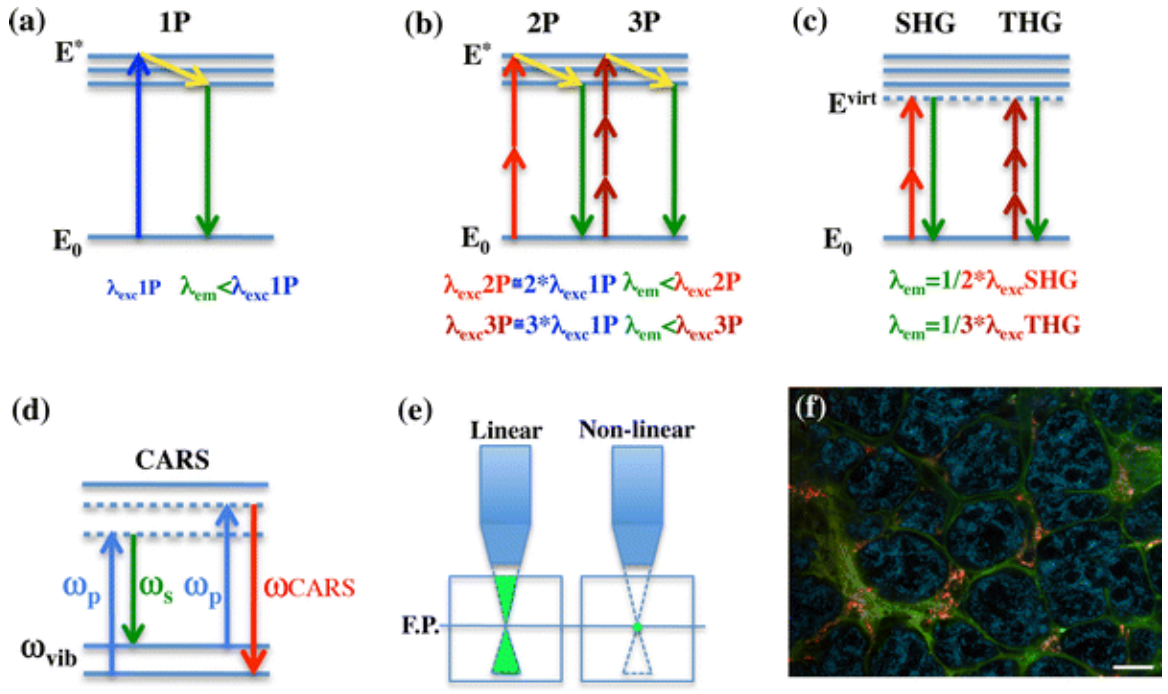

Figure 3. Non-linear optical microscopy. a–d Jablonski diagram illustrating a single photon (1P), b two-photon (2P) and three-photon (3P) excitation, c second (SHG) and third (THG) harmonic generation, and d Coherent anti-Stokes Raman spectroscopy (CARS). a, b In both single and MP microscopy, the emitted photons have a lower energy than the sum of the incident ones, due to some energy loss (yellow arrow). c In SHG and THG the incident photons are scattered and recombine in a single one, without energy loss. d In CARS microscopy two beams are used: the pump (ω p) and the stokes (ω s). When they are tuned to match a vibrational energy gap (ωvib), a strong anti-Stokes signal is generated (ω CARS). Note that both in the harmonic emission and in CARS no electronic transitions occur. e Non-linear emission occurs at the focal spot. f Multiple fluorophores can be imaged using a single excitation wavelength. Alexa 488-dextran transferrin (green) and Texas-red–dextran (red) were injected in the submandibular glands of male rats and internalized into endosomal vesicles by fibroblast located in the stroma. After 1 h, the glands were imaged by MPM using 750 nm as excitation wavelength. The endogenous fluorescence highlights the acinar structures (cyan). Note that both transferrin and dextran bind to the extracellular matrix surrounding the acini. Scale bar 20 μm

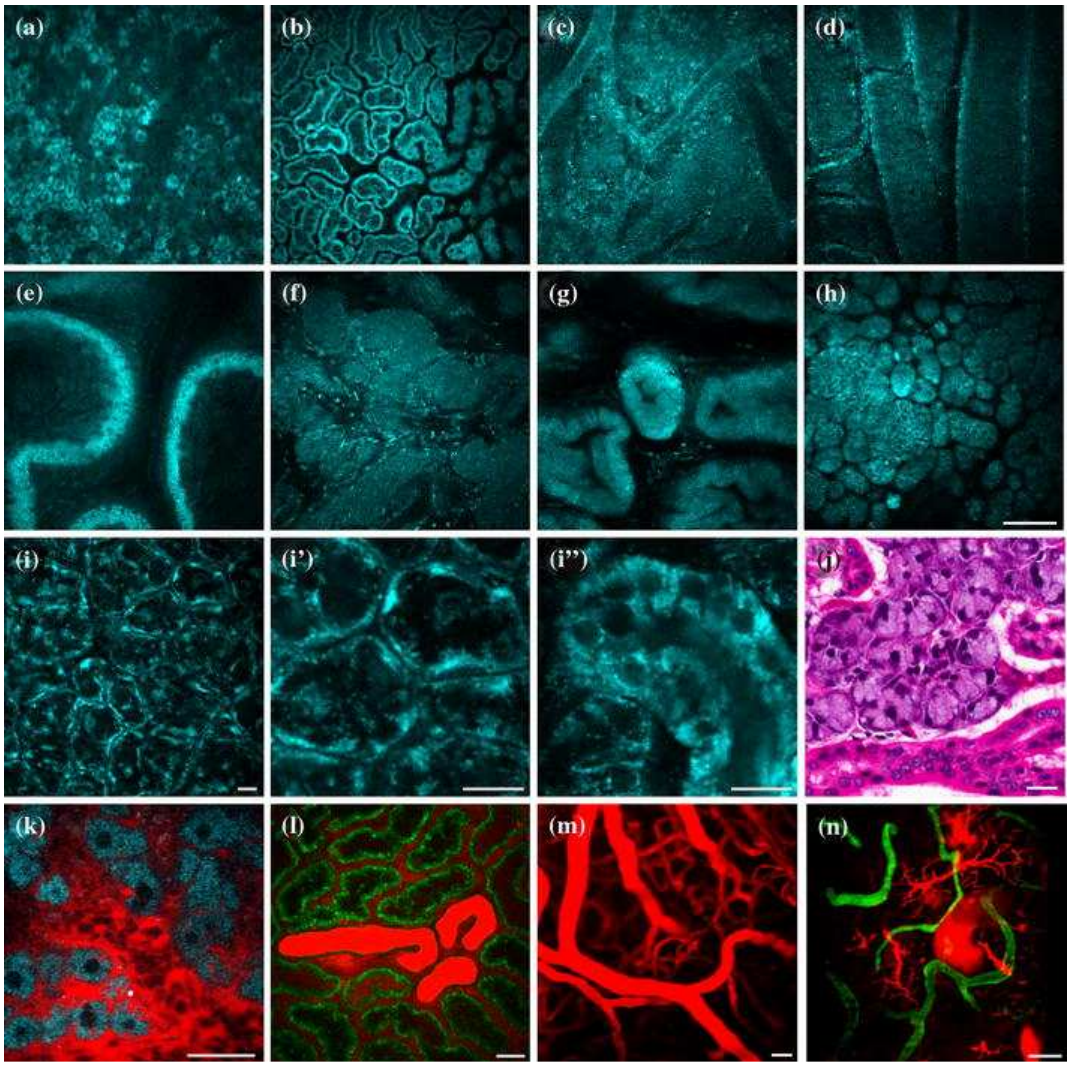

Figure 4. Imaging the architecture of the tissues in live animals. a–i Excitation of intrinsic fluorescence to image tissue architecture. Rats were anesthetized and various organs such as liver (a), kidney (b), brain cortex (c), skeletal muscle (d), epididymis (f), bladder (g), prostate (h) and lacrimal glands (i) were imaged at a low magnification using 740 nm as excitation wavelength. Scale bar 100 μm. The submandibular glands were imaged at a higher magnification (i) and details of the structure the acini (i′) and the large striated ducts (i″) are compared with the classical H&E staining (j). Scale bars 10 μm. k–m Imaging the vasculature in live animal. Texas-red dextran was systemically injected in anesthetized rats and the liver (k), the kidney (l) and the brain cortex (m) were imaged using 740 nm (k, l) or 920 nm (m) as excitation wavelength. n Vasculature and salivary ducts in live animals. FITC-dextran was injected systemically in anesthetized rats, whereas Texas-red dextran was injected into the Wharton's duct as described in Sramkova et al. (2009). The salivary glands were imaged by MPM using 920 nm as excitation wavelength. Scale bars 20 μm

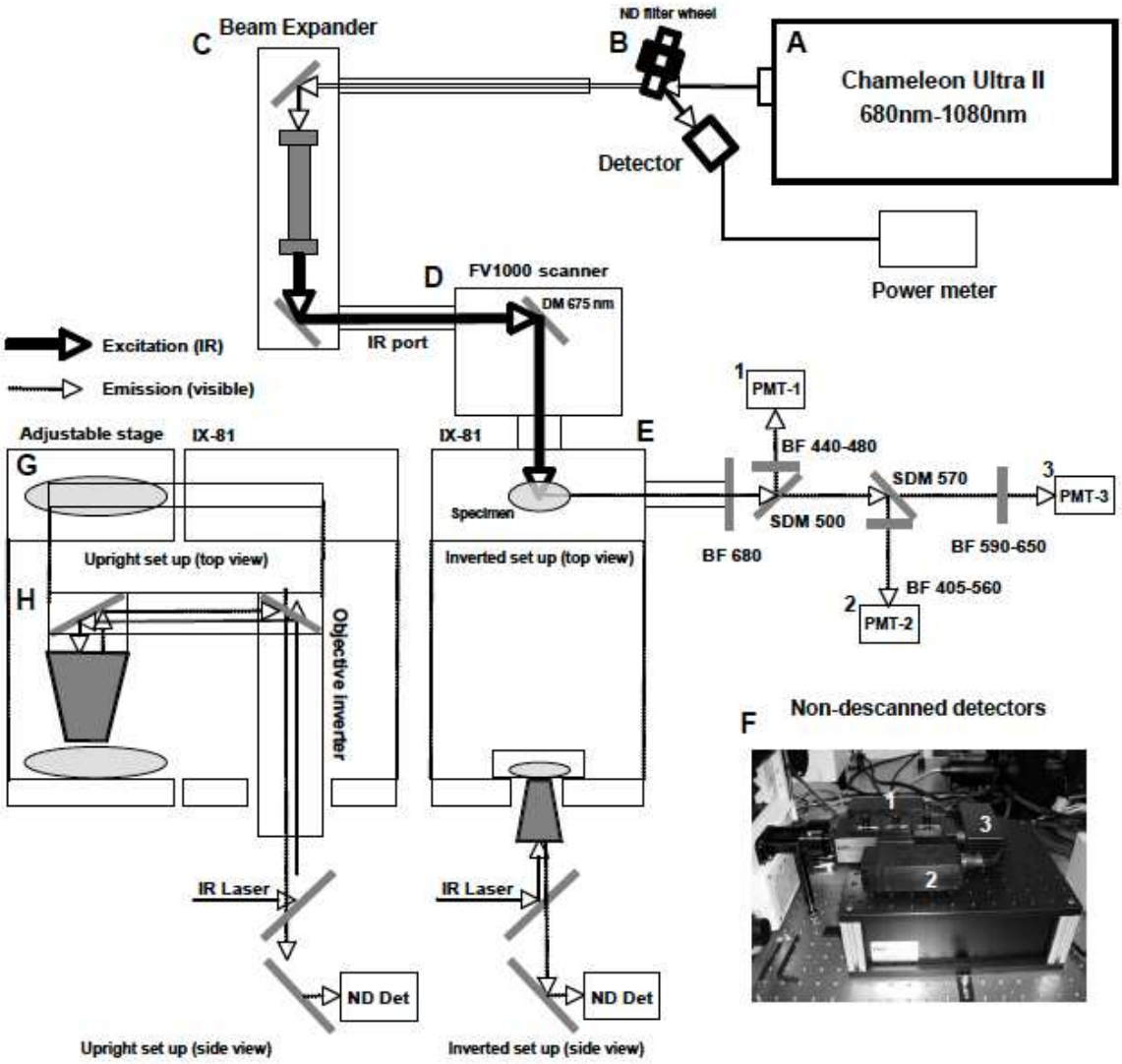

Figure 5. Multiphoton Microscope set up. The laser beam generated by a tunable Ti:Sapphire femtosecond laser (A) is directed through a rotating wheel holding a series of ND filters. The reflected light is collected on a detector (B) connected to a power meter. The size of the beam is modulated using a beam expander (C) and from there, the beam is directed first into the Fluoview 1000 scanning head (D) and then to the microscope (E). The specimens can be imaged using two different configurations. In the inverted configuration the specimen (typically excised tissue) is located on the stage of the microscope while in the upright configuration the specimen (typically the live animal) is located on the adjustable stage (G) adjacent to he microscope. In this configuration the objective is mounted on an objective inverter (H). The emitted signal is directed into a custom-made arrays of three non-descanned detectors that were installed on the right port of the microscope (F). A 680 nm barrier filter is used to prevent the scattered IR light to reach the detectors. The three PMTs (1,2,3), two the dichroics and the 3 barrier filters are arranged as shown above.

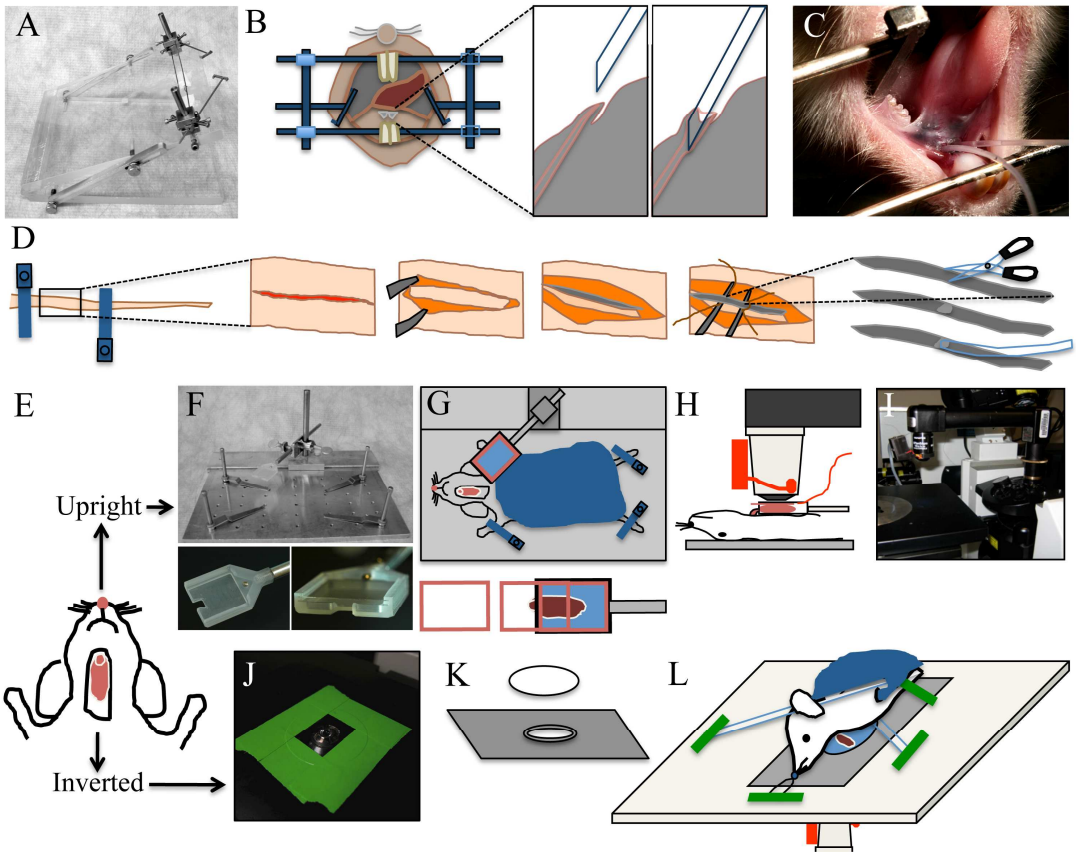

Figure 6. Animal preparation for intravital microscopy. A-C - Cannulation of the Wharton's duct. A - Custom made stereotactic device for cannulation. B - Diagram showing the Wharton's duct cannulation procedure. C - Picture of an anesthetized rat, immobilized on the stereotactic device. Two PE-5 cannulae were inserted in the ducts. D - Diagram of tail artery catheterization procedure. The tail artery is isolated, an incision is made and PE-5 tubing is inserted. E - Diagram showing the rat after SGs externalization surgery. The animal can be positioned for imaging either for upright or inverted configuration. F-I - Setup for the upright configuration. F - Custom made animal stabilization stage with salivary gland holder. Lower panels show the details of SG holder. G - diagram showing the positioning of the animal for the upright configuration. Lowe panel shows the insertion of the coverglass. H - Diagram showing the animal in a side view on the stage. The objective equipped with a heater is brought on top of the coverslip covering the SG. I - Picture showing the microscope in the upright configuration. Objective and heater are mounted on to an objective inverter. J-L - Setup for the inverted configuration. J - A round 40 mm cover slip secured to a 35 mm inverted dish holder stage insert is pictured. Plan-Apo 60x water-immersion objective is visible. K - Diagram showing the 35 mm dish holder stage insert and a coverslip. L - Diagram showing the positioning of the animal for the inverted configuration. The animal is stabilized by a suture holding the incisors and several bars holding down the neck and the thorax areas. These stabilization devices are held in place by masking tape.

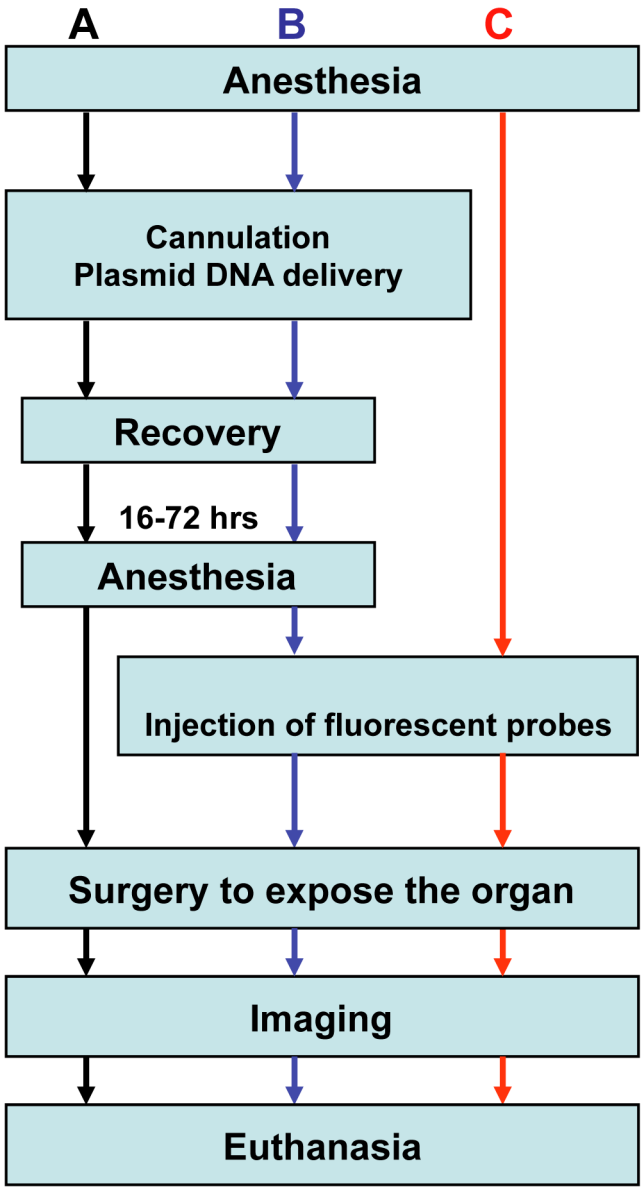

Figure 7. Flowchart of common experimental procedures for intravital microscopy. A. Workflow for imaging only the transfected cells *in vivo*. B. Procedures for imaging a combination of expressed fluorescent proteins and injected fluorescent probes. C. Workflow for visualizing fluorescent probes introduced into the SG tissue. Note, that the injection of the fluorescent probes can be performed while imaging. When imaging transgenic mice in exocytosis eperiments, in some cases the animals were imaged without introducing any exogenous dyes.

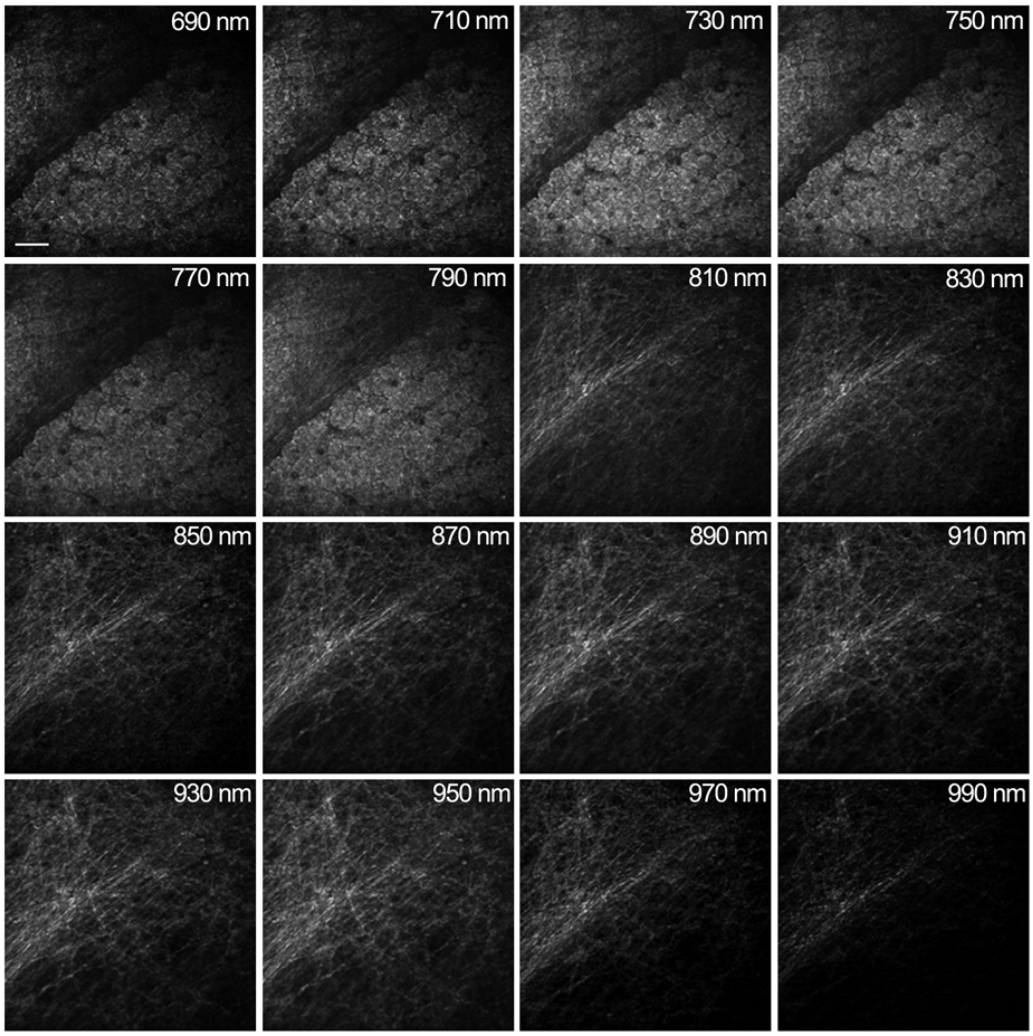

Figure 8. Characterization of endogenous fluorescence from isolated rat submandibular glands. Rat SGs were isolated and imaged close to the surface of the gland, using a 20x water immersion lens. Wavelengths from 690 to 990 nm were used and the power at the objective was maintained around 15 mW. The emitted signal was collected on the external non-descanned detector using a 510 nm dichroic mirror. Excitation below 800 nm produced a signal from the parenchyma of the cell. Above 800 nm predominantly elastic fibers (collagen and elastin) were revealed. Bars 50 µm.

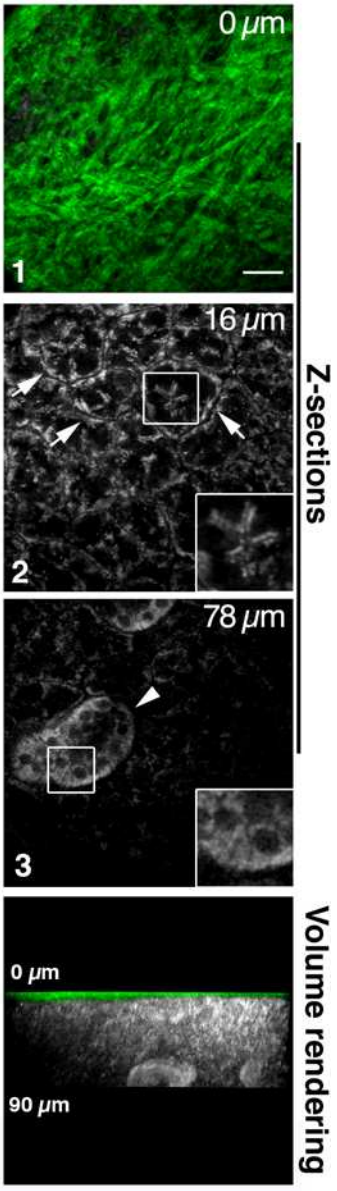

Figure 9. Characterization of the rat submandibular glands by TPM and SHG. Z-stacks and volume rendering of isolated rat SGs - Z-stacks of the same area were acquired exciting first at 750 nm to image the parenchyma (grey) and then at 900 nm to image the elastic fibers (green). Acinar structures (arrows) and striated ducts (arrowhead) are also shown in the insets at a higher magnification. Lower panel - Side view of the volume rendering.

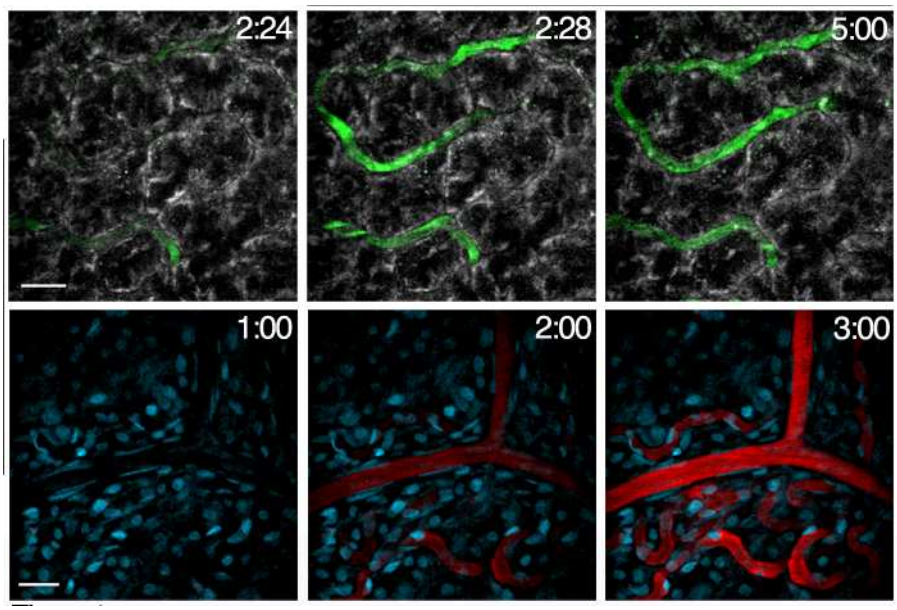

Figure 10. Dynamic imaging of the vasculature in rat salivary glands. 500 kDa FITC-D was injected in the tail artery of a rat (upper panels) or a rat pre-injected with Hoechst 33342 (lower panels) and imaged either at 750 nm to visualize the parenchyma of the glands (upper panels, parenchyma grey, vasculature green) or at 800 nm to image the nuclei (lower panels, nuclei cyan, vasculature red). Time of injection: 2'20" (upper panels) and 1'32" (lower panels). Bars 20 µm

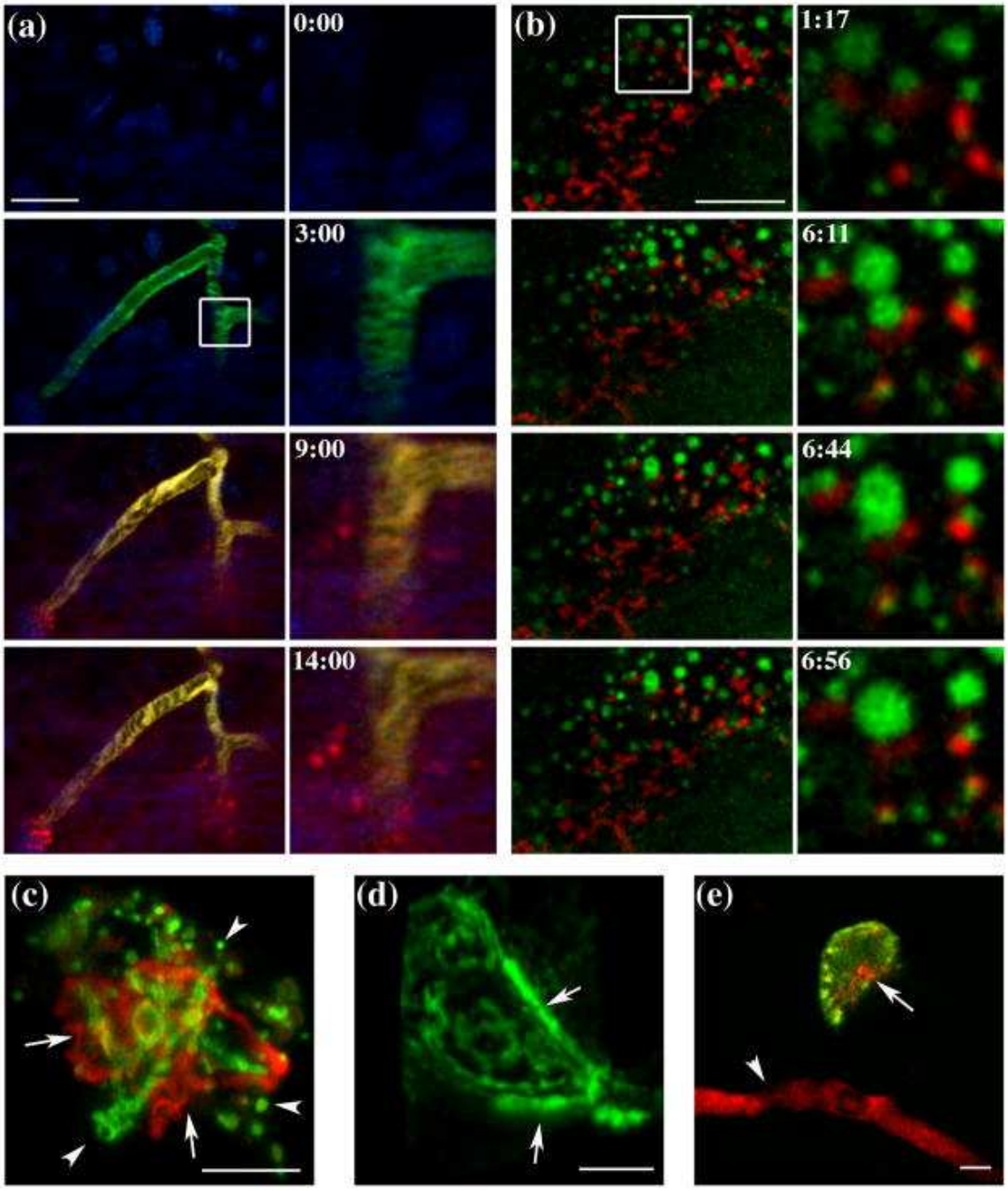

Figure 11. Imaging subcellular structures in live animals. a. Endocytosis of fluorescently labeled dextrans in the salivary glands of live rats. Anesthetized rats were injected with Hoechst to label the nuclei (blue), and imaged in time-lapse using two-photon microscopy. After 2:30 min, a 500 kDa FITC-dextran was injected to label the vasculature (green) and after 6:00 min a 70 kDa Texas-red dextran was injected to image the endocytic process. Endocytic structures appeared right after the injection and they increased in number and in size over time (see supplementary movie 4). Excitation wavelength 820 nm. Scale bar 20 μm. b. Imaging lysosomal fusion in a live animal. Rats were injected with Alexa 488 dextran (green) and Mitotracker (red) and after 4 h the submandibular glands were imaged in time-lapse using single photon confocal microscopy. Two lysosomal structures were caught during

a fusion event (inset). Note the dynamics of both the lysosomes and the mitochondria in supplementary movie 5. Scale bar 5 μm. c–e Gene transduction in live animal. The acinar cells of the salivary glands of live rats were transduced using plasmid DNA encoding for different genes as described in Sramkova et al. (2009). c. Cell expressing TGN38-mCherry, which show the typical TGN ribbon-like structure (red, arrows), and the water channel Aquaporin5-YFP (arrowheads), localized both at the apical plasma membrane and in vesicular structures (arrowheads). d Cell expressing LifeAct-GFP to label F-actin (Riedl et al. 2008). Note the enrichment of F-actin at the apical pole of the plasma membrane. e Cell expressing LifeAct-GFP (green) and TGN-mCherry (red, arrow). Texas-red dextran was also injected systemically in the rat and appeared in a blood vessel (arrowheads; supplementary movie 6). Scale bars 5 μm

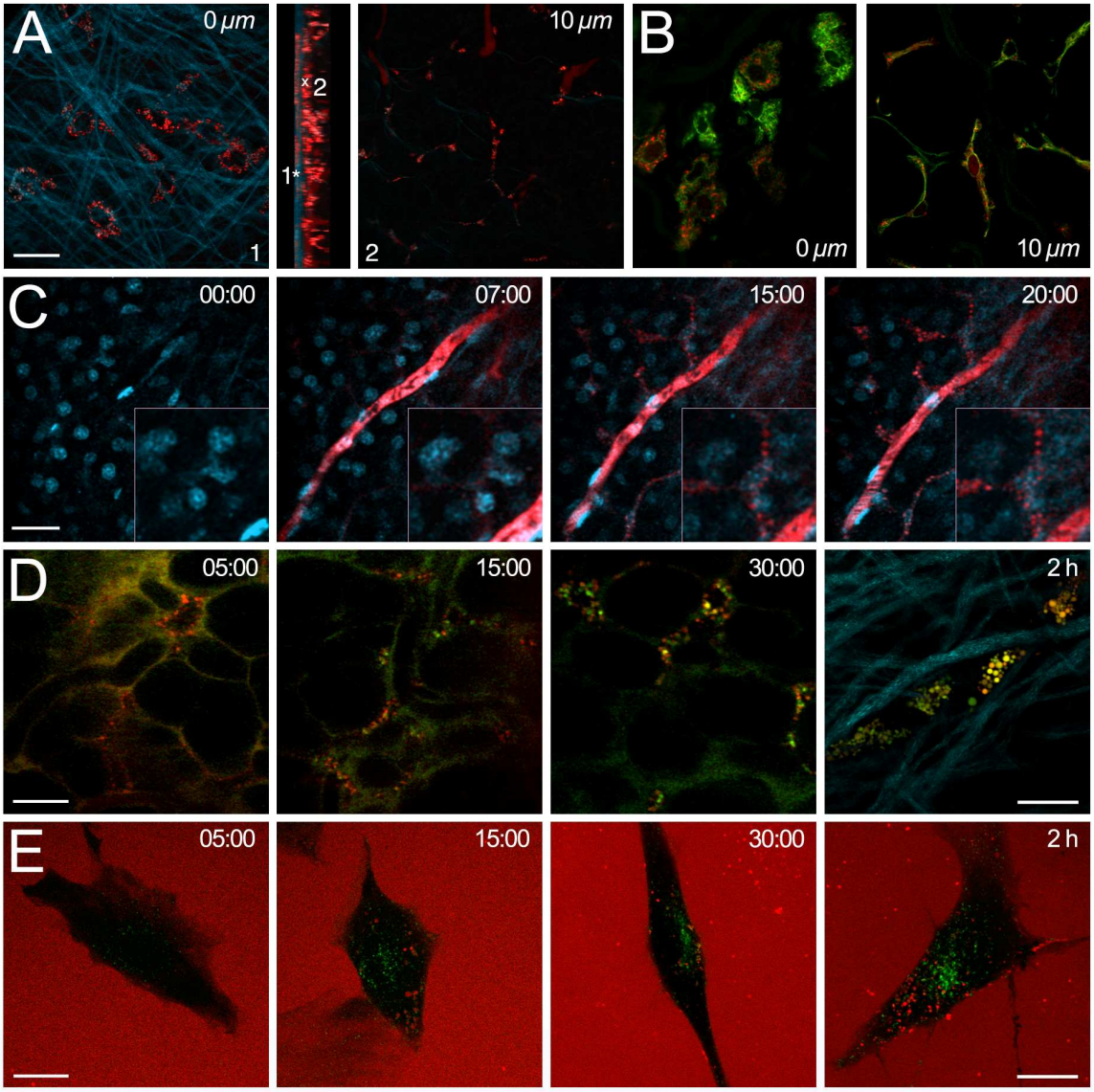

Figure 12. Endocytosis in stromal fibroblasts of the salivary gland. A. Isolated SGs were imaged at different depth from the surface exciting at 830 nm to highlight the elastic fibers covering the gland (cyan) and the TXR-D (red). Center panel – Volume rendering (side view). TXR-D was internalized by cells lying at the surface of the gland (2A-1) or in the stroma surrounding the acini (2A-2). B. SGs were labeled with an antibody directed against vimentin (green) and imaged at the surface (left panel) or deeper into the gland (right panel) exciting at 830 nm. Most of the cells, which internalized dextran were positive for vimentin. C. A rat was injected with 10 µg of Hoechst 33343, the SGs were exposed and imaged at 830 nm. After 2 min and 30 sec, 200 µg of TXR-D were injected into the tail artery highlighting the vasculature almost instantly. After 7 minutes small round structures appeared inside cells adjacent to a blood vessel (inset and arrowheads) which increased overtime both in number (15 min, inset and arrows) and in size (20 min inset and arrows). D. A rat was anesthetized and the SG was prepared for intravital MPM. Prior to imaging 100 µg/ml 70kd Texas Red labeled dextran and 0.5 µg/ml ALEXA-488 labeled Transferrin were injected in the stroma.

First three panels show single frames extracted from different timelapses at 5, 15 and 30 minutes of imaging. Transferrin seems to be internalized separately and at a slower rate than dextran. At 30 min significant overlap of the two probes is seen. A complete overlap is evident in a snapshot of the cell at 2h post-injection (the last panel). E. Same experiment (as in D) was repeated with cultured fibroblasts isolated from rat SG. It is apparent that the internalization kinetics are reversed and the two probes never overlap. Scan speed: 0.3 frame/sec. Bars = 20 µm

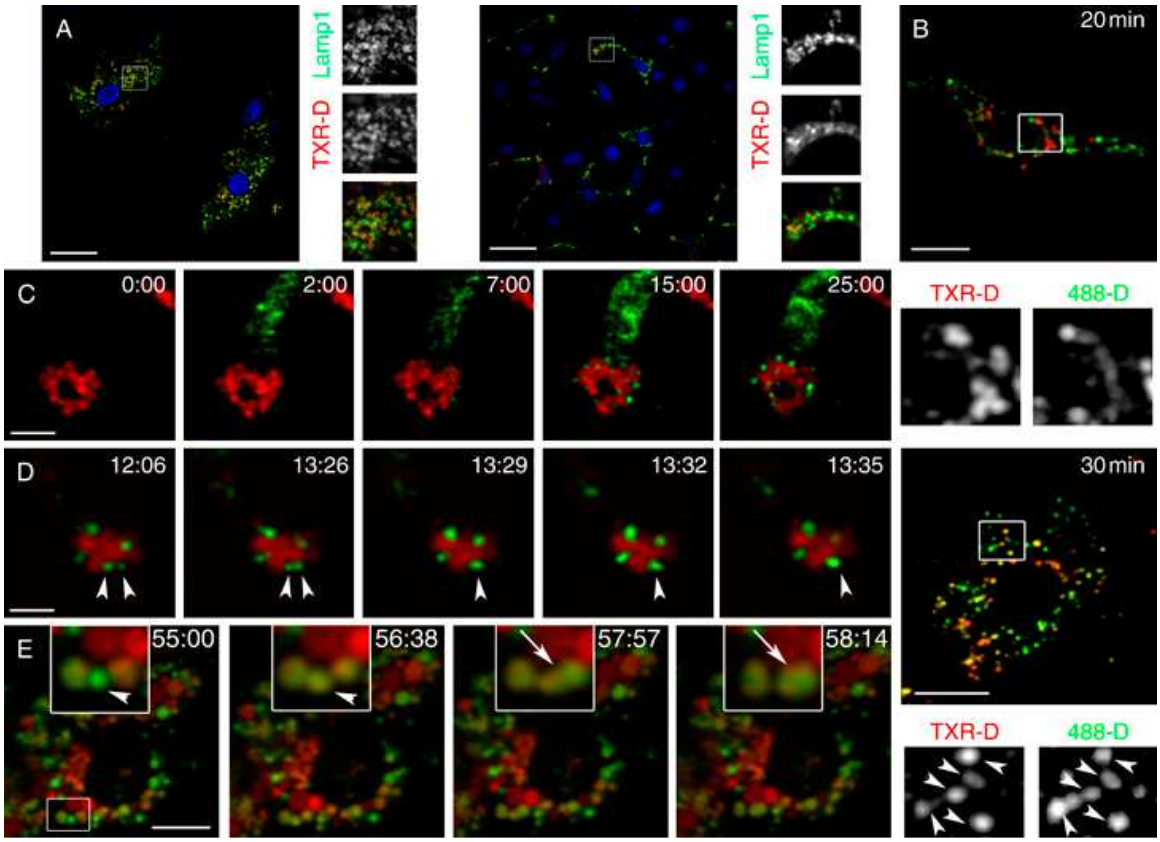

Figure 13. Trafficking of dextran from the early endosomes to the late/endosomes lysosomes. Rats were injected with TXR-D and after 24 h either euthanized (A) or injected with 488-D (B–E). A. SGs were isolated, fixed and labeled with an antibody directed against LAMP-1 (green) and Hoechst 33342 (blue). Images were acquired by confocal microscopy. TXR-D is localized in structures decorated by LAMP-1 (insets) both in cell located at the surface (left panels) and deeper in the tissue (right panels). Bars 20 μm. B. Twenty and 30 min after the injection of the 488-D, the rats were euthanized, the glands were excised and imaged. At 30 min but not at 20 min, a significant colocalization between 488-D and TXR-D was observed (insets and arrowheads). Bars 10 μm. C–E. Dynamic imaging of the trafficking of dextran through the endosomal compartments of live animals. Before the injection of 488-D, the glands were exposed and imaged at 830 nm. TXR-D-containing lysosomes are shown in red. C. In the first 25 min after the internalization, endosomes grow in size but do not fuse with lysosomes. Bars 20 μm. D. Small early endosomes undergo fusion (arrowheads). Bars 20 μm. E. After 55 min from the injection, we observed 488-D-containing endosomes (time 55:00, inset and arrowhead), which acquired first TXR-D (time 56:38, inset and arrowhead) and then fused with a structure containing both 488-D and TXRD (time 57:57 and 58:14, insets and arrows). Bars 10 μm.

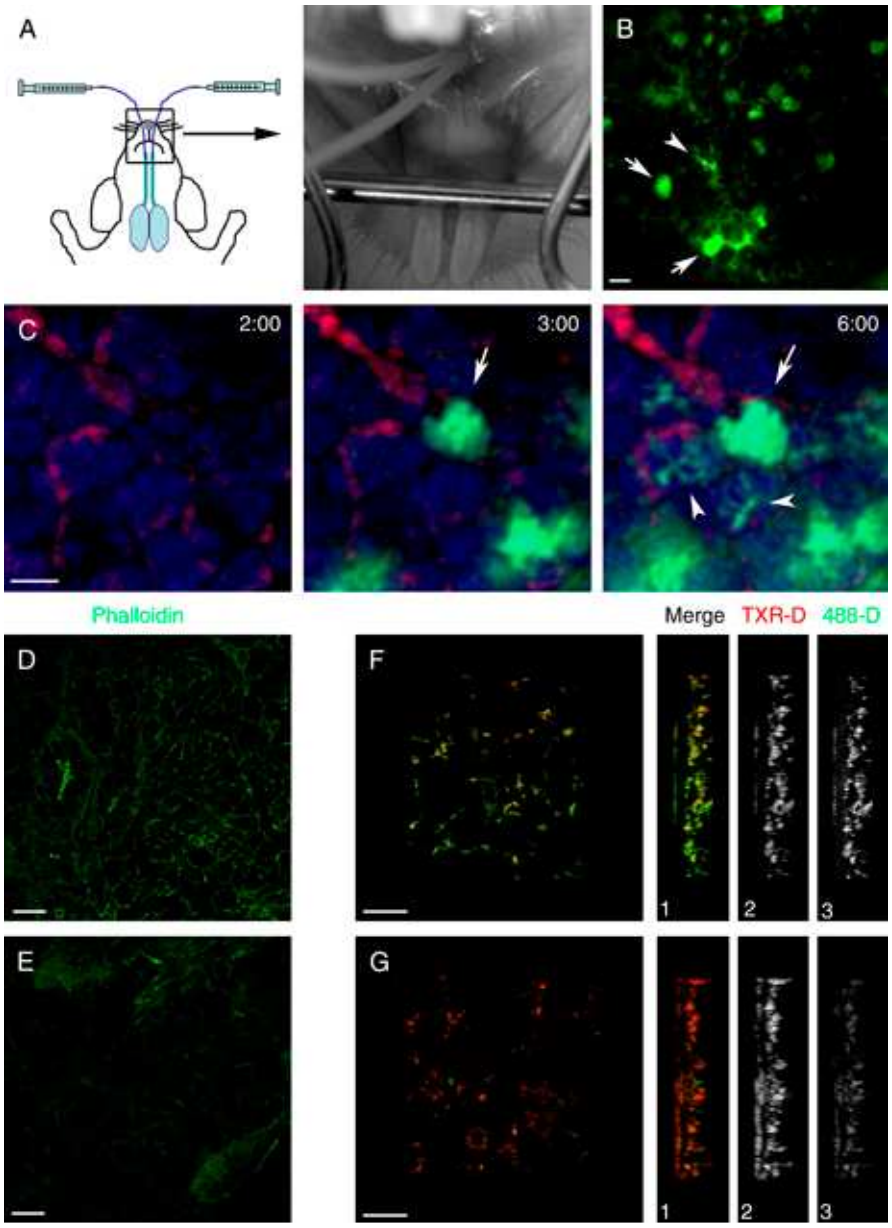

Figure 14. Delivery of molecules to the rat salivary glands through the Wharton's duct. A. Cannulation of the Wharton's duct. The rats were placed onto an adjustable stage, and two thin cannulae were inserted into the Wharton's ducts from the orifices below the tongue (right panel, arrowhead). B and C. Injection of 488-D into the Wharton's duct. Twenty micrograms of 488-D were injected through the cannula into the Wharton's duct either alone (B) or in combination with 200 μg of systemically injected TXR-D (C). B. Snapshot showing the SGs after 5 min after injection of 488-D. Arrows point to the cross section of large ducts, while the arrowhead points to a series of smaller ducts. C. The SG was exposed and imaged at 750 nm to highlight the parenchyma of the SGs. The vasculature is shown in red. 488-D (green) appeared first in large ducts (arrows) and later in smaller ducts and acini canaliculi (arrowheads). D–G. Effect of LatA and CytD on the SGs. TXR-D was systemically injected in a rat. After 1 h, two cannulae were inserted in the Wharton's ducts, and one of the glands

was injected with 10 μm LatA, while the other was injected with the vehicle (control). After 45 min, the rat received a systemic injection of 488-D, and 1 h later, the animal was euthanized. First, the glands were imaged at 830 nm (F and G) and then frozen and processed for cryosections and immunolabeling (D and E). D and E. Both glands were sectioned, labeled with Alexa 488–phalloidin and imaged by confocal microscopy. F and G. 3D reconstructions of the first 60 μm below the surface of the glands. The levels of TXR-D (red) that was injected before Lat A were not affected, while the amount of internalized 488-D (green) was substantially reduced (side view). Bars 20 μm.

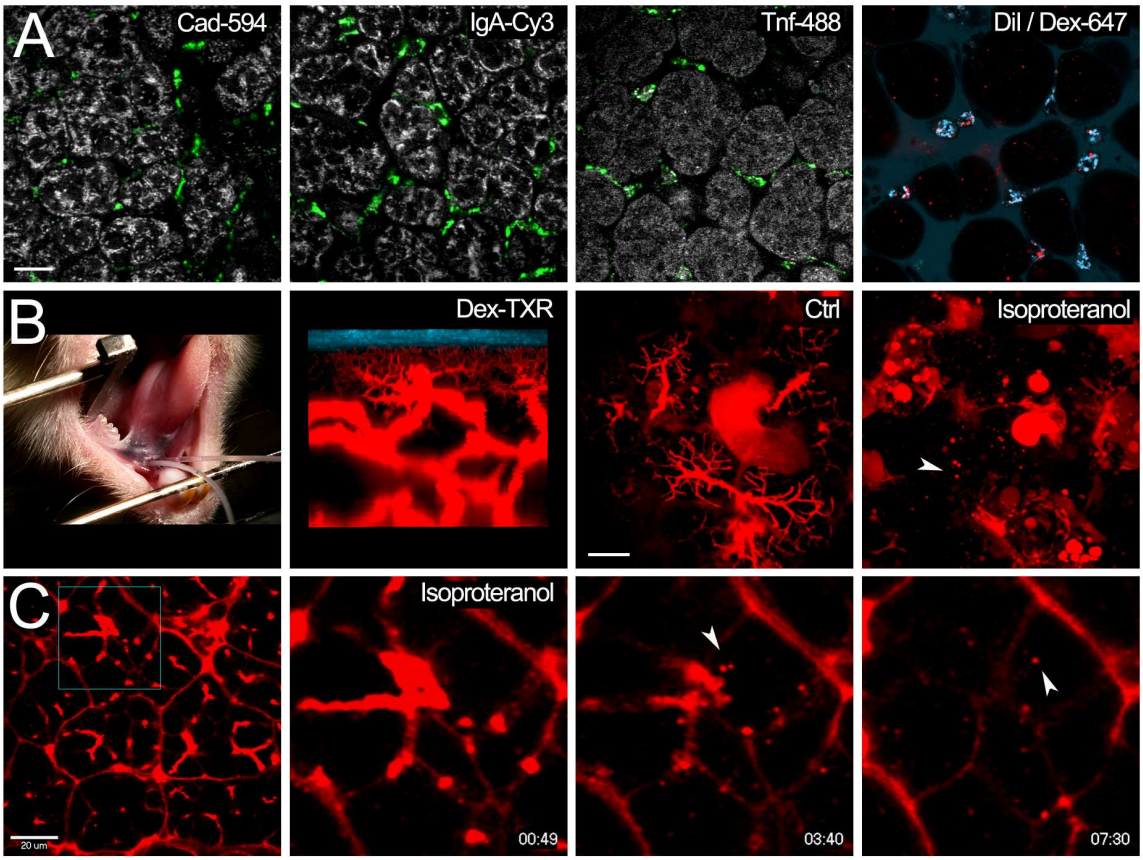

Figure 15. Compensatory endocytosis in the acinar cells of the salivary gland.
A. Cadaverin-594, monomeric IgA-Cy3, Transferrin-488 (green), 10kDa Dextran-647 (cyan) and DiI (red) were injected into the stroma of SG and the glands. After 1h the glands were excised and imaged by MPM (first three panels) or confocal microscopy (last panel). All the probes except the lipophilic DiI probe are excluded from the epithelium implicating the existence of barrier to basolateral endocytosis. Panels 1-2 show rat SG and 3-4 show mice SG. B. Image showing a rat with cannulated Wharton's ducts (first panel). A 3D stack of 150 µm thickness was acquired in a live rat while 10kDa Dextran-TXR (red) was infused into the ductal system by gravity. Side view of the volume rendering is shown with ductal system and collagen layer (cyan) visible. Top-down MIP of 20 µm thick 3D stack (panels 3-4) showing 10kDa Dextran-TXR (red) gravity infused SG before and after isoproteranol treatment. Dextran infused by gravity labels the ductal system of the gland but is not internalized by the epithelium. After stimulation with 0.5 mg/kg isoproteranol acinar cells endocytose Dextran-TXR at the apical side (arrowhead) C. Timelapse sequence showing compensatory endocytosis of gravity infused 10kDa Dextran-TXR after isoproteranol stimulation in live rat. Bars = 20 µm

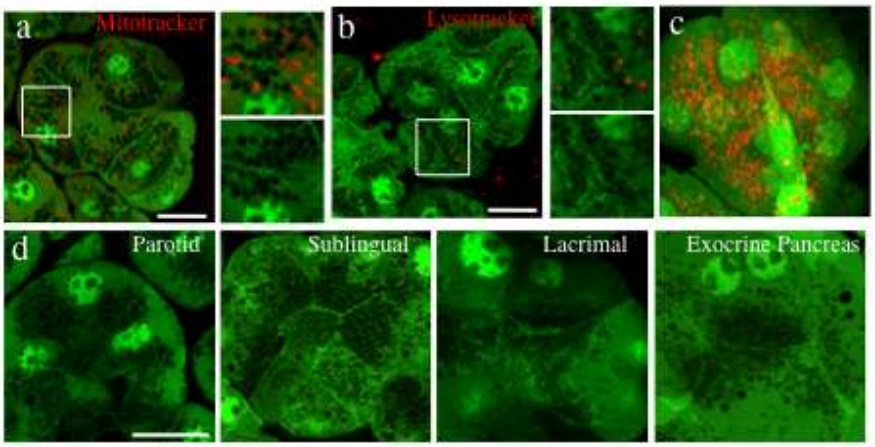

Secretory granules per acinus	2300-3100
Cells per acinus	9-10
Diameter of the granules (μm)	1.30 – 1.60
Diameter of the canaliculi (μm)	0.3-0.4

Figure 16. Characterization of the SCGs in the GFP mouse model. a-b. Submandibular salivary glands were exposed and bathed with the vital dyes Mitotracker (a), and Lysotracker (b) to label mitochondria and lysosomes, respectively, as described in the Materials and Methods section. Minimal or no overlap was observed with the SCGs. Bars, 10 µm. c. Volume rendering of an entire acinus in the submandibular SGs. The SCGs were color coded in red and the number of the SCGs and their diameter, the number of cells per acinus and the diameter of the canaliculi were measured from 5 acini and reported in the table. d. Parotid, sublingual, and lacrimal glands and the pancreas were excised and immediately imaged. The morphology of SCGs and the APM was similar to that of the submandibular SGs. Bar, 10 µm.

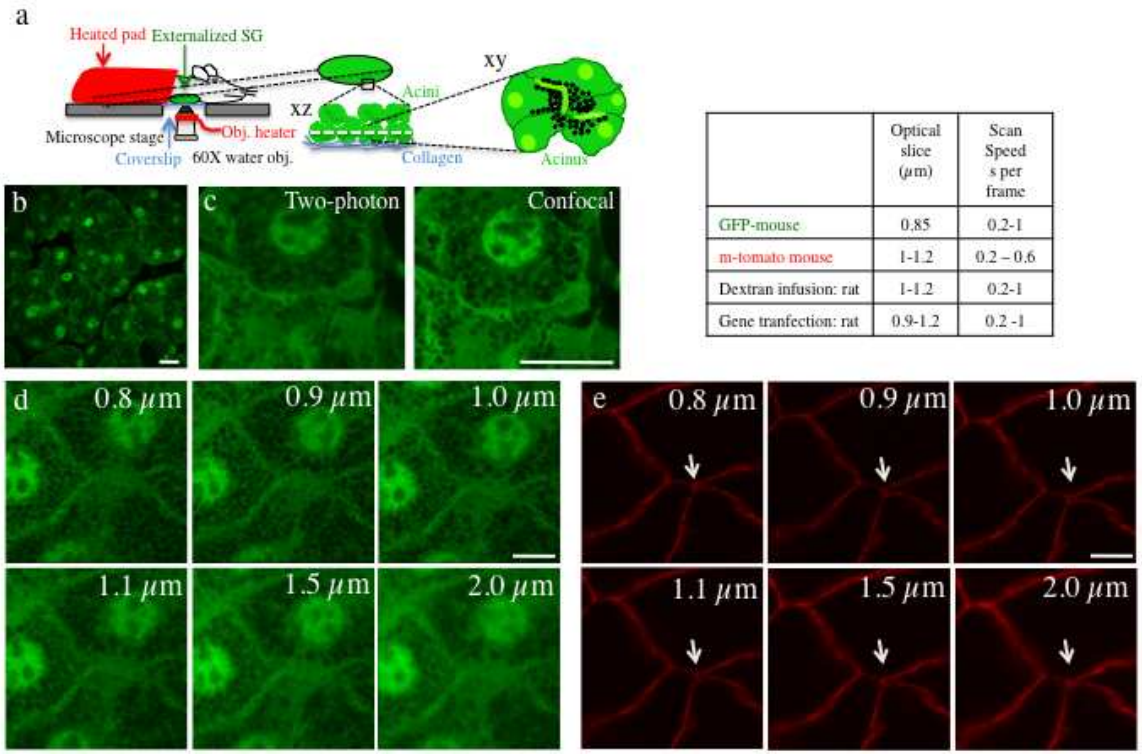

	Optical slice (μm)	Scan Speed s per frame
GFP-mouse	0.85	0.2-1
m-tomato mouse	1-1.2	0.2 – 0.6
Dextran infusion: rat	1-1.2	0.2-1
Gene tranfection: rat	0.9-1.2	0.2 -1

Figure 17. Optimization of the parameters to image the large SCGs. a. Diagram showing the preparation of the rodents for intravital microscopy. The animals were anesthetized and the SGs were exposed as described in the Materials and Methods. The animals were placed on the stage of the microscope with the SGs facing a glass coverslip mounted on the stage. b-c. Comparison between two-photon and confocal microscopy. The SGs of anesthetized GFP-mice were exposed and imaged *in situ* by either two-photon microscopy using an excitation wavelength of 930 nm (b and c, left panel) or confocal microscopy using an excitation wavelength of 488 nm (c, right panel). Bars, 10 µm. d-e. Optimization of the thickness of the optical slice. The salivary glands of a mouse expressing both GFP and m-Tomato were exposed and imaged by confocal microscopy using an excitation wavelength of 488 nm (d) or 594 nm (e). The pinhole was adjusted as indicated. The best resolution to image the SCGs was achieved when the thickness of the optical slice was set at 0.8 µm (the lowest limit for our microscope), whereas the best visualization of the apical plasma membrane was achieved by setting the pinhole between 1 and 1.2 µm (arrow). The table summarizes the imaging conditions utilized in this study. Bars, 5 µm.

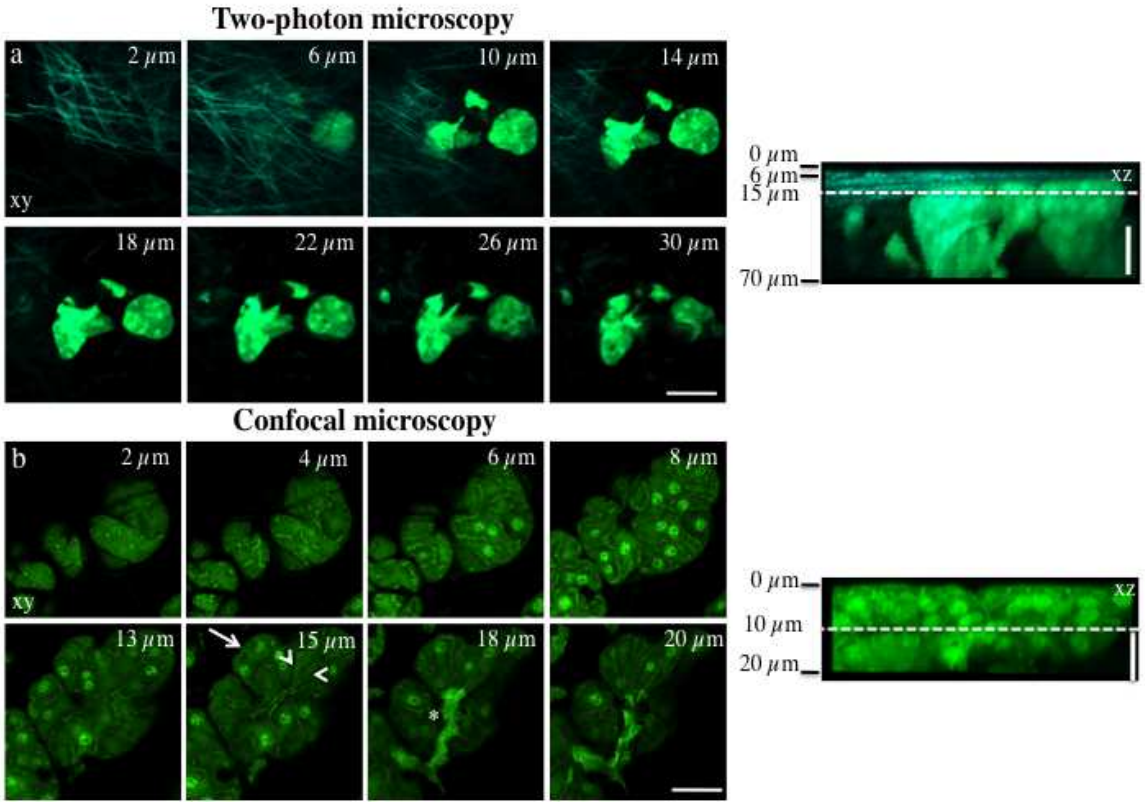

Figure 18. Optimization of the imaging depth in live animals. The GFP mice were anesthetized, the submandibular SGs were exposed, and imaged either *in situ* by using two-photon microscopy (a) or fixed by perfusion (see Materials and Methods), excised, and imaged by confocal microscopy (b). a. Z scan was performed from the surface of the gland using an excitation wavelength of 930 nm (step size 1 µm, 60 X water immersion objective N.A. 1.2 from Olympus). Collagen fibers detected by second harmonic generation (cyan) are at the surface of the glands, and below the acini (green). Right panel, view of the xz maximal intensity projection. Dotted line represents the optimal imaging depth. Bars, 20 µm. b. Z scan was performed using an excitation wavelength of 488 nm (step size 1 µm). Acini (arrow), acinar canaliculi (arrowheads), and the intercalated duct (asterisk) are shown. Bar, 20 µm. Right panel, view of the xz maximal intensity projection. Dotted line represents the optimal imaging depth.
Bar, 10 µm.

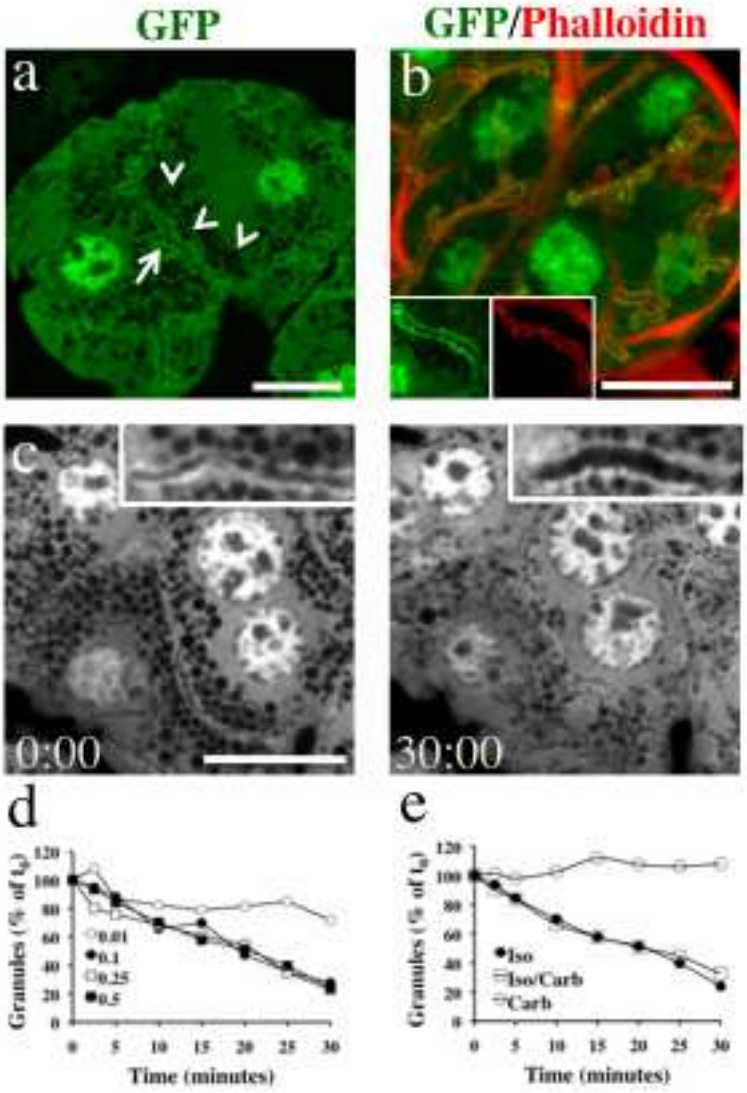

Figure 19. A transgenic mouse model for dynamic imaging of the SCGs the APM *in vivo*. The submandibular SGs of anesthetized GFP-mice were imaged *in situ* by IVM (a,c) or excised and labeled with TRITC-phalloidin to reveal the actin cytoskeleton (b). a. Cytoplasmic GFP (green) is excluded from the SCGs (arrowheads) and it is enriched at the APM (arrow). b. The APM is enriched in GFP (green) and actin as revealed by counter-staining with TRITC-phalloidin (red). Insets. High magnification of a canaliculus. c. The anesthetized GFP-mice received a subcutaneous (SC) injection of 0.5 mg/Kg Iso and the SGs were imaged in time-lapse. Acinus imaged at the moment of Iso injection (left panel) or after 30 min (right panel, see Movie 2 and 3). High magnification of the canaliculi (insets). Bars, 10 µm. d-e. Quantitation of the degranulation of the SCGs. Data shown are measurements from a single acinus. The experiments were performed 3 times with similar results. d. Exocytosis in response to various doses of Iso: 0.01 mg/Kg (empty circles), 0.1 mg/Kg (filled circles), 0.25 mg/Kg (empty squares) and 0.5 mg/Kg (filled squares). e. Exocytosis in response to muscarinic or adrenergic stimulation: 0.01 mg/Kg Carb (empty circles), 0.1 mg/Kg Iso (filled circles) or both (empty squares).

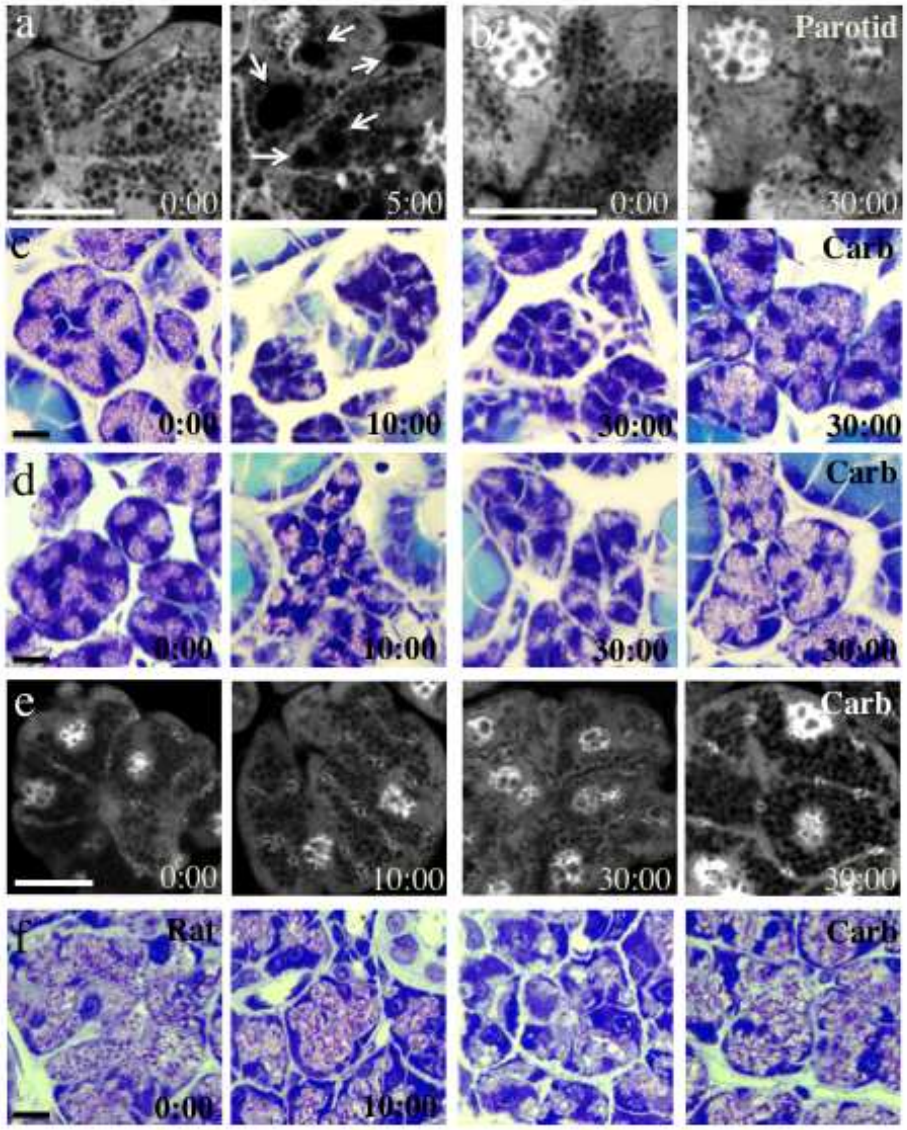

Figure 20. Characterization of the stimulus regulating the fusion of the SCGs in SGs. a,b. The submandibular (a) or the parotid (b) glands of anesthetized GFP mice were exposed and the animals injected SC with 1 mg/Kg (a) or 0.5 mg/Kg (b) Iso. a. After 5 minutes from the injection, large vacuoles formed in the cytoplasm (arrows) and exocytosis was blocked. b. Exocytosis of SCGs in the parotid glands proceeded with similar characteristics to that of the submandibular glands. c-f. Anesthetized GFP mice (c,e), wild type FVB mice (d) or Sprague-Dawley rats (f) were injected with 0.1 mg/Kg Iso or 0.045 mg/Kg Carb. The animals were perfused with a fixative solution at noted time-points as described in the Methods Section, SGs were excised and either imaged by confocal microscopy (e) or stained with toluidine blue (c,d,f). When injected with Iso, the degranulation occured at a very similar rate in all the animals tested. Carb did not elicit any exocytosis of the SCGs whereas water secretion was stimulated. Bars, 10 µm

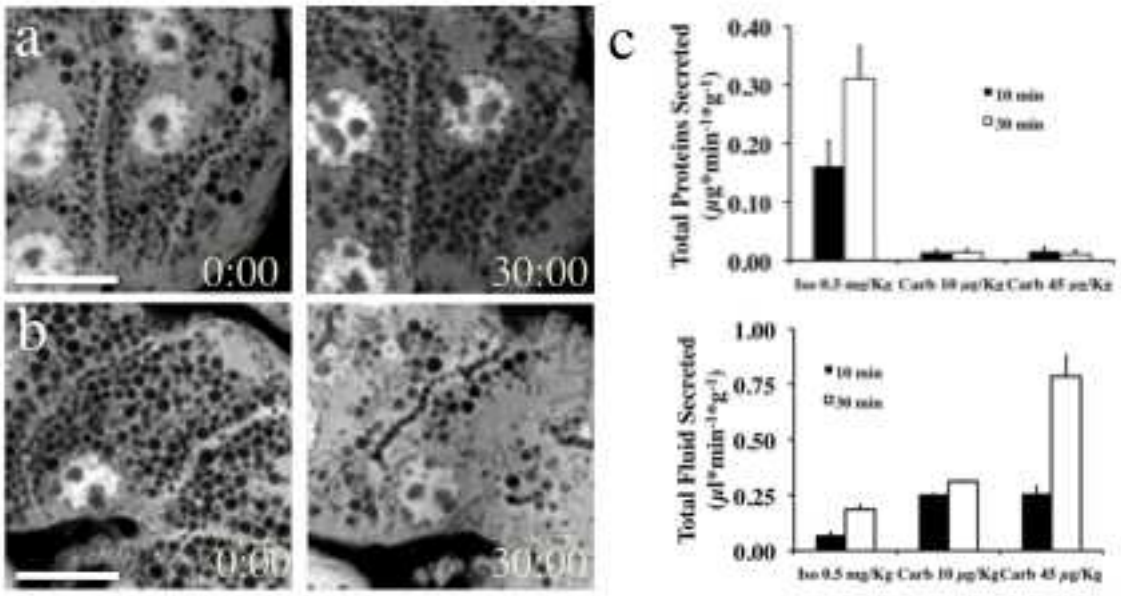

Figure 21. Carbachol stimulates water secretion in the SGs of live animals but not SCGs exocytosis. a,b. Anesthetized GFP mice were injected with 0.015 mg/Kg Carb either alone (a), or in combination with 0.1 mg/Kg Iso (b), and imaged in time-lapse mode. Snapshots at time 0 or 30 min after the injection are shown. Bars, 10 µm. Almost complete degranulation occurred after 30 min of Iso treatment. c, Sprague-Dawley rats were anesthetized and the saliva from the submandibular glands was collected upon injection of 0.5 mg/Kg Iso , 0.01 mg/Kg Carb or 0.045 mg/Kg Carb. Protein (upper panel) and fluid (lower panel) secretion were determined after 10 and 30 min from the injection. Data are average +/- s.e.m of 3 independent experiments.

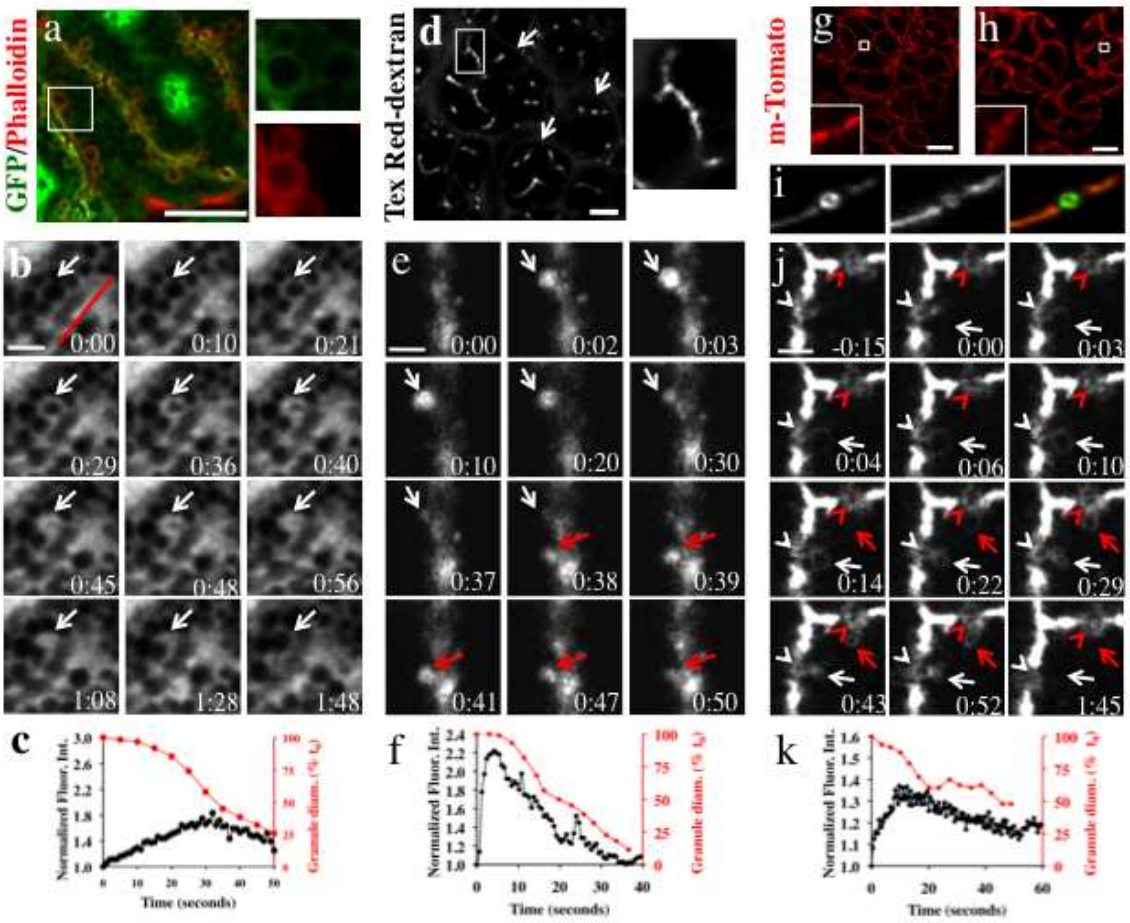

Figure 22. SCGs completely collapse after fusion with the APM. a. SCGs close to the APM are enriched in GFP. Anesthetized GFP-mice were injected SC with 0.1 mg/Kg Iso and after 10 min, excised and labeled with TRITC-Phalloidin. Granules close to the APM are coated with actin (red) and also enriched in GFP (green). Bar, 10 µm. b. Time series of a single granule (white arrows) fusing with the APM (red line) (red arrowheads). Bar, 3 µm. c. Quantitation of both the GFP fluorescence intensity around a SCG (black circles) and its diameter (red circles) during Iso-stimulated exocytosis. Data shown are from a single event. 5 events per animal were measured in two independent experiments. d-f. 10 kDa Texas Red-dextran was infused by gravity into the salivary ducts of a live anesthetized rat. The SGs were exposed and imaged by confocal microscopy. d. Canaliculi are highlighted in the acini (arrows). Inset. High magnification of a canaliculus. Bar, 10 µm. e, f. 0.1 mg/Kg Iso was injected SC. e. Time-lapse sequence. Upon the opening of the fusion pore, dextran enters two SCGs (white and red arrows) enabling their visualization. Bar, 3 µm. f. The fluorescence intensity of the dextran inside the granule shown in e (white arrows) was measured (black circles) and correlated with its diameter (red circles) as described in the Materials and Methods. Data shown are from a single event. 4-5 events per animal were measured in two independent experiments. g-j. Anesthetized m-Tomato mice were left untreated (g,i) or injected with Iso (h,j,k). The SMGs were imaged *in situ* (g,h,j) or labeled with TRITC-

phalloidin (i). Acinar canaliculi in cross section (g, h inset and i). j. Time series of the collapse of two SCGs revealed by the diffusion of the m-Tomato from the APM (white and red arrows). Note the expansion of the canaliculi (white and red arrowheads). Bar, 3 µm. k. The fluorescence intensity of the m-Tomato at the surface of a granule (black circles) and its diameter (red circles) were measured as described in the Materials and Methods. Data shown are measurements of a single event. 6-10 events per animal were recorded in 3 independent experiments.

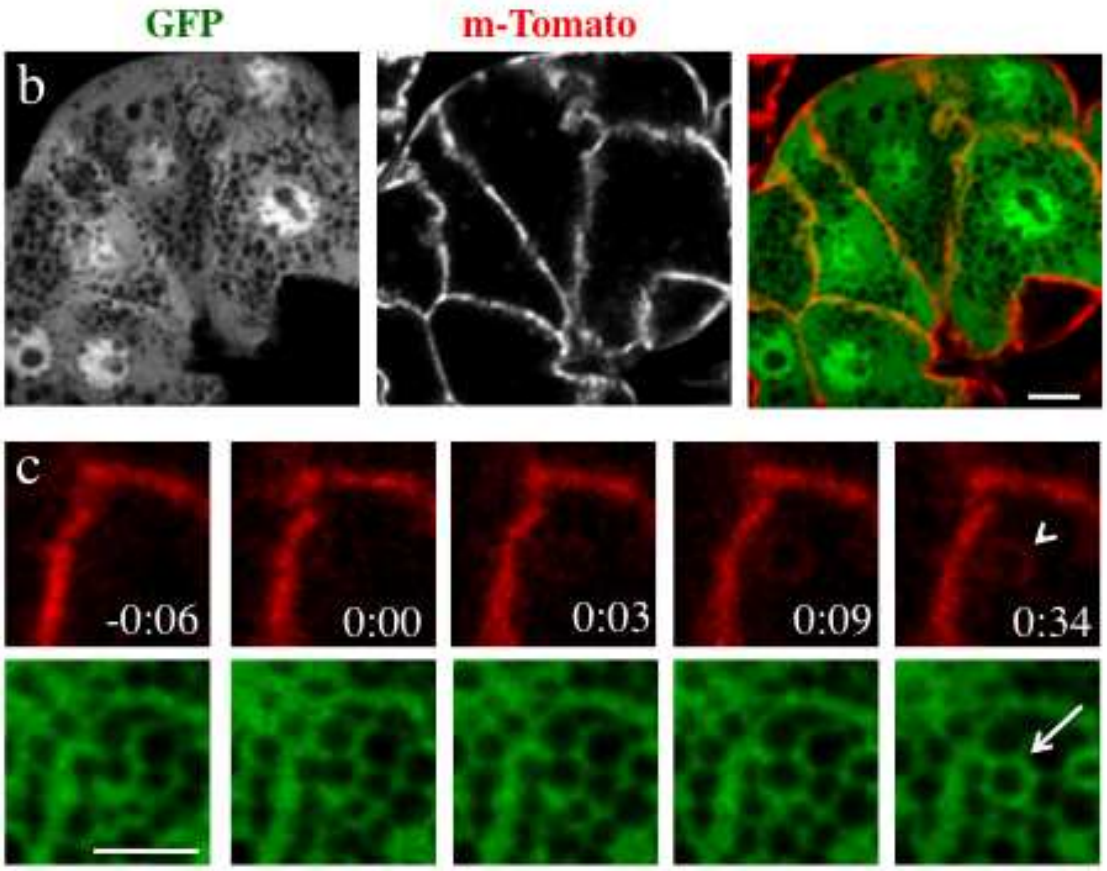

Figure 23. The granules observed in the GFP-mice are filled by dextran injected into the acinar canaliculi and are equivalent to those observed in the m-Tomato mice. a- 10 kDa Alexa 647-dextran was infused by gravity into the salivary ducts of a live anesthetized GFP-mouse. The SGs were exposed and imaged by confocal microscopy. 0.1 mg/Kg Iso was injected SC. Upon opening of the fusion pore, dextran enters a SCGs (arrows) enabling its visualization Bar, 5 µm Inset. High magnification of the SCG Bar, 2 µm b-c, GFP-mice were crossed with m-Tomato mice (GFP/m-Tomato mouse). The submandibular glands were exposed and imaged *in situ* either in resting conditions (a) or upon stimulation with 0.5 mg/Kg Iso (b). a, The submandibular salivary glands were exposed and imaged *in situ*. Bar, 5 µm. b, Time-lapse series of a secretory granule. The granule fused with the APM as indicated by m-Tomato diffusing from the APM into the membrane of the granule (arrowhead). The GFP fluorescence increased around the granule (arrow) shortly after fusion. Bar, 3 µm.

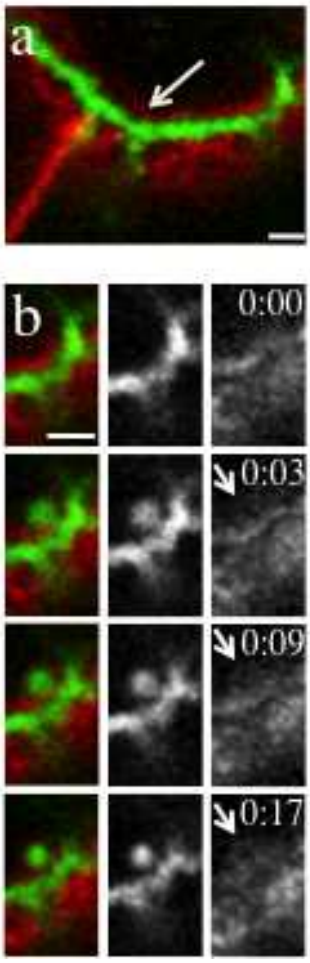

Figure 24. Membranes diffusion into the secretory granules from the apical plasma membrane and opening of the fusion pore. a-b. 10 kDa Alexa 488-dextran (green) was infused by gravity into the salivary ducts of a live anesthetized m-Tomato mouse (red). a. The SGs were exposed and imaged by confocal microscopy. The arrow indicates the APM (red). b. 0.1 mg/Kg was injected and the glands imaged as described in Materials and Methods. Arrows point to the APM diffused into the SCG. Bars, 2 µm.

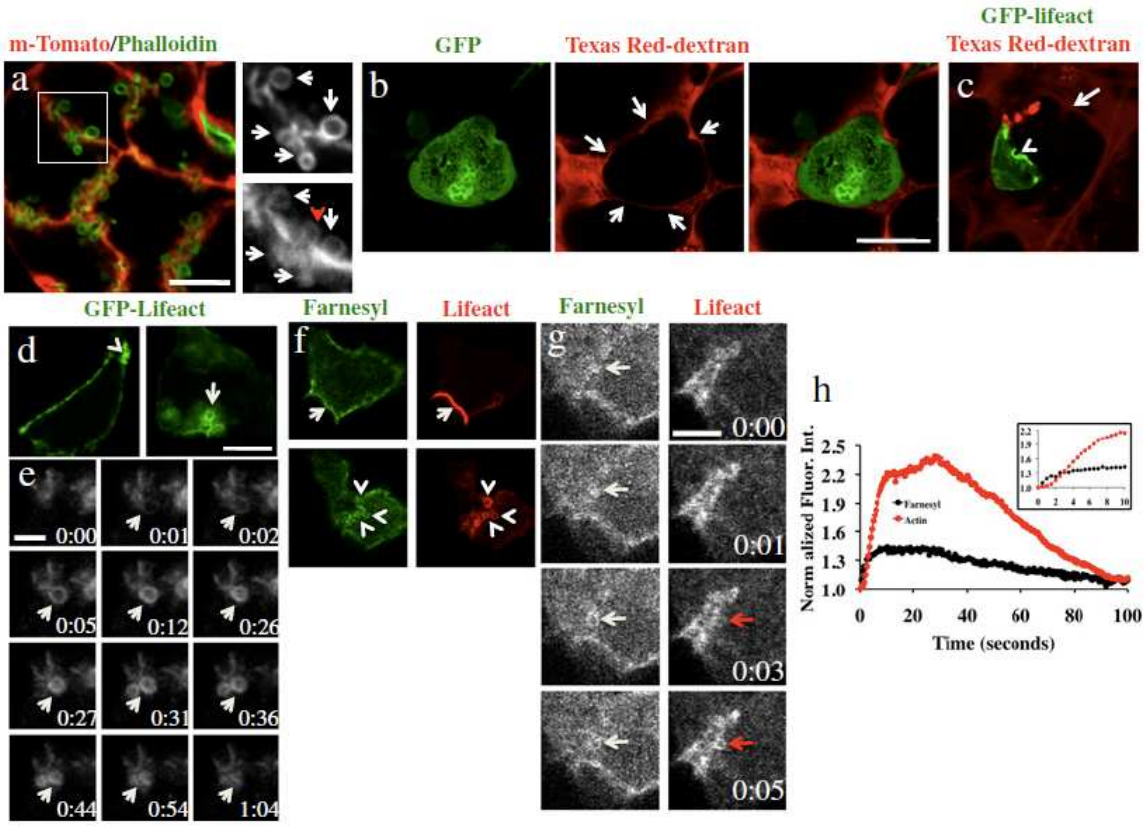

Figure 25. Actin recruitment onto the SCGs at the APM. A. m-Tomato mice were injected with 0.5 mg/Kg Iso, and after 10 min the SGs were excised and labeled with Alexa 488-phalloidin. All the SCGs coated with actin were also labeled with m-Tomato (Inset, white arrows). A granule labeled with m-Tomato is not coated with actin (red arrowhead). (Scale bar, 10 μm.) B. The SGs of anesthetized GFP mice were exposed and incubated with 10 kDa of Texas Red-dextran as described in Materials and Methods. After 10-15 min, the SGs were imaged by confocal microscopy using 488 nm and 561 nm as excitation wavelengths. Texas Red-dextran labels the stroma and the basement membranes (red, arrows), highlighting the acinar structures (green). (Scale bar, 10 μm.) C. A Sprague–Dawley rat was anesthetized, and GFP-lifeact was transfected as described in Materials and Methods. The SGs were exposed and incubated with 10 kDa of Texas Red dextran to reveal the acinar structures (red). The acinar cell expressing GFP-lifeact (green) is localized in the acinus (arrow). GFP-lifeact is accumulated in acinar canaliculi (arrowhead). (D–G) GFP-lifeact was transfected alone in the SGs of a live rat (D and E), whereas RFP-lifeact was tranfected together with GFP-farnesyl (F and G). The animals were injected with 0.1 mg/Kg Iso, and the SGs were imaged as described. D. Single acinar cells showing GFP-lifeact enriched at the APM in resting conditions (Left, arrowhead) and recruited onto the SCGs upon stimulation (Right, arrow). E. Time-lapse sequence of the recruitment of GFP-lifeact onto the SCGs (arrows). (Scale bars, 3 μm.). F. RFP-lifeact was enriched at the APM (Right, arrows) whereas GFP-farnesyl (Left) localized at the PM similarly as m-Tomato. Upon stimulation with Iso, RFP-lifeact was recruited to SCGs that are also labeled with GFP-Farnesyl (Lower, arrowheads). G. Time-lapse sequence showing that, upon Iso treatment, GFP-farnesyl (white arrows) diffuses into the SCGs before the recruitment of actin (red arrows). H. Fluorescence

intensity of the RFP-farnesyl at the surface of the whole granules (black circles). The levels of GFP-lifeact recruited (red circles) were measured as described in Materials and Methods. Data shown are measurements from a single event. Seven to 10 events per animal were recorded in three independent experiments.

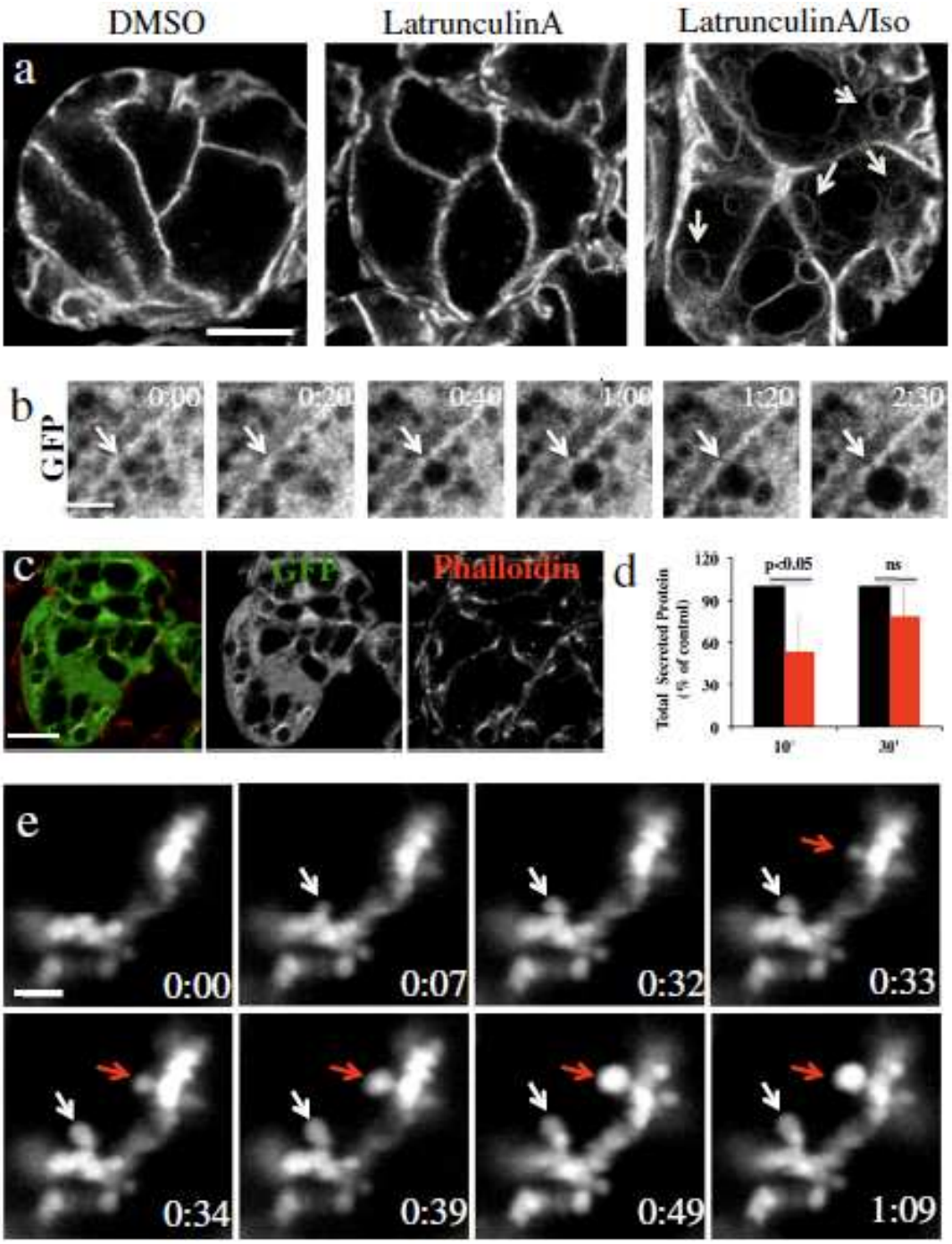

Figure 26. Characterization of the effect of the actin-disrupting agents on exocytosis of the SCGs. A. LatA blocks the collapse of the SCGs. The SGs of the m-Tomato mice were exposed to 10 μM LatA (Center and Right) or to 0.5% DMSO (Left). After 20 min, the animals received an s.c. injection of 0.1 mg/kg Iso (Right). The SGs were imaged *in situ*. Large vacuoles were observed in the cytoplasm of the acinar cells (arrows). (Scale bar, 10 μm.) B. The secretory granules increase in size upon fusion with the apical plasma membrane and disruption of the actin cytoskeleton. The SGs of the GFP mice were exposed to 10 μM cytochalasin D (CytD). After 20 min, the animals received an s.c. injection of 0.1 mg/kg Iso,

and the glands were imaged *in situ*. (Scale bar, 5 μm.) C. The SGs were removed 30 min after Iso injection and labeled with TRITC–phalloidin. Note that cells are filled with large vacuoles and small SCGs are no longer detectable (Left). The actin cytoskeleton is disrupted and does not coat the vacuoles (Right). (Scale bar, 10 μm.) .D. Sprague–Dawley rats were anesthetized and treated with 10 μm CytD as described in Materials and Methods. The Wharton's duct was cannulated, and saliva was collected 10 and 30 min after Iso stimulation. The total amount of protein secreted was determined. Data are averages ± SEM of four independent experiments. E. The opening of the fusion pore is not affected by the impairment of the actin cytoskeleton. Texas Red–dextran (10 kDa) was infused by gravity into the salivary ducts of a live anesthetized rat. The SGs were exposed and incubated for 20 min with 10 μm CytD. Iso (0.1 mg/kg) was injected s.c., and the SGs were imaged by confocal microscopy. Time-lapse series showing that the Texas Red–dextran immediately fills a fused granule (white and red arrows) that expands in size and does not collapse. (Scale bar, 3 μm.)

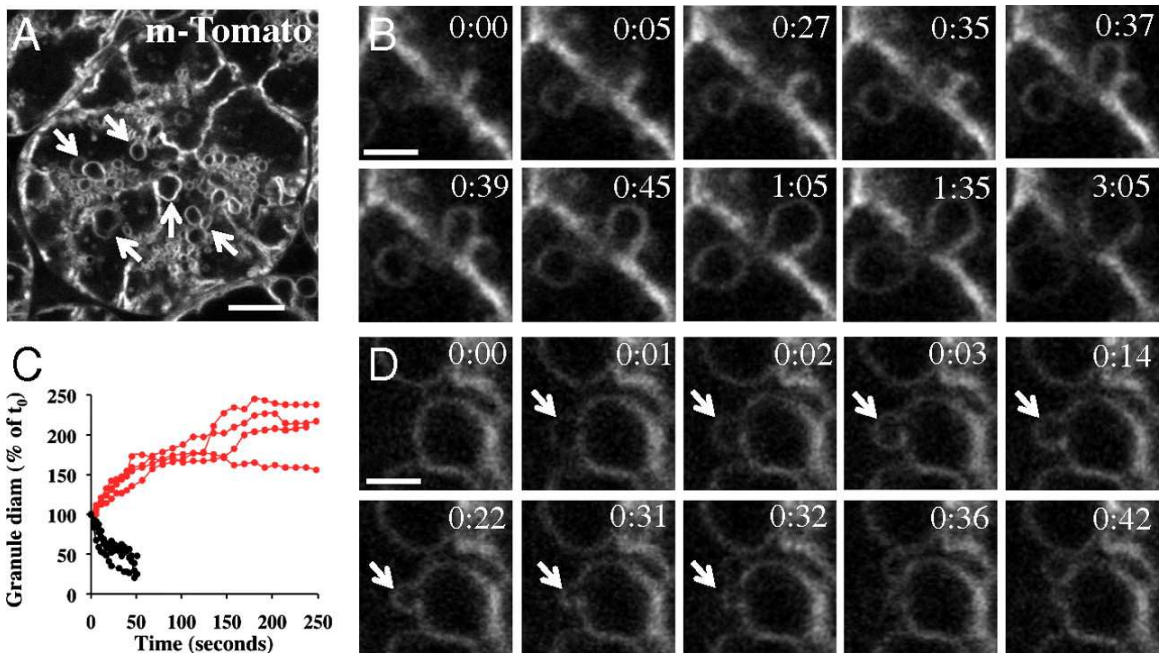

Figure 27. Role of the actin cytoskeleton in facilitating the collapse of the SCGs. A–D. The SGs of the m-Tomato mice were exposed to 10 μM CytD, and after 20 min the animals received a s.c.injection of 0.1 mg/kg Iso. A. The SGs were exposed and imaged *in situ*. Large vacuoles were observed in the cytoplasm of the acinar cells (arrows). (Scale bar, 10 μm.) B–D. Time-lapse sequence of SCGs after fusion with the APM, 2 min (B) or 10 min (D) after the injection of Iso. B. The SCGs fuse with the APM, do not collapse, and form large vacuoles. (Scale bar, 3 μm.). C. Quantitation of the diameter of the vacuoles that fail to collapse after fusion with the APM in the presence of CytD (red circles) and of the granules that fuse under control conditions (black circles). Data shown are from four granules in the same acinus. A total of 10–15 granules were analyzed in two independent experiments. D. A SCG fuses with a large vacuole and rapidly collapses (arrows)

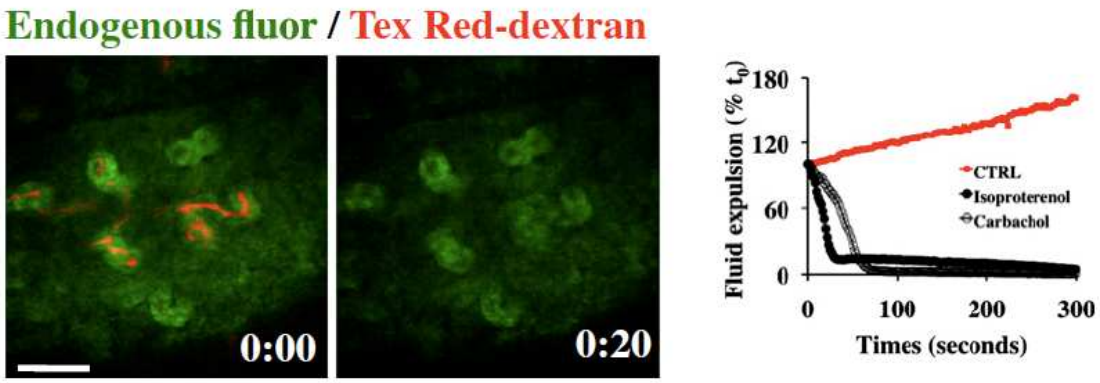

Figure 28. Hydrostatic pressure is generated in the salivary ductal system upon stimulation with Iso. The salivary glands of a Sprague–Dawley rat were cannulated, and a 10-kDa Texas Red–dextran was infused by gravity into the Wharton's duct. The glands were exposed and imaged *in situ* using two-photon microscopy, exciting at 740 nm to reveal the parenchyma of the glands, as described previously (1). Upon injection of 0.5 mg/kg of Iso, the dextran was rapidly expelled from the ductal system and cleared in 20 s (Movie S13). This rapid expulsion can be explained by the secretion of fluid from the acini rather than by protein secretion. (Scale bar, 50 μm.) The graph shows the quantitation of the expulsion of the dye when the animal is injected with saline (red circles), 0.5 mg/kg Iso (black circles), or 0.045 mg/kg Carb (white circles). Data shown are based on a single duct. The experiment was repeated four times with similar results.

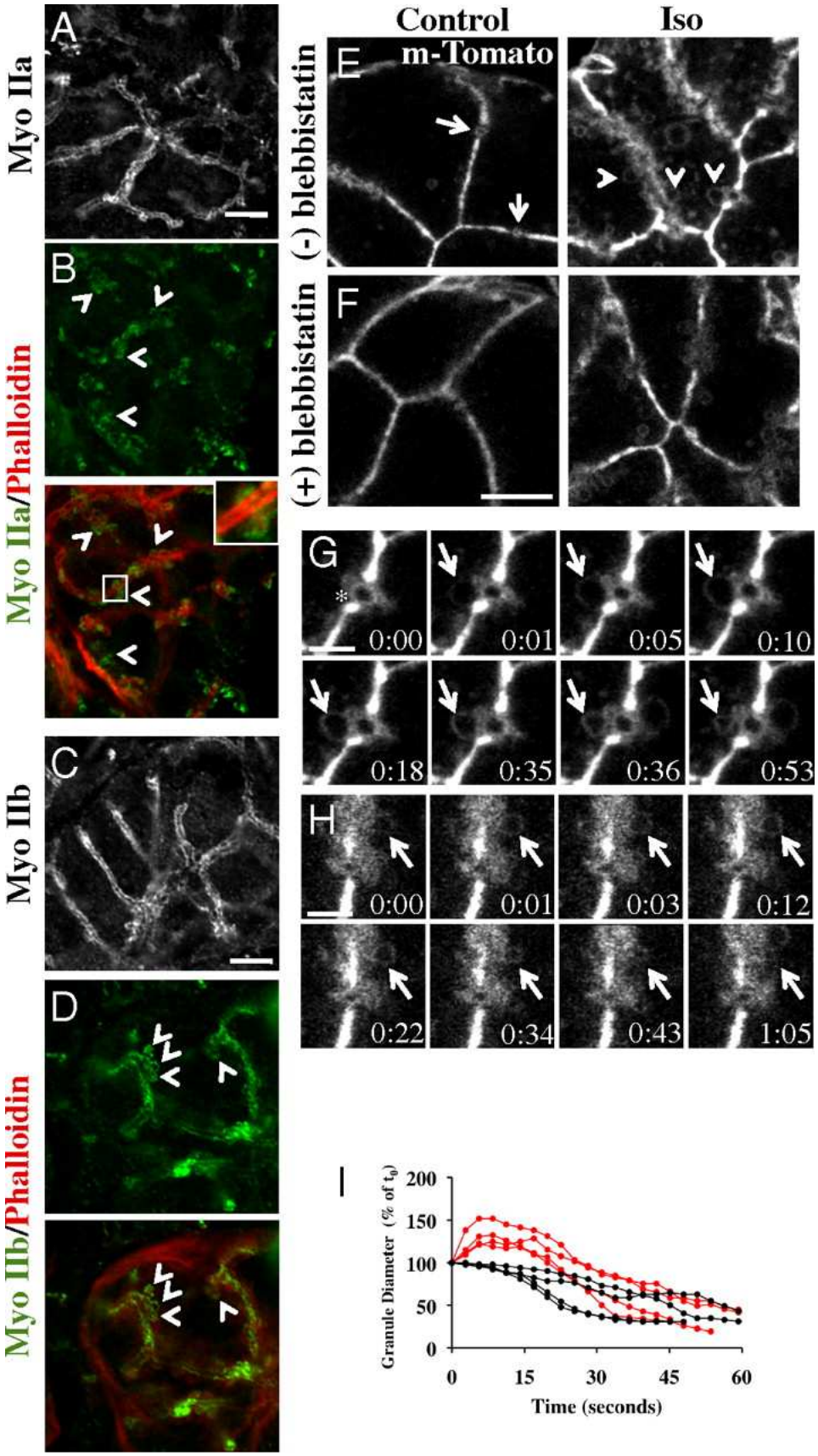
Myo IIa
Myo IIa/Phalloidin
Myo IIb
Myo IIb/Phalloidin
A
B
C
D
Control
Iso
E
m-Tomato
(-) blebbistatin
F
(+) blebbistatin
G
0:00
0:01
0:05
0:10
0:18
0:35
0:36
0:53
H
0:00
0:01
0:03
0:12
0:22
0:34
0:43
1:05
Granule Diameter (% of t0)
200
150
100
50
0
0
15
30
45
60
Time (seconds)

Figure 29. Role of myosin IIa and IIb in the collapse of the secretory granules. A–D. FVB mice were left untreated (A and C) or injected with 0.1 mg/kg Iso (Band D). SGs were excised and labeled for endogenous nonmuscle myosin IIa (A and B) and IIb (C and D) and actin (Band C) as described in Materials and Methods. Upon stimulation with Iso, both myosin types are localized in SCGs at the APM (arrowheads). Inset in B. An SCG at the APM. (Scale bars, 10 μm.) E–H. The SGs of m-Tomato mice were exposed and incubated with 50 μM of either (−)Bleb (E and G) or (+)Bleb (F and H). After 20 min, the SGs were imaged (E and F, Leftpanels). In the presence of (−)Bleb, the acinar canaliculi expanded (arrows). The mice were then injected s.c. with 0.1 mg/kg Iso and imaged in time-lapse mode (E and F, Right panels, and G and H). E and F. Snapshots taken 10 min after the Iso injection. Large granules appeared at the APM (arrowheads) (Scale bar in F, 10 μm.). G and H. Time-lapse sequence of SCGs fusing with APM (Movies S15 and S16). Expanded canaliculus (asterisk) (Scale bars, 3 μm.) I. Quantitation of the diameter of the SCGs after fusion with the APM in the presence of (−)Bleb (red circles) or (+)Bleb (black circles). Data shown are from four granules in the same acinus. A total of 15–20 granules were analyzed in two independent experiments.

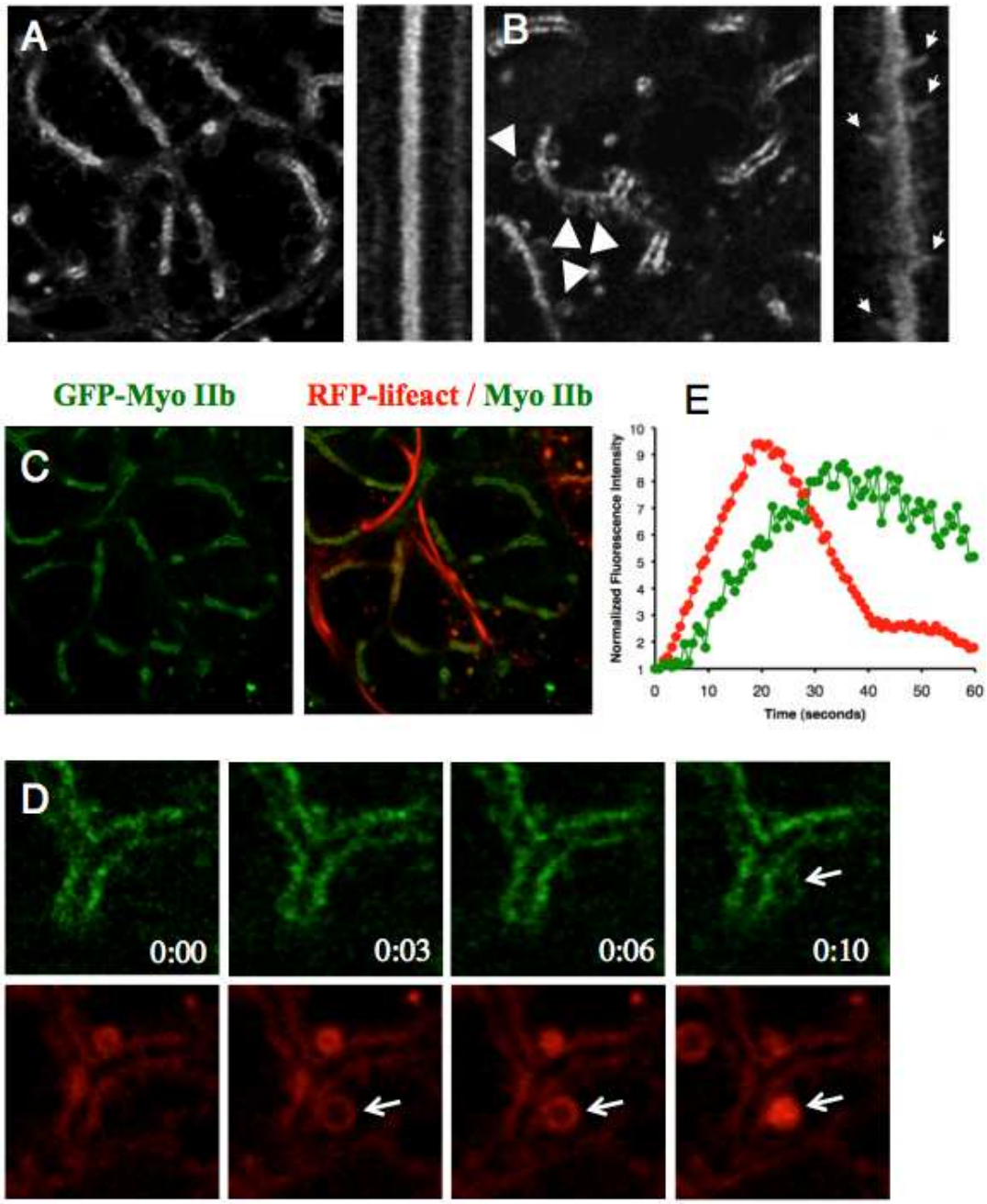

Figure 30. Myosin II and F-actin dynamics during regulated exocytosis. A and B. GFP-Myosin IIb expressing transgenic mice were anesthetized and set up for IVM. The acinar cells in the SG were imaged by confocal timelapse microscopy. GFP-Myosin IIb is enriched at the APM and lining the canaliculi. The SGs were imaged at resting conditions (A) and after s.c. injection of Iso at 0.1 mg/kg (B). After stimulation, GFP-Myosin IIb profiles resembling fusing granules appear at the canaliculi and undergo collapse (B). Such dynamics are captured in the kymograph of canalicular cross-section (B, arrows), while the control kymograph remains relatively smooth indicating no collapse events. C-E. Double transgenic mouse expressing GFP-Myosin IIb and RFP-Lifeact was anesthetized and imaged by IVM. Broad view of the acinar structure is shown in panel C, where both markers are enriched at

the apical canaliculi. D. Close-up snapshots of a canaliculus from a timelapse sequence taken shortly after Iso stimulation. F-actin marker and Myosin IIb recruitment on a granule can be seen. Interestingly, there appears to be a several second delay Myosin IIb recruitment. 10 s. time sequence is shown. E. A plot of relative fluorescence intensity over time is shown for a representative granule fusion/collapse event. The fluorescence was quantified by gating a region of interest around the fusing granule. The delay of 6-8 s. in the onset of GFP-Myosin IIb signal (green circles) can be observed. The fluorescence decline phase is also delayed by about 15s when compared to RFP-Lifeact (red circles).

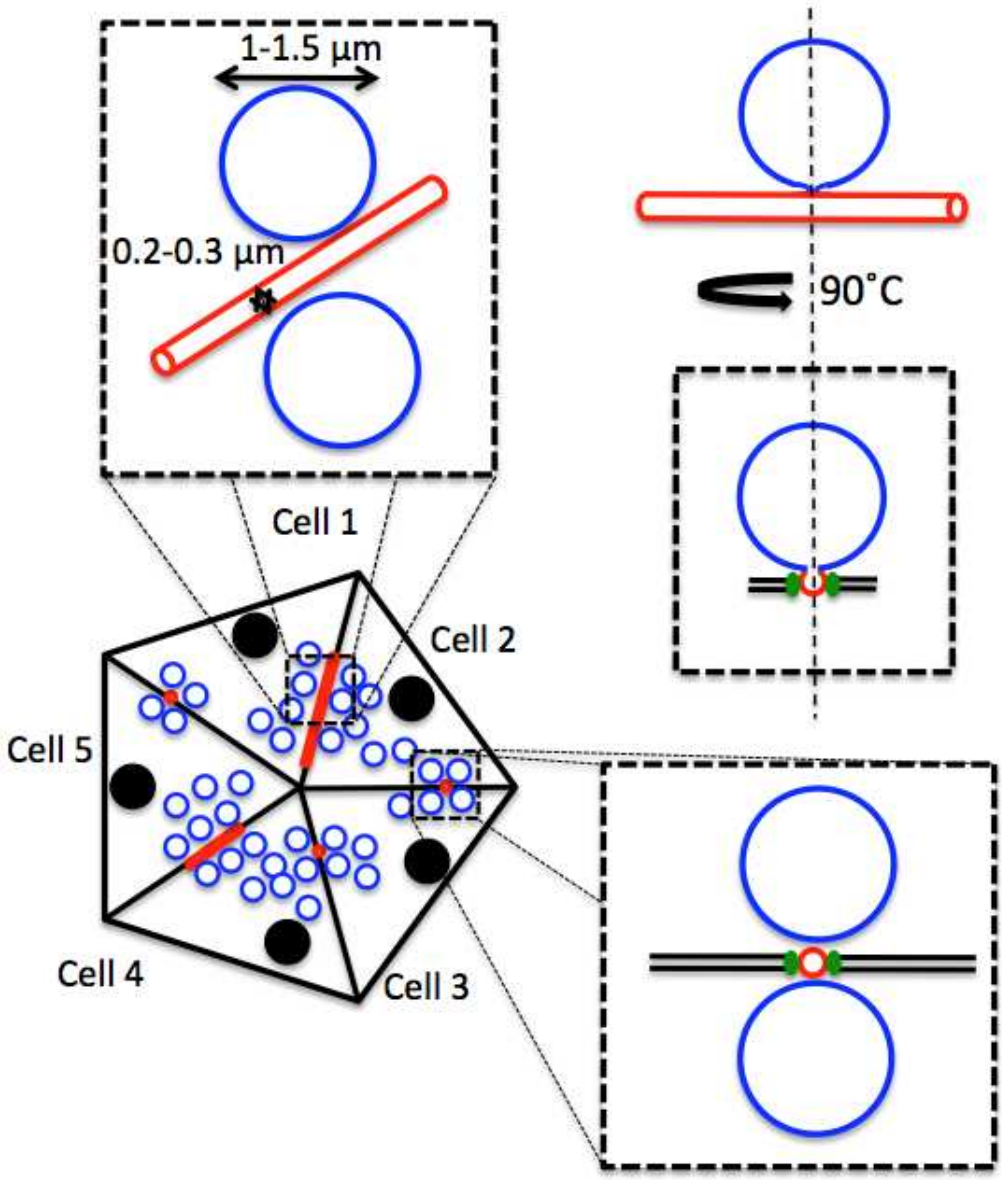

Figure 31. Organization of the granules and apical plasma membrane. Diagram of a SG acinus and organization of the APM. Acini are formed by pyramidal polarized epithelial cells that are in close contact and the APM (red) is shared by two cells and forms narrow canaliculi. The dashed boxes show two orthogonal enlargements of the apical area. The canaliculi have a diameter of 0.2-0.3 µm and are separated from the basolateral membrane by tight junctions (green). The SCGs (blue) have a much larger diameter (1-1.5 µm). When the fusion pore opens two compartments with different composition and membrane tension are interconnected (diagram on the right).

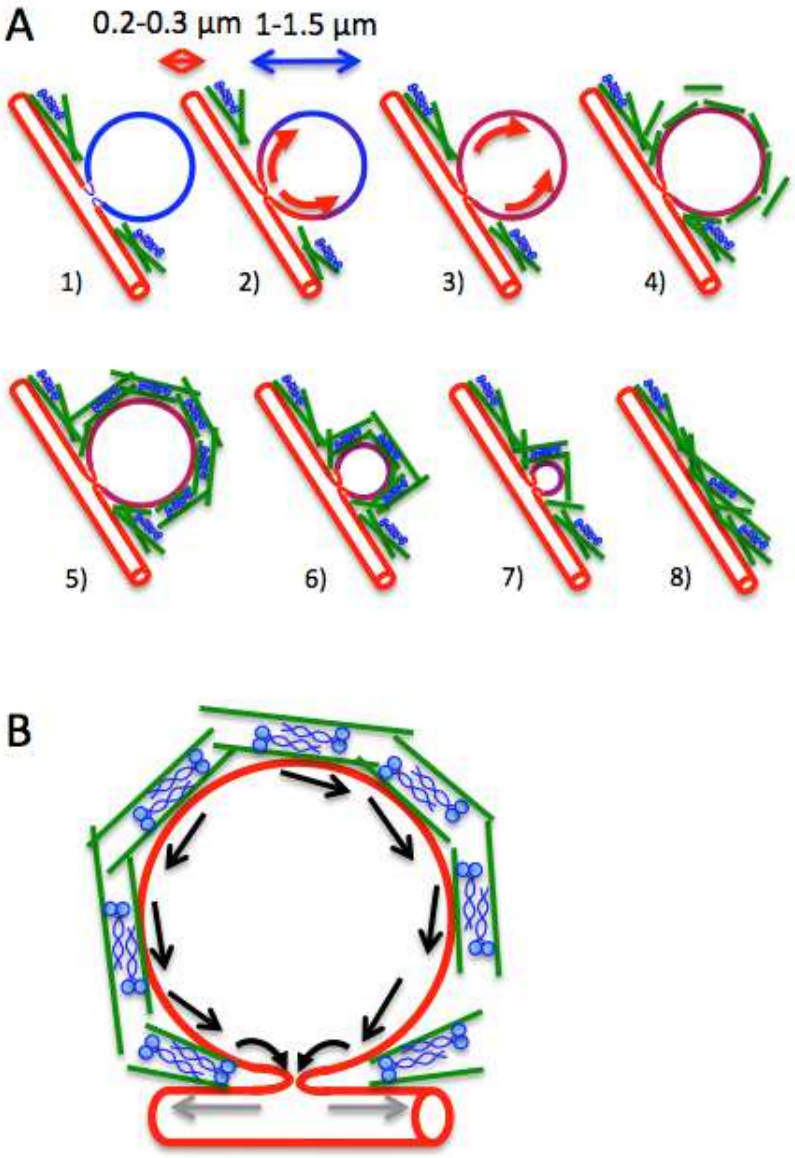

Figure 32. Role of the actomyosin complex in the gradual collapse of the secretory granules. A and B. Model depicting a sequence of events after granule fuses with the APM. SCGs (blue) fuse with the APM (red) and the fusion pore opens (1); the membranes flow from the APM into the SCGs (red arrows) (2-3). The difference in membrane tension and the presence of hydrostatic pressure in the ductal system are major factors working against in the gradual collapse of the SCGs. To counteract these forces, actomyosin complex assembles on to the granule membrane after the fusion and mixing of the membranes (4-5). The contractile activity of the actomyosin complex (actin, green rods; myosin II, blue) that assembles around the SCGs may push the membranes (black arrows in B) and/or dilate further the fusion pore (grey arrows in B) to facilitate the gradual collapse (6-8). B. Close-up model of step 5, after the actomyosin complex is assembled and exerting force onto the granule and, possibly, the fusion pore.

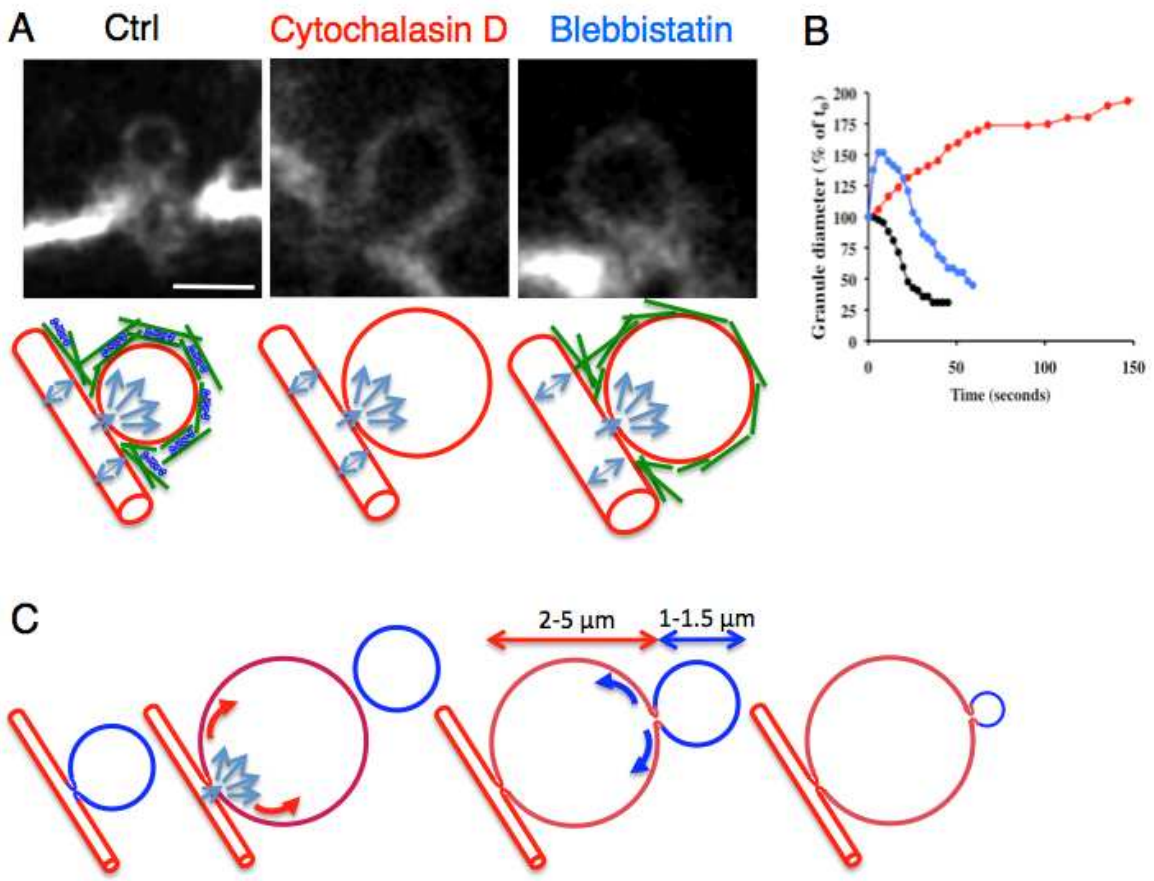

Figure 33. The actomyosin complex provides a scaffold to counteract the effect of the hydrostatic pressure on the secretory granules. A. Mice expressing the m-Tomato probe were pre-treated with cytochalasin D, blebbistatin or the vehicle (DMSO, ctrl) and injected with Iso to stimulate SCGs exocytosis. When the actin cytoskeleton was disrupted with cytochalasin D or the motor activity of myosin II was inhibited with blebbistatin the SCGs expanded in size due to the unfavorable membrane tension and the hydrostatic pressure generated by fluid secretion (light blue arrows). Scale bar, 2 µm. Actin (green) and myosin II (blue) are recruited to the SCGs to counteract the hydrostatic pressure and to facilitate the gradual collapse of the SCGs. B. SCGs were imaged after their fusion with the APM by using time-lapse intravital confocal microscopy. The diameter of the SCGs was measured over time in animals treated with cytochalasin D (red circles), blebbistatin (blue circles) or DMSO (black circles). C. In the absence of a functional actin cytoskeleton the SCGs expand forming large vacuoles (2-5 µm) due to the difference in membrane tension and the hydrostatic pressure generated by fluid secretion (light blue arrows). Membranes flow into the large vacuoles (red arrows), which acquire the properties of the APM. Due to the lower membrane tension of the large vacuoles, and reduced pressure in the sytem the remaining SCGs can now gradually collapse without the need of a functional actomyosin complex.

REFERENCES

[1] I. Mellman, "Endocytosis and molecular sorting," *Annu Rev Cell Dev Biol,* vol. 12, pp. 575-625, 1996.

[2] S. A. Mousavi, L. Malerod, T. Berg, and R. Kjeken, "Clathrin-dependent endocytosis," *Biochem J,* vol. 377, pp. 1-16, Jan 1 2004.

[3] J. G. Donaldson and D. B. Williams, "Intracellular assembly and trafficking of MHC class I molecules," *Traffic,* vol. 10, pp. 1745-52, Dec 2009.

[4] S. Mayor and R. E. Pagano, "Pathways of clathrin-independent endocytosis," *Nat Rev Mol Cell Biol,* vol. 8, pp. 603-12, Aug 2007.

[5] K. Sandvig, M. L. Torgersen, H. A. Raa, and B. van Deurs, "Clathrin-independent endocytosis: from nonexisting to an extreme degree of complexity," *Histochem Cell Biol,* vol. 129, pp. 267-76, Mar 2008.

[6] E. S. Chhabra and H. N. Higgs, "The many faces of actin: matching assembly factors with cellular structures," *Nat Cell Biol,* vol. 9, pp. 1110-21, Oct 2007.

[7] H. Girao, M. I. Geli, and F. Z. Idrissi, "Actin in the endocytic pathway: from yeast to mammals," *FEBS Lett,* vol. 582, pp. 2112-9, Jun 18 2008.

[8] C. J. Merrifield, M. E. Feldman, L. Wan, and W. Almers, "Imaging actin and dynamin recruitment during invagination of single clathrin-coated pits," *Nat Cell Biol,* vol. 4, pp. 691-8, Sep 2002.

[9] C. J. Merrifield, B. Qualmann, M. M. Kessels, and W. Almers, "Neural Wiskott Aldrich Syndrome Protein (N-WASP) and the Arp2/3 complex are recruited to sites of clathrin-mediated endocytosis in cultured fibroblasts," *Eur J Cell Biol,* vol. 83, pp. 13-8, Feb 2004.

[10] S. Benesch, S. Polo, F. P. Lai, K. I. Anderson, T. E. Stradal, J. Wehland, and K. Rottner, "N-WASP deficiency impairs EGF internalization and actin assembly at clathrin-coated pits," *J Cell Sci,* vol. 118, pp. 3103-15, Jul 15 2005.

[11] C. J. Merrifield, D. Perrais, and D. Zenisek, "Coupling between clathrin-coated-pit invagination, cortactin recruitment, and membrane scission observed in live cells," *Cell,* vol. 121, pp. 593-606, May 20 2005.

[12] N. Sauvonnet, A. Dujeancourt, and A. Dautry-Varsat, "Cortactin and dynamin are required for the clathrin-independent endocytosis of gammac cytokine receptor," *J Cell Biol,* vol. 168, pp. 155-63, Jan 3 2005.

[13] J. Zhu, K. Zhou, J. J. Hao, J. Liu, N. Smith, and X. Zhan, "Regulation of cortactin/dynamin interaction by actin polymerization during the fission of clathrin-coated pits," *J Cell Sci,* vol. 118, pp. 807-17, Feb 15 2005.

[14] K. R. Ayscough, "Endocytosis and the development of cell polarity in yeast require a dynamic F-actin cytoskeleton," *Curr Biol,* vol. 10, pp. 1587-90, Dec 14-28 2000.

[15] K. R. Ayscough, J. Stryker, N. Pokala, M. Sanders, P. Crews, and D. G. Drubin, "High rates of actin filament turnover in budding yeast and roles for actin in establishment and maintenance of cell polarity revealed using the actin inhibitor latrunculin-A," *J Cell Biol,* vol. 137, pp. 399-416, Apr 21 1997.

[16] C. Lamaze, L. M. Fujimoto, H. L. Yin, and S. L. Schmid, "The actin cytoskeleton is required for receptor-mediated endocytosis in mammalian cells," *J Biol Chem,* vol. 272, pp. 20332-5, Aug 15 1997.

[17] L. Pelkmans, D. Puntener, and A. Helenius, "Local actin polymerization and dynamin recruitment in SV40-induced internalization of caveolae," *Science,* vol. 296, pp. 535-9, Apr 19 2002.

[18] D. Yarar, C. M. Waterman-Storer, and S. L. Schmid, "A dynamic actin cytoskeleton functions at multiple stages of clathrin-mediated endocytosis," *Mol Biol Cell,* vol. 16, pp. 964-75, Feb 2005.

[19] T. A. Gottlieb, I. E. Ivanov, M. Adesnik, and D. D. Sabatini, "Actin microfilaments play a critical role in endocytosis at the apical but not the basolateral surface of polarized epithelial cells," *J Cell Biol,* vol. 120, pp. 695-710, Feb 1993.

[20] L. M. Fujimoto, R. Roth, J. E. Heuser, and S. L. Schmid, "Actin assembly plays a variable, but not obligatory role in receptor-mediated endocytosis in mammalian cells," *Traffic,* vol. 1, pp. 161-71, Feb 2000.

[21] R. D. Burgoyne and A. Morgan, "Secretory granule exocytosis," *Physiol Rev,* vol. 83, pp. 581-632, Apr 2003.

[22] J. R. Monck and J. M. Fernandez, "The fusion pore and mechanisms of biological membrane fusion," *Curr Opin Cell Biol,* vol. 8, pp. 524-33, Aug 1996.

[23] A. M. Sokac and W. M. Bement, "Kiss-and-coat and compartment mixing: coupling exocytosis to signal generation and local actin assembly," *Mol Biol Cell,* vol. 17, pp. 1495-502, Apr 2006.

[24] S. O. Rizzoli and R. Jahn, "Kiss-and-run, collapse and 'readily retrievable' vesicles," *Traffic,* vol. 8, pp. 1137-44, Sep 2007.

[25] H. Kasai, T. Kishimoto, T. Nemoto, H. Hatakeyama, T. T. Liu, and N. Takahashi, "Two-photon excitation imaging of exocytosis and endocytosis and determination of their spatial organization," *Adv Drug Deliv Rev,* vol. 58, pp. 850-77, Sep 15 2006.

[26] J. A. Pickett and J. M. Edwardson, "Compound exocytosis: mechanisms and functional significance," *Traffic,* vol. 7, pp. 109-16, Feb 2006.

[27] T. C. Sudhof, "The synaptic vesicle cycle," *Annu Rev Neurosci,* vol. 27, pp. 509-47, 2004.

[28] M. Malacombe, M. F. Bader, and S. Gasman, "Exocytosis in neuroendocrine cells: new tasks for actin," *Biochim Biophys Acta,* vol. 1763, pp. 1175-83, Nov 2006.

[29] K. M. Valentijn, J. E. Sadler, J. A. Valentijn, J. Voorberg, and J. Eikenboom, "Functional architecture of Weibel-Palade bodies," *Blood,* vol. 117, pp. 5033-43, May 12 2011.

[30] Y. A. Chizmadzhev, P. I. Kuzmin, D. A. Kumenko, J. Zimmerberg, and F. S. Cohen, "Dynamics of fusion pores connecting membranes of different tensions," *Biophys J,* vol. 78, pp. 2241-56, May 2000.

[31] A. Masedunskas, N. Porat-Shliom, and R. Weigert, "Linking differences in membrane tension with the requirement for a contractile actomyosin scaffold during exocytosis in salivary glands," *Commun. Integr. Biol,* In press.

[32] D. A. Ammar, P. N. Nguyen, and J. G. Forte, "Functionally distinct pools of actin in secretory cells," *Am J Physiol Cell Physiol,* vol. 281, pp. C407-17, Aug 2001.

[33] L. Orci, K. H. Gabbay, and W. J. Malaisse, "Pancreatic beta-cell web: its possible role in insulin secretion," *Science,* vol. 175, pp. 1128-30, Mar 10 1972.

[34] S. Muallem, K. Kwiatkowska, X. Xu, and H. L. Yin, "Actin filament disassembly is a sufficient final trigger for exocytosis in nonexcitable cells," *J Cell Biol,* vol. 128, pp. 589-98, Feb 1995.

[35] T. Nashida, S. Yoshie, A. Imai, and H. Shimomura, "Presence of cytoskeleton proteins in parotid glands and their roles during secretion," *Arch Oral Biol,* vol. 49, pp. 975-82, Dec 2004.

[36] T. Nemoto, T. Kojima, A. Oshima, H. Bito, and H. Kasai, "Stabilization of exocytosis by dynamic F-actin coating of zymogen granules in pancreatic acini," *J Biol Chem,* vol. 279, pp. 37544-50, Sep 3 2004.

[37] G. V. Jerdeva, K. Wu, F. A. Yarber, C. J. Rhodes, D. Kalman, J. E. Schechter, and S. F. Hamm-Alvarez, "Actin and non-muscle myosin II facilitate apical exocytosis of tear proteins in rabbit lacrimal acinar epithelial cells," *J Cell Sci,* vol. 118, pp. 4797-812, Oct 15 2005.

[38] P. Bhat and P. Thorn, "Myosin 2 maintains an open exocytic fusion pore in secretory epithelial cells," *Mol Biol Cell,* vol. 20, pp. 1795-803, Mar 2009.

[39] O. Larina, P. Bhat, J. A. Pickett, B. S. Launikonis, A. Shah, W. A. Kruger, J. M. Edwardson, and P. Thorn, "Dynamic regulation of the large exocytotic fusion pore in pancreatic acinar cells," *Mol Biol Cell,* vol. 18, pp. 3502-11, Sep 2007.

[40] R. Lyck, N. Ruderisch, A. G. Moll, O. Steiner, C. D. Cohen, B. Engelhardt, V. Makrides, and F. Verrey, "Culture-induced changes in blood-brain barrier transcriptome: implications for amino-acid transporters in vivo," *J Cereb Blood Flow Metab,* vol. 29, pp. 1491-502, Sep 2009.

[41] J. G. Burchfield, J. A. Lopez, K. Mele, P. Vallotton, and W. E. Hughes, "Exocytotic vesicle behaviour assessed by total internal reflection fluorescence microscopy," *Traffic,* vol. 11, pp. 429-39, Apr 2010.

[42] V. A. Lizunov, H. Matsumoto, J. Zimmerberg, S. W. Cushman, and V. A. Frolov, "Insulin stimulates the halting, tethering, and fusion of mobile GLUT4 vesicles in rat adipose cells," *J Cell Biol,* vol. 169, pp. 481-9, May 9 2005.

[43] Y. Xu, B. R. Rubin, C. M. Orme, A. Karpikov, C. Yu, J. S. Bogan, and D. K. Toomre, "Dual-mode of insulin action controls GLUT4 vesicle exocytosis," *J Cell Biol,* vol. 193, pp. 643-53, May 16 2011.

[44] U. K. Wiegand, A. Don-Wauchope, I. Matskevich, R. R. Duncan, J. Greaves, M. J. Shipston, D. K. Apps, and R. H. Chow, "Exocytosis studies in a chromaffin cell-free system: imaging of single-vesicle exocytosis in a chromaffin cell-free system using total internal reflection fluorescence microscopy," *Ann N Y Acad Sci,* vol. 971, pp. 257-61, Oct 2002.

[45] S. Zhang and T. H. Murphy, "Imaging the impact of cortical microcirculation on synaptic structure and sensory-evoked hemodynamic responses in vivo," *PLoS Biol,* vol. 5, p. e119, May 2007.

[46] J. A. Martina, X. S. Wu, M. Catalfamo, T. Sakamoto, C. Yi, and J. A. Hammer, 3rd, "Imaging of lytic granule exocytosis in CD8(+) cytotoxic T lymphocytes reveals a modified form of full fusion," *Cell Immunol,* vol. 271, pp. 267-79, 2011.

[47] M. Ohara-Imaizumi and S. Nagamatsu, "Insulin exocytotic mechanism by imaging technique," *J Biochem,* vol. 140, pp. 1-5, Jul 2006.

[48] T. D. Nightingale, I. J. White, E. L. Doyle, M. Turmaine, K. J. Harrison-Lavoie, K. F. Webb, L. P. Cramer, and D. F. Cutler, "Actomyosin II contractility expels von Willebrand factor from Weibel-Palade bodies during exocytosis," *J Cell Biol,* vol. 194, pp. 613-29, Aug 22 2011.

[49] H. Kasai, H. Hatakeyama, T. Kishimoto, T. T. Liu, T. Nemoto, and N. Takahashi, "A new quantitative (two-photon extracellular polar-tracer imaging-based quantification (TEPIQ)) analysis for diameters of exocytic vesicles and its application to mouse pancreatic islets," *J Physiol,* vol. 568, pp. 891-903, Nov 1 2005.

[50] N. Behrendorff, S. Dolai, W. Hong, H. Y. Gaisano, and P. Thorn, "Vesicle-associated membrane protein 8 (VAMP8) is a SNARE (soluble N-ethylmaleimide-sensitive factor attachment protein receptor) selectively required for sequential granule-to-granule fusion," *J Biol Chem,* vol. 286, pp. 29627-34, Aug 26 2011.

[51] T. Nemoto, R. Kimura, K. Ito, A. Tachikawa, Y. Miyashita, M. Iino, and H. Kasai, "Sequential-replenishment mechanism of exocytosis in pancreatic acini," *Nat Cell Biol,* vol. 3, pp. 253-8, Mar 2001.

[52] A. Segawa and A. Riva, "Dynamics of salivary secretion studied by confocal laser and scanning electron microscopy," *Eur J Morphol,* vol. 34, pp. 215-9, Aug 1996.

[53] A. Segawa, S. Terakawa, S. Yamashina, and C. R. Hopkins, "Exocytosis in living salivary glands: direct visualization by video-enhanced microscopy and confocal laser microscopy," *Eur J Cell Biol,* vol. 54, pp. 322-30, Apr 1991.

[54] Y. Chen, J. D. Warner, D. I. Yule, and D. R. Giovannucci, "Spatiotemporal analysis of exocytosis in mouse parotid acinar cells," *Am J Physiol Cell Physiol,* vol. 289, pp. C1209-19, Nov 2005.

[55] J. D. Warner, C. G. Peters, R. Saunders, J. H. Won, M. J. Betzenhauser, W. T. Gunning, 3rd, D. I. Yule, and D. R. Giovannucci, "Visualizing form and function in organotypic slices of the adult mouse parotid gland," *Am J Physiol Gastrointest Liver Physiol,* vol. 295, pp. G629-40, Sep 2008.

[56] G. B. Proctor and G. H. Carpenter, "Regulation of salivary gland function by autonomic nerves," *Auton Neurosci,* vol. 133, pp. 3-18, Apr 30 2007.

[57] J. S. Beck and B. N. Berg, "The Circulatory Pattern in the Islands of Langerhans," *Am J Pathol,* vol. 7, pp. 31-36 1, Jan 1931.

[58] F. Helmchen and W. Denk, "Deep tissue two-photon microscopy," *Nat Methods,* vol. 2, pp. 932-40, Dec 2005.

[59] J. Mertz, "Nonlinear microscopy: new techniques and applications," *Curr Opin Neurobiol,* vol. 14, pp. 610-6, Oct 2004.

[60] W. R. Zipfel, R. M. Williams, and W. W. Webb, "Nonlinear magic: multiphoton microscopy in the biosciences," *Nat Biotechnol,* vol. 21, pp. 1369-77, Nov 2003.

[61] P. J. Campagnola and L. M. Loew, "Second-harmonic imaging microscopy for visualizing biomolecular arrays in cells, tissues and organisms," *Nat Biotechnol,* vol. 21, pp. 1356-60, Nov 2003.

[62] M. Oheim, D. J. Michael, M. Geisbauer, D. Madsen, and R. H. Chow, "Principles of two-photon excitation fluorescence microscopy and other nonlinear imaging approaches," *Adv Drug Deliv Rev,* vol. 58, pp. 788-808, Sep 15 2006.

[63] M. Rubart, "Two-photon microscopy of cells and tissue," *Circ Res,* vol. 95, pp. 1154-66, Dec 10 2004.

[64] P. T. So, C. Y. Dong, B. R. Masters, and K. M. Berland, "Two-photon excitation fluorescence microscopy," *Annu Rev Biomed Eng,* vol. 2, pp. 399-429, 2000.

[65] G. E. Stutzmann and I. Parker, "Dynamic multiphoton imaging: a live view from cells to systems," *Physiology (Bethesda),* vol. 20, pp. 15-21, Feb 2005.

[66] K. Svoboda and R. Yasuda, "Principles of two-photon excitation microscopy and its applications to neuroscience," *Neuron,* vol. 50, pp. 823-39, Jun 15 2006.

[67] M. Göppert-Mayer, "Uber elementarakte mit zwei quantensprungen.," *Ann. Phys. (Leipzig),* vol. 5, pp. 273-94, 1931.

[68] W. Denk, J. H. Strickler, and W. W. Webb, "Two-photon laser scanning fluorescence microscopy," *Science,* vol. 248, pp. 73-6, Apr 6 1990.

[69] M. Oheim, E. Beaurepaire, E. Chaigneau, J. Mertz, and S. Charpak, "Two-photon microscopy in brain tissue: parameters influencing the imaging depth," *J Neurosci Methods,* vol. 111, pp. 29-37, Oct 15 2001.

[70] P. Theer, M. T. Hasan, and W. Denk, "Two-photon imaging to a depth of 1000 microm in living brains by use of a Ti:Al2O3 regenerative amplifier," *Opt Lett,* vol. 28, pp. 1022-4, Jun 15 2003.

[71] V. Andresen, S. Alexander, W. M. Heupel, M. Hirschberg, R. M. Hoffman, and P. Friedl, "Infrared multiphoton microscopy: subcellular-resolved deep tissue imaging," *Curr Opin Biotechnol,* vol. 20, pp. 54-62, Feb 2009.

[72] F. Bestvater, E. Spiess, G. Stobrawa, M. Hacker, T. Feurer, T. Porwol, U. Berchner-Pfannschmidt, C. Wotzlaw, and H. Acker, "Two-photon fluorescence absorption and emission spectra of dyes relevant for cell imaging," *J Microsc,* vol. 208, pp. 108-15, Nov 2002.

[73] E. Spiess, F. Bestvater, A. Heckel-Pompey, K. Toth, M. Hacker, G. Stobrawa, T. Feurer, C. Wotzlaw, U. Berchner-Pfannschmidt, T. Porwol, and H. Acker, "Two-photon excitation and emission spectra of the green fluorescent protein variants ECFP, EGFP and EYFP," *J Microsc,* vol. 217, pp. 200-4, Mar 2005.

[74] W. R. Zipfel, R. M. Williams, R. Christie, A. Y. Nikitin, B. T. Hyman, and W. W. Webb, "Live tissue intrinsic emission microscopy using multiphoton-excited native fluorescence and second harmonic generation," *Proc Natl Acad Sci U S A,* vol. 100, pp. 7075-80, Jun 10 2003.

[75] A. Zoumi, A. Yeh, and B. J. Tromberg, "Imaging cells and extracellular matrix in vivo by using second-harmonic generation and two-photon excited fluorescence," *Proc Natl Acad Sci U S A,* vol. 99, pp. 11014-9, Aug 20 2002.

[76] D. Debarre, W. Supatto, A. M. Pena, A. Fabre, T. Tordjmann, L. Combettes, M. C. Schanne-Klein, and E. Beaurepaire, "Imaging lipid bodies in cells and tissues using third-harmonic generation microscopy," *Nat Methods,* vol. 3, pp. 47-53, Jan 2006.

[77] A. J. Radosevich, M. B. Bouchard, S. A. Burgess, B. R. Chen, and E. M. Hillman,

"Hyperspectral in vivo two-photon microscopy of intrinsic contrast," *Opt Lett,* vol. 33, pp. 2164-6, Sep 15 2008.

[78] Y. Guan, R. T. Worrell, T. A. Pritts, and M. H. Montrose, "Intestinal ischemia-reperfusion injury: reversible and irreversible damage imaged in vivo," *Am J Physiol Gastrointest Liver Physiol,* vol. 297, pp. G187-96, Jul 2009.

[79] M. Paxian, S. A. Keller, B. Cross, T. T. Huynh, and M. G. Clemens, "High-resolution visualization of oxygen distribution in the liver in vivo," *Am J Physiol Gastrointest Liver Physiol,* vol. 286, pp. G37-44, Jan 2004.

[80] L. Wu, M. M. Tiwari, K. J. Messer, J. H. Holthoff, N. Gokden, R. W. Brock, and P. R. Mayeux, "Peritubular capillary dysfunction and renal tubular epithelial cell stress following lipopolysaccharide administration in mice," *Am J Physiol Renal Physiol,* vol. 292, pp. F261-8, Jan 2007.

[81] M. S. Roberts, M. J. Roberts, T. A. Robertson, W. Sanchez, C. Thorling, Y. Zou, X. Zhao, W. Becker, and A. V. Zvyagin, "In vitro and in vivo imaging of xenobiotic transport in human skin and in the rat liver," *J Biophotonics,* vol. 1, pp. 478-93, Dec 2008.

[82] K. A. Kasischke, H. D. Vishwasrao, P. J. Fisher, W. R. Zipfel, and W. W. Webb, "Neural activity triggers neuronal oxidative metabolism followed by astrocytic glycolysis," *Science,* vol. 305, pp. 99-103, Jul 2 2004.

[83] M. E. Llewellyn, R. P. Barretto, S. L. Delp, and M. J. Schnitzer, "Minimally invasive high-speed imaging of sarcomere contractile dynamics in mice and humans," *Nature,* vol. 454, pp. 784-8, Aug 7 2008.

[84] E. C. Rothstein, S. Carroll, C. A. Combs, P. D. Jobsis, and R. S. Balaban, "Skeletal muscle NAD(P)H two-photon fluorescence microscopy in vivo: topology and optical inner filters," *Biophys J,* vol. 88, pp. 2165-76, Mar 2005.

[85] G. Cox, E. Kable, A. Jones, I. Fraser, F. Manconi, and M. D. Gorrell, "3-dimensional imaging of collagen using second harmonic generation," *J Struct Biol,* vol. 141, pp. 53-62, Jan 2003.

[86] R. T. Megens, S. Reitsma, P. H. Schiffers, R. H. Hilgers, J. G. De Mey, D. W. Slaaf, M. G. oude Egbrink, and M. A. van Zandvoort, "Two-photon microscopy of vital murine elastic and muscular arteries. Combined structural and functional imaging with subcellular resolution," *J Vasc Res,* vol. 44, pp. 87-98, 2007.

[87] N. Morishige, W. M. Petroll, T. Nishida, M. C. Kenney, and J. V. Jester, "Noninvasive corneal stromal collagen imaging using two-photon-generated second-harmonic signals," *J Cataract Refract Surg,* vol. 32, pp. 1784-91, Nov 2006.

[88] A. M. Pena, A. Fabre, D. Debarre, J. Marchal-Somme, B. Crestani, J. L. Martin, E. Beaurepaire, and M. C. Schanne-Klein, "Three-dimensional investigation and scoring

of extracellular matrix remodeling during lung fibrosis using multiphoton microscopy," *Microsc Res Tech,* vol. 70, pp. 162-70, Feb 2007.

[89] K. Schenke-Layland, J. Xie, E. Angelis, B. Starcher, K. Wu, I. Riemann, W. R. MacLellan, and S. F. Hamm-Alvarez, "Increased degradation of extracellular matrix structures of lacrimal glands implicated in the pathogenesis of Sjogren's syndrome," *Matrix Biol,* vol. 27, pp. 53-66, Jan 2008.

[90] E. Brown, T. McKee, E. diTomaso, A. Pluen, B. Seed, Y. Boucher, and R. K. Jain, "Dynamic imaging of collagen and its modulation in tumors in vivo using second-harmonic generation," *Nat Med,* vol. 9, pp. 796-800, Jun 2003.

[91] J. Y. Perentes, T. D. McKee, C. D. Ley, H. Mathiew, M. Dawson, T. P. Padera, L. L. Munn, R. K. Jain, and Y. Boucher, "In vivo imaging of extracellular matrix remodeling by tumor-associated fibroblasts," *Nat Methods,* vol. 6, pp. 143-5, Feb 2009.

[92] J. B. Wyckoff, Y. Wang, E. Y. Lin, J. F. Li, S. Goswami, E. R. Stanley, J. E. Segall, J. W. Pollard, and J. Condeelis, "Direct visualization of macrophage-assisted tumor cell intravasation in mammary tumors," *Cancer Res,* vol. 67, pp. 2649-56, Mar 15 2007.

[93] K. Konig, A. Ehlers, I. Riemann, S. Schenkl, R. Buckle, and M. Kaatz, "Clinical two-photon microendoscopy," *Microsc Res Tech,* vol. 70, pp. 398-402, May 2007.

[94] C. L. Evans, E. O. Potma, M. Puoris'haag, D. Cote, C. P. Lin, and X. S. Xie, "Chemical imaging of tissue in vivo with video-rate coherent anti-Stokes Raman scattering microscopy," *Proc Natl Acad Sci U S A,* vol. 102, pp. 16807-12, Nov 15 2005.

[95] Y. Fu, T. B. Huff, H. W. Wang, H. Wang, and J. X. Cheng, "Ex vivo and in vivo imaging of myelin fibers in mouse brain by coherent anti-Stokes Raman scattering microscopy," *Opt Express,* vol. 16, pp. 19396-409, Nov 24 2008.

[96] J. J. Kang, I. Toma, A. Sipos, F. McCulloch, and J. Peti-Peterdi, "Quantitative imaging of basic functions in renal (patho)physiology," *Am J Physiol Renal Physiol,* vol. 291, pp. F495-502, Aug 2006.

[97] W. Yu, R. M. Sandoval, and B. A. Molitoris, "Quantitative intravital microscopy using a Generalized Polarity concept for kidney studies," *Am J Physiol Cell Physiol,* vol. 289, pp. C1197-208, Nov 2005.

[98] W. Yu, R. M. Sandoval, and B. A. Molitoris, "Rapid determination of renal filtration function using an optical ratiometric imaging approach," *Am J Physiol Renal Physiol,* vol. 292, pp. F1873-80, Jun 2007.

[99] L. R. Nyman, K. S. Wells, W. S. Head, M. McCaughey, E. Ford, M. Brissova, D. W. Piston, and A. C. Powers, "Real-time, multidimensional in vivo imaging used to

investigate blood flow in mouse pancreatic islets," *J Clin Invest,* vol. 118, pp. 3790-7, Nov 2008.

[100] M. J. Levene, D. A. Dombeck, K. A. Kasischke, R. P. Molloy, and W. W. Webb, "In vivo multiphoton microscopy of deep brain tissue," *J Neurophysiol,* vol. 91, pp. 1908-12, Apr 2004.

[101] E. Chaigneau, M. Oheim, E. Audinat, and S. Charpak, "Two-photon imaging of capillary blood flow in olfactory bulb glomeruli," *Proc Natl Acad Sci U S A,* vol. 100, pp. 13081-6, Oct 28 2003.

[102] E. Chaigneau, P. Tiret, J. Lecoq, M. Ducros, T. Knopfel, and S. Charpak, "The relationship between blood flow and neuronal activity in the rodent olfactory bulb," *J Neurosci,* vol. 27, pp. 6452-60, Jun 13 2007.

[103] B. Stefanovic, E. Hutchinson, V. Yakovleva, V. Schram, J. T. Russell, L. Belluscio, A. P. Koretsky, and A. C. Silva, "Functional reactivity of cerebral capillaries," *J Cereb Blood Flow Metab,* vol. 28, pp. 961-72, May 2008.

[104] D. Fukumura and R. K. Jain, "Imaging angiogenesis and the microenvironment," *APMIS,* vol. 116, pp. 695-715, Jul-Aug 2008.

[105] G. E. Koehl, A. Gaumann, and E. K. Geissler, "Intravital microscopy of tumor angiogenesis and regression in the dorsal skin fold chamber: mechanistic insights and preclinical testing of therapeutic strategies," *Clin Exp Metastasis,* vol. 26, pp. 329-44, 2009.

[106] J. Gavard, X. Hou, Y. Qu, A. Masedunskas, D. Martin, R. Weigert, X. Li, and J. S. Gutkind, "A role for a CXCR2/phosphatidylinositol 3-kinase gamma signaling axis in acute and chronic vascular permeability," *Mol Cell Biol,* vol. 29, pp. 2469-80, May 2009.

[107] A. A. Bhirde, V. Patel, J. Gavard, G. Zhang, A. A. Sousa, A. Masedunskas, R. D. Leapman, R. Weigert, J. S. Gutkind, and J. F. Rusling, "Targeted killing of cancer cells in vivo and in vitro with EGF-directed carbon nanotube-based drug delivery," *ACS Nano,* vol. 3, pp. 307-16, Feb 24 2009.

[108] B. R. Smith, Z. Cheng, A. De, A. L. Koh, R. Sinclair, and S. S. Gambhir, "Real-time intravital imaging of RGD-quantum dot binding to luminal endothelium in mouse tumor neovasculature," *Nano Lett,* vol. 8, pp. 2599-606, Sep 2008.

[109] C. Ricard, J. C. Vial, J. Douady, and B. van der Sanden, "In vivo imaging of elastic fibers using sulforhodamine B," *J Biomed Opt,* vol. 12, p. 064017, Nov-Dec 2007.

[110] P. Verant, C. Ricard, R. Serduc, J. C. Vial, and B. van der Sanden, "In vivo staining of neocortical astrocytes via the cerebral microcirculation using sulforhodamine B," *J Biomed Opt,* vol. 13, p. 064028, Nov-Dec 2008.

[111] M. Garcia-Alloza, L. A. Borrelli, A. Rozkalne, B. T. Hyman, and B. J. Bacskai, "Curcumin labels amyloid pathology in vivo, disrupts existing plaques, and partially restores distorted neurites in an Alzheimer mouse model," *J Neurochem,* vol. 102, pp. 1095-104, Aug 2007.

[112] T. L. Spires, M. Meyer-Luehmann, E. A. Stern, P. J. McLean, J. Skoch, P. T. Nguyen, B. J. Bacskai, and B. T. Hyman, "Dendritic spine abnormalities in amyloid precursor protein transgenic mice demonstrated by gene transfer and intravital multiphoton microscopy," *J Neurosci,* vol. 25, pp. 7278-87, Aug 3 2005.

[113] J. Livet, T. A. Weissman, H. Kang, R. W. Draft, J. Lu, R. A. Bennis, J. R. Sanes, and J. W. Lichtman, "Transgenic strategies for combinatorial expression of fluorescent proteins in the nervous system," *Nature,* vol. 450, pp. 56-62, Nov 1 2007.

[114] M. H. Grayson, R. S. Hotchkiss, I. E. Karl, M. J. Holtzman, and D. D. Chaplin, "Intravital microscopy comparing T lymphocyte trafficking to the spleen and the mesenteric lymph node," *Am J Physiol Heart Circ Physiol,* vol. 284, pp. H2213-26, Jun 2003.

[115] F. Hillen, E. L. Kaijzel, K. Castermans, M. G. oude Egbrink, C. W. Lowik, and A. W. Griffioen, "A transgenic Tie2-GFP athymic mouse model; a tool for vascular biology in xenograft tumors," *Biochem Biophys Res Commun,* vol. 368, pp. 364-7, Apr 4 2008.

[116] T. A. Sutton, H. E. Mang, S. B. Campos, R. M. Sandoval, M. C. Yoder, and B. A. Molitoris, "Injury of the renal microvascular endothelium alters barrier function after ischemia," *Am J Physiol Renal Physiol,* vol. 285, pp. F191-8, Aug 2003.

[117] W. Wang, J. B. Wyckoff, S. Goswami, Y. Wang, M. Sidani, J. E. Segall, and J. S. Condeelis, "Coordinated regulation of pathways for enhanced cell motility and chemotaxis is conserved in rat and mouse mammary tumors," *Cancer Res,* vol. 67, pp. 3505-11, Apr 15 2007.

[118] S. Pinner, P. Jordan, K. Sharrock, L. Bazley, L. Collinson, R. Marais, E. Bonvin, C. Goding, and E. Sahai, "Intravital imaging reveals transient changes in pigment production and Brn2 expression during metastatic melanoma dissemination," *Cancer Res,* vol. 69, pp. 7969-77, Oct 15 2009.

[119] S. Pinner and E. Sahai, "Imaging amoeboid cancer cell motility in vivo," *J Microsc,* vol. 231, pp. 441-5, Sep 2008.

[120] P. Bousso and E. Robey, "Dynamics of CD8+ T cell priming by dendritic cells in intact lymph nodes," *Nat Immunol,* vol. 4, pp. 579-85, Jun 2003.

[121] T. R. Mempel, S. E. Henrickson, and U. H. Von Andrian, "T-cell priming by dendritic cells in lymph nodes occurs in three distinct phases," *Nature,* vol. 427, pp. 154-9, Jan 8 2004.

[122] M. J. Miller, O. Safrina, I. Parker, and M. D. Cahalan, "Imaging the single cell dynamics of CD4+ T cell activation by dendritic cells in lymph nodes," *J Exp Med*, vol. 200, pp. 847-56, Oct 4 2004.

[123] M. J. Miller, S. H. Wei, I. Parker, and M. D. Cahalan, "Two-photon imaging of lymphocyte motility and antigen response in intact lymph node," *Science*, vol. 296, pp. 1869-73, Jun 7 2002.

[124] S. Stoll, J. Delon, T. M. Brotz, and R. N. Germain, "Dynamic imaging of T cell-dendritic cell interactions in lymph nodes," *Science*, vol. 296, pp. 1873-6, Jun 7 2002.

[125] H. D. Hickman, K. Takeda, C. N. Skon, F. R. Murray, S. E. Hensley, J. Loomis, G. N. Barber, J. R. Bennink, and J. W. Yewdell, "Direct priming of antiviral CD8+ T cells in the peripheral interfollicular region of lymph nodes," *Nat Immunol*, vol. 9, pp. 155-65, Feb 2008.

[126] J. G. Egen, A. G. Rothfuchs, C. G. Feng, N. Winter, A. Sher, and R. N. Germain, "Macrophage and T cell dynamics during the development and disintegration of mycobacterial granulomas," *Immunity*, vol. 28, pp. 271-84, Feb 2008.

[127] A. Boissonnas, L. Fetler, I. S. Zeelenberg, S. Hugues, and S. Amigorena, "In vivo imaging of cytotoxic T cell infiltration and elimination of a solid tumor," *J Exp Med*, vol. 204, pp. 345-56, Feb 19 2007.

[128] B. Breart, F. Lemaitre, S. Celli, and P. Bousso, "Two-photon imaging of intratumoral CD8+ T cell cytotoxic activity during adoptive T cell therapy in mice," *J Clin Invest*, vol. 118, pp. 1390-7, Apr 2008.

[129] B. Roediger, L. G. Ng, A. L. Smith, B. Fazekas de St Groth, and W. Weninger, "Visualizing dendritic cell migration within the skin," *Histochem Cell Biol*, vol. 130, pp. 1131-46, Dec 2008.

[130] H. Qi, J. G. Egen, A. Y. Huang, and R. N. Germain, "Extrafollicular activation of lymph node B cells by antigen-bearing dendritic cells," *Science*, vol. 312, pp. 1672-6, Jun 16 2006.

[131] L. E. Mansson, K. Melican, J. Boekel, R. M. Sandoval, I. Hautefort, G. A. Tanner, B. A. Molitoris, and A. Richter-Dahlfors, "Real-time studies of the progression of bacterial infections and immediate tissue responses in live animals," *Cell Microbiol*, vol. 9, pp. 413-24, Feb 2007.

[132] M. W. Laschke, S. Kerdudou, M. Herrmann, and M. D. Menger, "Intravital fluorescence microscopy: a novel tool for the study of the interaction of Staphylococcus aureus with the microvascular endothelium in vivo," *J Infect Dis*, vol. 191, pp. 435-43, Feb 1 2005.

[133] M. U. Norman, T. J. Moriarty, A. R. Dresser, B. Millen, P. Kubes, and G. Chaconas, "Molecular mechanisms involved in vascular interactions of the Lyme disease

pathogen in a living host," *PLoS Pathog*, vol. 4, p. e1000169, 2008.

[134] C. Lo Celso, H. E. Fleming, J. W. Wu, C. X. Zhao, S. Miake-Lye, J. Fujisaki, D. Cote, D. W. Rowe, C. P. Lin, and D. T. Scadden, "Live-animal tracking of individual haematopoietic stem/progenitor cells in their niche," *Nature*, vol. 457, pp. 92-6, Jan 1 2009.

[135] A. Mizrahi, J. C. Crowley, E. Shtoyerman, and L. C. Katz, "High-resolution in vivo imaging of hippocampal dendrites and spines," *J Neurosci*, vol. 24, pp. 3147-51, Mar 31 2004.

[136] F. Pan and W. B. Gan, "Two-photon imaging of dendritic spine development in the mouse cortex," *Dev Neurobiol*, vol. 68, pp. 771-8, May 2008.

[137] K. W. Dunn, R. M. Sandoval, K. J. Kelly, P. C. Dagher, G. A. Tanner, S. J. Atkinson, R. L. Bacallao, and B. A. Molitoris, "Functional studies of the kidney of living animals using multicolor two-photon microscopy," *Am J Physiol Cell Physiol*, vol. 283, pp. C905-16, Sep 2002.

[138] R. M. Sandoval, M. D. Kennedy, P. S. Low, and B. A. Molitoris, "Uptake and trafficking of fluorescent conjugates of folic acid in intact kidney determined using intravital two-photon microscopy," *Am J Physiol Cell Physiol*, vol. 287, pp. C517-26, Aug 2004.

[139] R. M. Sandoval and B. A. Molitoris, "Quantifying endocytosis in vivo using intravital two-photon microscopy," *Methods Mol Biol*, vol. 440, pp. 389-402, 2008.

[140] I. Toma, J. J. Kang, and J. Peti-Peterdi, "Imaging renin content and release in the living kidney," *Nephron Physiol*, vol. 103, pp. p71-4, 2006.

[141] Z. Zhong, V. K. Ramshesh, H. Rehman, R. T. Currin, V. Sridharan, T. P. Theruvath, I. Kim, G. L. Wright, and J. J. Lemasters, "Activation of the oxygen-sensing signal cascade prevents mitochondrial injury after mouse liver ischemia-reperfusion," *Am J Physiol Gastrointest Liver Physiol*, vol. 295, pp. G823-32, Oct 2008.

[142] A. M. Hall, R. J. Unwin, N. Parker, and M. R. Duchen, "Multiphoton imaging reveals differences in mitochondrial function between nephron segments," *J Am Soc Nephrol*, vol. 20, pp. 1293-302, Jun 2009.

[143] A. Masedunskas and R. Weigert, "nternalization of fluorescent dextrans in the submandibular salivary glands of live animals: A study combining intravital two-photon microscopy and second harmonic generation," *Progress in Biomedical Optics and Imaging - Proceedings of SPIE*, vol. 6860, 2008.

[144] J. Bao, X. Ma, C. Liu, and R. S. Adelstein, "Replacement of nonmuscle myosin II-B with II-A rescues brain but not cardiac defects in mice," *J Biol Chem*, vol. 282, pp. 22102-11, Jul 27 2007.

[145] J. Riedl, K. C. Flynn, A. Raducanu, F. Gartner, G. Beck, M. Bosl, F. Bradke, S. Massberg, A. Aszodi, M. Sixt, and R. Wedlich-Soldner, "Lifeact mice for studying F-actin dynamics," *Nat Methods,* vol. 7, pp. 168-9, Mar 2010.

[146] B. Peter, M. A. Van Waarde, A. Vissink, E. J. s-Gravenmade, and A. W. Konings, "Degranulation of rat salivary glands following treatment with receptor-selective agonists," *Clin Exp Pharmacol Physiol,* vol. 22, pp. 330-6, May 1995.

[147] M. Sramkova, A. Masedunskas, L. Parente, A. Molinolo, and R. Weigert, "Expression of plasmid DNA in the salivary gland epithelium: novel approaches to study dynamic cellular processes in live animals," *Am J Physiol Cell Physiol,* vol. 297, pp. C1347-57, Dec 2009.

[148] A. Masedunskas and R. Weigert, "Intravital two-photon microscopy for studying the uptake and trafficking of fluorescently conjugated molecules in live rodents," *Traffic,* vol. 9, pp. 1801-10, Sep 2008.

[149] R. Weigert, M. Sramkova, L. Parente, P. Amornphimoltham, and A. Masedunskas, "Intravital microscopy: a novel tool to study cell biology in living animals," *Histochem Cell Biol,* vol. 133, pp. 481-91, May 2010.

[150] S. L. Ashworth and G. A. Tanner, "Fluorescent labeling of renal cells in vivo," *Nephron Physiol,* vol. 103, pp. p91-6, 2006.

[151] G. A. Tanner, R. M. Sandoval, B. A. Molitoris, J. R. Bamburg, and S. L. Ashworth, "Micropuncture gene delivery and intravital two-photon visualization of protein expression in rat kidney," *Am J Physiol Renal Physiol,* vol. 289, pp. F638-43, Sep 2005.

[152] P. Amornphimoltham, A. Masedunskas, and R. Weigert, "Intravital microscopy as a tool to study drug delivery in preclinical studies," *Adv Drug Deliv Rev,* vol. 63, pp. 119-28, Jan-Feb 2011.

[153] J. Rohrer, A. Schweizer, D. Russell, and S. Kornfeld, "The targeting of Lamp1 to lysosomes is dependent on the spacing of its cytoplasmic tail tyrosine sorting motif relative to the membrane," *J Cell Biol,* vol. 132, pp. 565-76, Feb 1996.

[154] N. A. Bright, M. J. Gratian, and J. P. Luzio, "Endocytic delivery to lysosomes mediated by concurrent fusion and kissing events in living cells," *Curr Biol,* vol. 15, pp. 360-5, Feb 22 2005.

[155] A. Amsterdam, I. Ohad, and M. Schramm, "Dynamic changes in the ultrastructure of the acinar cell of the rat parotid gland during the secretory cycle," *J Cell Biol,* vol. 41, pp. 753-73, Jun 1969.

[156] S. U. Gorr, S. G. Venkatesh, and D. S. Darling, "Parotid secretory granules: crossroads of secretory pathways and protein storage," *J Dent Res,* vol. 84, pp. 500-9, Jun 2005.

[157] A. K. Hadjantonakis, M. Gertsenstein, M. Ikawa, M. Okabe, and A. Nagy, "Generating green fluorescent mice by germline transmission of green fluorescent ES cells," *Mech Dev,* vol. 76, pp. 79-90, Aug 1998.

[158] A. Diaspro and C. J. R. Shepard, *Two-Photon Microscopy: Basic Principles and Architectures* 2002.

[159] J. H. Sheetz, A. H. Morgan, and C. A. Schneyer, "Morphological and biochemical changes in the rat parotid gland after compensatory and isoproterenol-induced enlargement," *Arch Oral Biol,* vol. 28, pp. 441-5, 1983.

[160] R. J. Turner and H. Sugiya, "Understanding salivary fluid and protein secretion," *Oral Dis,* vol. 8, pp. 3-11, Jan 2002.

[161] C. C. Wang, H. Shi, K. Guo, C. P. Ng, J. Li, B. Q. Gan, H. Chien Liew, J. Leinonen, H. Rajaniemi, Z. H. Zhou, Q. Zeng, and W. Hong, "VAMP8/endobrevin as a general vesicular SNARE for regulated exocytosis of the exocrine system," *Mol Biol Cell,* vol. 18, pp. 1056-63, Mar 2007.

[162] T. Kanno, "Compound exocytosis of secretory granules containing salivary chromogranin A in granular duct cells in rat submandibular gland: the last study in collaboration with the late Professor Noboru Yanaihara at Yanaihara Institute," *Regul Pept,* vol. 123, pp. 3-7, Dec 15 2004.

[163] P. Thorn, K. E. Fogarty, and I. Parker, "Zymogen granule exocytosis is characterized by long fusion pore openings and preservation of vesicle lipid identity," *Proc Natl Acad Sci U S A,* vol. 101, pp. 6774-9, Apr 27 2004.

[164] P. Thorn and I. Parker, "Two phases of zymogen granule lifetime in mouse pancreas: ghost granules linger after exocytosis of contents," *J Physiol,* vol. 563, pp. 433-42, Mar 1 2005.

[165] M. D. Muzumdar, B. Tasic, K. Miyamichi, L. Li, and L. Luo, "A global double-fluorescent Cre reporter mouse," *Genesis,* vol. 45, pp. 593-605, Sep 2007.

[166] M. Kovacs, J. Toth, C. Hetenyi, A. Malnasi-Csizmadia, and J. R. Sellers, "Mechanism of blebbistatin inhibition of myosin II," *J Biol Chem,* vol. 279, pp. 35557-63, Aug 20 2004.

[167] J. Riedl, A. H. Crevenna, K. Kessenbrock, J. H. Yu, D. Neukirchen, M. Bista, F. Bradke, D. Jenne, T. A. Holak, Z. Werb, M. Sixt, and R. Wedlich-Soldner, "Lifeact: a versatile marker to visualize F-actin," *Nat Methods,* vol. 5, pp. 605-7, Jul 2008.

[168] O. Rocks, A. Peyker, and P. I. Bastiaens, "Spatio-temporal segregation of Ras signals: one ship, three anchors, many harbors," *Curr Opin Cell Biol,* vol. 18, pp. 351-7, Aug 2006.

[169] V. Idone, C. Tam, and N. W. Andrews, "Two-way traffic on the road to plasma

membrane repair," *Trends Cell Biol*, vol. 18, pp. 552-9, Nov 2008.

[170] G. Eitzen, "Actin remodeling to facilitate membrane fusion," *Biochim Biophys Acta*, vol. 1641, pp. 175-81, Aug 18 2003.

[171] M. A. Conti and R. S. Adelstein, "Nonmuscle myosin II moves in new directions," *J Cell Sci*, vol. 121, pp. 11-8, Jan 1 2008.

[172] T. Togo and R. A. Steinhardt, "Nonmuscle myosin IIA and IIB have distinct functions in the exocytosis-dependent process of cell membrane repair," *Mol Biol Cell*, vol. 15, pp. 688-95, Feb 2004.

[173] J. R. Beach and T. T. Egelhoff, "Myosin II recruitment during cytokinesis independent of centralspindlin-mediated phosphorylation," *J Biol Chem*, vol. 284, pp. 27377-83, Oct 2 2009.

[174] J. A. Pickett, P. Thorn, and J. M. Edwardson, "The plasma membrane Q-SNARE syntaxin 2 enters the zymogen granule membrane during exocytosis in the pancreatic acinar cell," *J Biol Chem*, vol. 280, pp. 1506-11, Jan 14 2005.

[175] A. Masedunskas, M. Sramkova, L. Parente, K. U. Sales, P. Amornphimoltham, T. H. Bugge, and R. Weigert, "Role for the actomyosin complex in regulated exocytosis revealed by intravital microscopy," *Proc Natl Acad Sci U S A*, vol. 108, pp. 13552-7, Aug 16 2011.

[176] Y. A. Chizmadzhev, D. A. Kumenko, P. I. Kuzmin, L. V. Chernomordik, J. Zimmerberg, and F. S. Cohen, "Lipid flow through fusion pores connecting membranes of different tensions," *Biophys J*, vol. 76, pp. 2951-65, Jun 1999.

[177] A. Masedunskas, M. Sramkova, and R. Weigert, "Homeostasis of the apical plasma membrane during regulated exocytosis in the salivary glands of live rodents," *Bioarchitecture*, In press.